



UNIVERSIDADE ESTADUAL DE CAMPINAS

FACULDADE DE ENGENHARIA MECÂNICA

Alexandre Monteiro Ribeiro

Identification and Control of an Electric Vehicle with Electronic Differential

Identificação e Controle de um Veículo Elétrico com Diferencial Eletrônico

CAMPINAS

2021

Alexandre Monteiro Ribeiro

Identification and Control of an Electric Vehicle with Electronic Differential

Identificação e Controle de um Veículo Elétrico com Diferencial Eletrônico

Thesis presented to the School of Mechanical Engineering of the University of Campinas in partial fulfillment of the requirements for the degree of Doctor in Mechanical Engineering, in the area of Mechatronics.

Tese apresentada à Faculdade de Engenharia Mecânica da Universidade Estadual de Campinas como parte dos requisitos exigidos para obtenção do título de Doutor em Engenharia Mecânica, na Área de Mecatrônica.

Orientador: Prof. Dr. André Ricardo Fioravanti

Coorientadora: Prof.^a Dra. Alexandra Bento Moutinho

Coorientador: Prof. Dr. Ely Carneiro de Paiva

ESTE EXEMPLAR CORRESPONDE À VERSÃO FINAL DA TESE DEFENDIDA PELO ALUNO ALEXANDRE MONTEIRO RIBEIRO, E ORIENTADA PELO PROF. DR. ANDRÉ RICARDO FIORAVANTI.

CAMPINAS

2021

Ficha catalográfica
Universidade Estadual de Campinas
Biblioteca da Área de Engenharia e Arquitetura
Rose Meire da Silva - CRB 8/5974

R354i Ribeiro, Alexandre Monteiro, 1990-
Identification and control of an electric vehicle with electronic differential /
Alexandre Monteiro Ribeiro. – Campinas, SP : [s.n.], 2021.

Orientador: André Ricardo Fioravanti.
Coorientadores: Ely Carneiro de Paiva e Alexandra Bento Moutinho.
Tese (doutorado) – Universidade Estadual de Campinas, Faculdade de
Engenharia Mecânica.

1. Programação semidefinida. 2. Veículos - Dinâmica. 3. Sistemas não-
lineares. 4. Veículos elétricos. I. Fioravanti, André Ricardo, 1982-. II. Paiva, Ely
Carneiro, 1965-. III. Moutinho, Alexandra Bento. IV. Universidade Estadual de
Campinas. Faculdade de Engenharia Mecânica. V. Título.

Informações para Biblioteca Digital

Título em outro idioma: Identificação e controle de um veículo elétrico com diferencial eletrônico

Palavras-chave em inglês:

Semidefinite programming

Vehicles - Dynamics

Nonlinear systems

Electric vehicles

Área de concentração: Mecatrônica

Titulação: Doutor em Engenharia Mecânica

Banca examinadora:

André Ricardo Fioravanti [Orientador]

Marcelo Becker

Ubirajara Franco Moreno

Ricardo Coração de Leão Fontoura de Oliveira

Matheus Souza

Data de defesa: 18-11-2021

Programa de Pós-Graduação: Engenharia Mecânica

Identificação e informações acadêmicas do(a) aluno(a)

- ORCID do autor: 0000-0002-7327-4112

- Currículo Lattes do autor: <http://lattes.cnpq.br/8362487201937848>

UNIVERSIDADE ESTADUAL DE CAMPINAS
FACULDADE DE ENGENHARIA MECÂNICA

TESE DE DOUTORADO

Identification and Control of an Electric Vehicle with Electronic Differential

Identificação e Controle de um Veículo Elétrico com Diferencial Eletrônico

Autor: Alexandre Monteiro Ribeiro

Orientador: Prof. Dr. André Ricardo Fioravanti

Coorientadora: Prof.^a Dra. Alexandra Bento Moutinho

Coorientador: Prof. Dr. Ely Carneiro de Paiva

A banca examinadora composta pelos membros abaixo aprovou esta tese:

Prof. Dr. André Ricardo Fioravanti, Presidente
Universidade Estadual de Campinas - UNICAMP

Prof. Dr. Marcelo Becker
Universidade de São Paulo - USP

Prof. Dr. Ubirajara Franco Moreno
Universidade Federal de Santa Catarina - UFSC

Prof. Dr. Ricardo Coração de Leão Fontoura de Oliveira
Universidade Estadual de Campinas - UNICAMP

Prof. Dr. Matheus Souza
Universidade Estadual de Campinas - UNICAMP

A Ata de Defesa com as respectivas assinaturas dos membros encontra-se no SIGA/Sistema de Fluxo de Dissertação/Tese e na Secretaria do Programa da Unidade.

Campinas, 18 de Novembro de 2021

Dedictory

This thesis is dedicated to my parents who supported me unconditionally during this journey.

Acknowledgements

First and foremost I would like to express my gratitude to my advisor, Dr. André R. Fioravanti, for his guidance, support, and thoughtful mentorship throughout my doctoral study. His patience, constant encouragement, and insightful discussions made it possible for me to conclude this Ph.D. degree.

I would like to extend my gratitude to my co-advisor Dr. Ely C. de Paiva, for all technical support, assistance, motivation, and enthusiasm during this research. I also wish to acknowledge Dr. Alexandra Moutinho for the mentorship and support provided during my stay in the IST.

I am grateful to all of the members of my defense committee, Dr. Marcelo Becker, Dr. Ubirajara Moreno, Dr. Ricardo de Oliveira, and Dr. Matheus Souza. Their willingness to read the thesis and thorough and helpful feedback were invaluable in helping to improve this dissertation. A further note of thanks is dedicated to the group members Dr. Niederauer Mastelari, Dr. Rafael Cordeiro, and Dr. Jozé Azinheira for their collaboration and assistance during this journey.

I have had the pleasure of working in the ACCES and LEVE laboratories with some great people: Apolo Marton, Vinicius Falcheto, Fernando Ortolano, Lucas Afonso, and Randerson Lemos. Undoubtedly, they made the lab a fun and enjoyable place.

In life, one hopes for a solid companionship. During the Ph.D. course, I have had the pleasure of meeting Ana Claudia Becari. Thank you for all your love and support.

Most importantly, I want to thank my family, my father Marcelo, my mother Sandra, and my sister Thaissa. Words can't express the influence they had on me. My family is my foundation, providing me with the stability that has allowed my academic growth. Their perseverance and patience with me far exceed what any parent should have to put up with. It is to them that I devote this dissertation.

Finally, I would like to convey my gratitude to FAPESP - Fundação de Amparo à Pesquisa do Estado de São Paulo, through Ph.D. scholarship 2018/05712-2, for providing me the financial support necessary for the development of this thesis.

Abstract

In the context of road vehicles, loss of stability may have critical safety implications. From this fact, we raise the need of studying vehicle stability for secure and reliable maneuvers execution. Simply determining whether the car, in a particular maneuver, is stable does not offer a comprehensive portrait of how far the system is from the stability boundary. By finding the region of attraction around the equilibrium point of the vehicular system, on the other hand, we can determine the direction and dimension of disturbances that will cause the vehicle to cross into the unstable region.

Within this field, this dissertation focuses upon ground vehicle stability analysis through the region of attraction (RoA) estimation. This region is defined by the set of initial conditions for which the system trajectories converge to the equilibrium. With the aid of sum-of-squares (SOS) programming techniques, Lyapunov functions, whose level sets are inner-bounds of the RoA, are found. The optimization approach is explored algorithmically and areas of local stability analysis and control synthesis are covered. A discussion around the decision variables to obtain larger inner bounds on the RoA is provided.

For local stability analysis, we present the SOS program that estimates the region of attraction for polynomial systems. The tire forces are approximated using both polynomial and rational functions and the lateral dynamics of a nonlinear vehicle model is written as a set of polynomial ordinary differential equations. The RoA is then estimated for the vehicle under various constant speed cornering and straight-line forward motion.

For controller synthesis, we present the SOS program that searches for a state feedback polynomial control law with input saturation for the objective of not only estimating, but also expanding the RoA. One major difficulty in this design is that the SOS generalizations assume affine-input systems, in which the vehicle model does not belong. The issue is addressed using the first-order Taylor expansion. A detailed discussion of such approximation is regarded.

The controller developed in this dissertation is evaluated in a scaled vehicle platform. To show that this vehicle is a valid and reliable test-bed platform whose lateral dynamics are similar to those of a full-sized vehicle, a thorough dynamic characterization is performed. With a persistent agreement between the theoretical and measured responses, the SOS-based analyses are confidently performed.

The SOS optimization-based methods in this dissertation complement the existing nonlinear analysis and design methods in the context of ground vehicles.

Keywords: Semidefinite programming; Vehicles - Dynamics; Nonlinear systems; Electric vehicles.

Resumo

No contexto de veículos terrestres, a perda de estabilidade pode ter implicações críticas de segurança. Desse fato, levantamos a necessidade de estudar a estabilidade do veículo para a execução de manobras de forma confiável e assegurada. O simples fato de determinar, em uma manobra em particular, se o veículo é estável não oferece um retrato abrangente de quão longe o sistema está do limite de estabilidade. Por outro lado, se conseguirmos determinar a região de atração em torno do ponto de equilíbrio do sistema, podemos estabelecer a direção e a dimensão dos distúrbios que farão o veículo cruzar para a região instável.

Dentro desta linha de raciocínio, esta dissertação é focada na análise de estabilidade de veículos terrestres por meio da estimativa da região de atração (RoA). Essa região é definida pelo conjunto de condições iniciais para as quais as trajetórias do sistema convergem para o equilíbrio. Através das técnicas de programação de soma de quadrados (SOS), é possível buscar por funções de Lyapunov cujas curvas de níveis são aproximações internas, ou estimativas, da RoA. Esta abordagem, que resulta em um problema de otimização convexo, é explorada algoritmicamente, permitindo cobrir a análise de estabilidade do sistema e a síntese de controle. Uma discussão sobre as variáveis de decisão para obter estimativas mais representativas da RoA é fornecida.

Para a análise de estabilidade local, apresenta-se o programa baseado em decomposições por SOS que estima a região de atração para sistemas polinomiais. As forças do pneu são aproximadas usando duas funções, polinomiais e racionais, e a dinâmica lateral de um modelo de veículo não linear é escrita como um conjunto de equações diferenciais ordinárias polinomiais. A RoA é então estimada para o veículo considerando-se diferentes condições iniciais. Assume-se velocidade constante em movimentos de curva e em linha reta.

Para a síntese do controlador, apresenta-se o programa SOS que busca uma lei de controle polinomial de realimentação em espaço de estados com inclusão de restrições de saturação das entradas. O objetivo passa a ser o de não só estimar mas também expandir a RoA. Uma grande dificuldade neste projeto consiste nas generalizações SOS que assumem exclusivamente sistemas afins na entrada, aos quais o modelo do veículo não pertence. O problema é abordado usando a expansão de Taylor de primeira ordem. Uma discussão detalhada de tal aproximação é considerada.

O controlador desenvolvido nesta dissertação é avaliado em uma plataforma de veículo em escala. Para mostrar que este veículo é de fato uma plataforma de teste válida e confiável, cuja dinâmica do movimento lateral é semelhante à de um veículo de tamanho real, é realizada uma caracterização completa. Com um alinhamento persistente entre as

respostas teóricas e medidas, as análises baseadas em SOS são realizadas no protótipo. Resultados sistemáticos são obtidos.

Os métodos baseados em otimização por SOS presentes nesta tese complementam as ferramentas de análise não linear e métodos de projeto existentes para o contexto de veículos terrestres.

Palavras-chave: Programação semidefinida; Veículos - Dinâmica; Sistemas não-lineares; Veículos elétricos.

List of Figures

1.1	Overall act of driving layout.	21
1.2	Layout of the operational vehicle control theory.	23
2.1	Four-wheel planar vehicle model.	33
2.2	Modified bicycle model. In (a) the rear tire is expanded to show the independent longitudinal force inputs and (b) the bicycle model with an equivalent rear axle and a yaw moment input term.	34
2.3	Corresponding lateral tire characteristic curve for Pacejka and Brush models. The results are shown for three values of friction coefficient μ . In (a) vertical load F_z is 2 kN and in (b) 4 kN.	36
2.4	Two-dimensional vertical force distribution considering a steady-state condition.	39
2.5	Phase portrait of the approximated bicycle model (dashed lines) and the complete planar vehicle model (solid lines). The vehicle is set at constant longitudinal velocity u_0 of 10 m/s . Green stars and black dots are equilibrium points of the bicycle and planar models, respectively. In (a) steering angle is set to 0 degrees and in (b) steering angle is set to -5 degrees. . . .	40
4.1	Illustration of the containment regions. The pink area stands for the true RoA. The blue area indicates the inner estimate and the green area is the region defined by the shaping function $s(x)$, strictly contained in Ω_γ	51
4.2	Phase portrait is shown in the background with initial conditions denoted by black dots. The estimated regions Ω_γ and \mathcal{S}_β are shown by the ellipses. The regions are obtained by picking (a) $s_1(x)$ and (b) $s_2(x)$	54
4.3	In the background is shown the phase portrait of the open-loop response with initial conditions denoted by black dots. The estimated RoAs for Lyapunov Functions of degrees 2, 4, 6, and 8.	63
4.4	The estimated RoAs of the closed-loop system are demonstrated using Lyapunov functions of orders 2, 4, 6 and 8, computed evaluating (a) IL and (b) CL linearizations, respectively.	64
5.1	Tire forces approximation. The Pacejka data points are shown as black circles along with 5th, 7th, and 9th order polynomial fits.	66

5.2	In background we present phase plane for the vehicle model assemble with polynomial approximation for the straight running maneuver. RoA estimates are shown using (a) $s(x) = x^T x$ and (b) $s(x) = V_{lin}$	68
5.3	RoA estimates for a constant cornering maneuver using $s(x) = V_{lin}$	69
5.4	Influence of $s(x)$ on the RoA estimate. $V(x)$ is a 4th order polynomial function. In (a) $s(x) = x^T x$ and (b) $s(x) = V_{lin}$	69
5.5	RoA estimate for the case where function $s(x)$ is defined as the previous Lyapunov function.	70
5.6	Estimated RoA of the controlled system for a constant cornering maneuver. In the background, we show the phase plane of the open-loop system. RoA is estimated by considering control laws K of (a) first-, (b) second-, (c) third-, and (d) fourth-orders.	72
5.7	Estimated region of attraction for the system under the LQR control. In the background are shown the phase plane of the open-loop plant. Lyapunov functions are shown for different degrees.	75
5.8	Pacejka's nonlinear tire force and its polynomial approximations using the linear, rational, and polynomial models.	76
5.9	Phase portrait for the bicycle model using the magic formula tire (solid lines) and the approximated polynomial tire (dashed lines). Black dots and green stars are equilibrium points of the real and approximated model, respectively. On the left, the system is assembled with a 7th order polynomial tire force approximation, and on right with the rational polynomial approximation.	77
5.10	RoA estimates for a straight running scenario ($\delta = 0$) with constant longitudinal speed $u_0 = 10$ m/s. Lyapunov functions are shown for different degrees. In the background, we show the phase plane of the open-loop system, with blue and orange lines representing the stable and unstable trajectories, respectively.	80
5.11	Estimated RoA of the controlled system for a straight running maneuver. In the background, we show the phase plane of the open-loop system. The estimated RoA under a control law $K(x)$ overcomes unstable paths around the saddle points. Furthermore, the input saturation bounds recognized in Table 6.1 are used in the control design.	81
5.12	RoA estimates for the open-loop maneuver. The vehicle steering angle $\bar{\delta}$ is set to -5 degrees with constant longitudinal speed $u_0 = 10$ m/s. The regions are estimated varying the degree of V from 2 to 8.	82

5.13	RoA estimates for the closed-loop maneuver. Phase plane is shown in the background. The regions are estimated varying the degree of $V(x)$ for a left-turn maneuver while synthesizing a first-order control law $K(x)$. Steering angle is set to -5 degrees with constant longitudinal speed $u_0 = 10 \text{ m/s}$. . .	82
5.14	State feedback and feedforward tracking controller diagram.	83
5.15	State trajectories (starting from the origin, shown as green stars) of the open and closed-loop scenarios. Phase plane are shown in the background for $\delta = -5^\circ$ and $u_0 = 10 \text{ m/s}$. Equilibrium points are denoted by black dots. On the right, the closed-loop trajectories are shown with the input saturation bounds recognized in Table 6.1.	84
5.16	Vehicle lateral v and angular r velocities response of the open and closed-loop systems. The main stages are highlighted in three intervals and trajectory indicated by dots diverges.	85
5.17	Comparison between the feedforward and the applied inputs by the proposed controller.	86
5.18	Vehicle trajectory and orientation.	87
5.19	Vehicle response for the straight running scenario. The results are shown for the open-loop (left) and closed-loop (right) systems. Blue and orange dots are the initial conditions of the converging and diverging trajectories, respectively. The estimated RoA is the largest level set obtained in Section 5.3.1.	88
5.20	Results of the cornering maneuver for the open-loop (left) and closed-loop (right) system. Blue and orange dots are the initial conditions of the converging and diverging trajectories, respectively. The estimated RoA is the largest level set obtained in section 5.3.1.	89
6.1	(a) Four-wheeled 1:5-scale platform. (b) Ackermann steering geometry. (c) The independent rear-wheel drive.	94
6.2	Diagram of the bicycle model.	95
6.3	Steering angle following the swept sine. The first half-wave period is discarded due to initial measurement noises.	99
6.4	Comparison between lateral (a) and angular (b) velocities for the sinusoidal steering angle input.	100
6.5	Trajectory of the proposed maneuver (a) and commanded steering angle (b).	100
6.6	In (a) lateral velocity and (b) angular velocity.	100
6.7	Set of experiments. The steering angle pattern is time-dependent fixed to the corresponding values: -5, -10, -15, and -20 degrees. Longitudinal velocity is (a) 0.3 m/s, (b) 0.4 m/s, (c) 0.5 m/s, (d) 0.6 m/s, and (e) 0.7 m/s.	102

6.8	Equilibrium points considering longitudinal velocities u_0 of (a) 0.4 m/s, (b) 1.0 m/s, and (c) 2.5 m/s.	104
6.9	Effect of changing the standard deviation of (a) longitudinal velocity and (b) friction coefficient.	106
6.10	Estimated RoA. Steering angle is set to (a) $\delta = 0$, (b) $\delta = -5$, and (c) $\delta = -10$ degrees.	108
6.11	Estimated RoA of the closed-loop system. Steering angle is set to (a) $\delta = 0$, (b) $\delta = -5$, and (c) $\delta = -10$ degrees.	109
6.12	Performed trajectory. The results are obtained using (a) first- and (b) third-orders controllers. Green and red marks are the initial and ending positions.	110
6.13	Measured longitudinal velocity for the closed-loop maneuver using (a) first- and (b) third-orders controllers.	111
6.14	Desired and achieved equilibrium conditions. Left and right figures are obtained using the first and third order controllers, respectively.	111
6.15	Commanded steering angle using the (a) first- and (b) third-order controllers.	112
6.16	Level sets of the polynomial control law. Dashed and continuous lines stand for the first- and third-orders controllers, respectively.	112

List of Tables

4.1	RoA's estimated area under a state feedback controller for different degrees of V	64
5.1	Vehicle and tire model main physical parameters.	67
5.2	Rising area of the estimated RoA as increasing the order of polynomial $V(x)$	70
5.3	Area of the estimated RoA under a polynomial state feedback controller of arbitrary degree.	73
5.4	Polynomial control gains K_i of degrees varying from 1 to 4 obtained with the sixth-order Lyapunov Functions. K_1 and K_2 are the state feedback control gains of inputs δ and M_z , respectively.	74
5.5	Area of the estimated RoAs for the system under the LQR control.	75
5.6	Estimated RoA areas (m rad/s ²) for the open-loop and closed-loop scenarios of the straight running maneuver. NP: Numerical Problems.	80
5.7	Estimated RoA areas (m rad/s ²) for the open-loop and closed-loop scenarios of the constant cornering maneuver. NP: Numerical Problems.	82
5.8	Computational statistics of Algorithms 1 and 2 for the open- and closed-loop analysis, respectively. NP: Numerical Problems.	83
5.9	A Monte-Carlo analysis of initial conditions inside the predicted ROA.	89
5.10	A Monte-Carlo analysis of initial conditions located outside the predicted region of attraction.	90
5.11	Open-loop and closed-loop stable region of Figures 5.19 and 5.20.	90
6.1	List of the vehicle's physical parameters.	98
6.2	Simulated (sim.) and real equilibrium points as well as their absolute difference (error) for each 10 seconds segment (T1 to T4) of the scenarios presented in Figure 6.7.	101
6.3	List of physical parameters.	107
6.4	Theoretical stable equilibrium points calculated from the bicycle model.	108
6.5	Expected and reached values using the first- and third-order controllers.	113

List of Acronyms and Symbols

Acronyms

ABS	Anti-lock brake system
TV	Torque vectoring
ESP	Electronic stability program
RoA	Region of attraction
SOS	Sum-of-squares
LF	Lyapunov function
SDP	Semidefinite programming
IL	Input linearization
CL	Control linearization
ODE	Ordinary differential equations
LQR	Linear quadratic regulator
CG	Center of gravity
GPS	Global positioning system
IMU	Inertial measurement unit
LIDAR	Light detection and ranging
SLAM	Simultaneous localization and mapping
EP	Equilibrium points

Greek symbols

Σ_n	Set of sum-of-squares polynomials in n variables
Ω_γ	Positively invariant region that is an inner estimate of the RoA
γ	Level set of region Ω_γ
β	Level set of region \mathcal{S}_β
ϵ_k	Small positive constant
φ_k	Positive polynomial with sufficiently small coefficients
δ	Steering angle
μ	Friction coefficient
α	Tire's slip angle
λ_i	Weighting and regularization factors

Latin symbols

A	Linear dynamic system matrix
B	Linear input system matrix
V	Lyapunov function
V_{lin}	Quadratic Lyapunov function derived from the linearized model
I_z	Yaw moment of inertia
M_z	Yaw moment generated by the rear-wheel drive differential
C_α	Tire cornering stiffness
\mathcal{S}_β	Domain of the shaping function at level set β
s	Shaping function
u	Vehicle longitudinal velocity

v	Vehicle lateral velocity
r	Vehicle yaw rate
a	Distance from CG to the front axle
b	Distance from CG to the rear axle
c	Half distance of the axle track
m	Vehicle mass
g	Gravitational acceleration
h_g	Suspension length
a_y	Lateral acceleration

Subscripts

fr, fl, rr, rl	Front right, front left, rear right, and rear left quantities, respectively
r, f	rear and front quantities, respectively
y	y -axis of the local coordinate system
x	x -axis of the local coordinate system
eq	An equilibrium condition
max	Maximum allowable value
lb	Lower bound
ub	Upper bound

Functions and special math operators

$\overline{(\cdot)}$	Steady-state values
$\widehat{(\cdot)}$	Estimated quantities
$\deg(\cdot)$	Degree of a polynomial function

Contents

1	Introduction	21
1.1	Context	21
1.2	Vehicle Control	22
1.2.1	Stability analysis	23
1.2.2	Vehicle stabilization	24
1.2.3	Envelope control	25
1.3	Motivation	25
1.3.1	Sum-of-squares programming	26
1.3.2	Region of attraction analysis for nonlinear vehicle dynamics	28
1.4	Scope and Objectives of the Work	28
1.5	Thesis Outline	29
2	Vehicle Modeling	32
2.1	Introduction	32
2.2	Planar Model	32
2.3	Tire Fundamentals	35
2.3.1	Brush tire model	37
2.3.2	Pacejka tire model	37
2.4	Four-Wheel and Bicycle Model Analysis	38
2.4.1	Review and comparison	38
2.5	Linear model	40
2.6	Final Remarks	41
3	Mathematical Preliminaries	42
3.1	Background on Polynomials	42
3.1.1	Sum-of-squares polynomials	43
3.2	Positivstellensatz	43
4	Local Stability and Controller Synthesis	46
4.1	Introduction	46
4.2	Local Stability	47
4.3	Expanding Interior Algorithm	47
4.3.1	Numerical example	53

4.4	Expanding the RoA with State Feedback	54
4.4.1	Expanding interior state feedback design	55
4.4.2	Input saturation	57
4.5	Non-Affine in Control Nonlinear Systems	58
4.5.1	Input linearization (IL)	59
4.5.2	Control linearization (CL)	60
4.5.3	Illustrative example	60
4.6	Theoretical Example	62
4.6.1	Estimating the RoA	62
4.6.2	Expanding the RoA	63
4.7	Final Remarks	64
5	RoA Estimation and State Feedback	65
5.1	Introduction	65
5.2	Polynomial Approximation	65
5.2.1	Region of attraction estimation	66
5.2.2	Expanding the RoA with state feedback and input saturation . . .	70
5.2.3	SOS vs LQR control performance	73
5.3	Rational Polynomial Approximation	75
5.3.1	RoA estimation and state feedback design	79
5.3.2	Control performance evaluation	83
5.3.3	Effect of model dissimilarity	87
5.4	Final Remarks	91
6	Experimental Evaluation	92
6.1	Introduction	92
6.2	Motivations	93
6.3	Vehicle Modeling	95
6.4	Parameter Identification	96
6.4.1	Data collection	97
6.4.2	Experimental setup	98
6.4.3	Experimental identification	98
6.4.4	Validation	99
6.4.5	Systematic investigation	101
6.5	Stability Analysis	103
6.5.1	Sensitivity analysis of the stable equilibrium points	105
6.6	Experimental Validation	107
6.7	Final Remarks	113

7 Conclusion	115
7.1 Summary	115
7.2 Future Research Directions	116
7.2.1 Inclusion of longitudinal and vertical dynamics and weight transfer	116
7.2.2 Regulation in unstable equilibrium conditions	117
7.2.3 Performance requirements	117
7.2.4 Experimental validation	118

1 Introduction

The constant technological advances in automotive, sensor, electronics, and computer industries are empowering the development of more efficient and modern road vehicles. The existent versatile tools range from driverless cars to the widespread use of assistive technologies.

By efficient vehicles, we mean all improvements, advantages, and benefits that arise as an effect of vehicle automatization. A decrease in the effect of the human factor on the process of driving is expected to improve road safety and facilitate the achievement of more efficient transport services. Some of the everyday life advantages of using autonomous technologies are reduction of the number and severity of road traffic accidents; reduction of time-consuming driving tasks; use of renewable energy and reduction of local air pollution; comfort; performance; and autonomy.

The following sections will consider the primary levels of ground vehicle control to highlight and direct the central theory aspects of the present thesis.

1.1 Context

In conformity with SAE J3016 [SAE International, 2018], which is a recognized document that describes and regularize the process of vehicle driving automation, the overall act of driving can be divided into three types of driver effort, as depicted in Figure 1.1. They are the strategic, tactical, and operational levels.

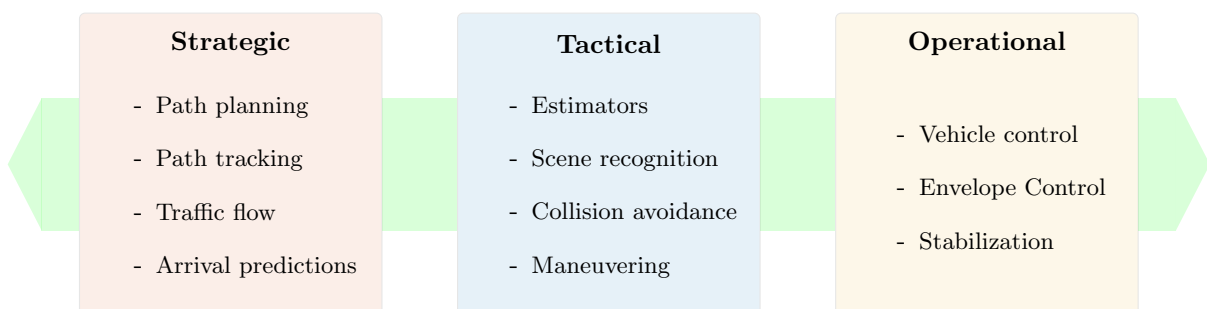


Figure 1.1. Overall act of driving layout.

The Strategic level encompasses motion planning tasks. Commonly, strategies within this layer are responsible to design the reference path. Despite the theoretical and tech-

nological advancements in this field, there are still many challenges identified as optimal route planning. Combining safety, real-time traffic conditions, traffic flow, number of intersections across the path, reduction of fuel consumption, and environmental pollution are some of the actual demanding tasks [Mac et al., 2016, Guo et al., 2019].

Moreover, with the deployment of fully electric vehicle technology, the mobility is expected to become more dependent and subordinate to critical infrastructures, incorporating range constraints, restrictions of autonomy, and the need for inclusion of waypoints, such as charging facilities, across the path [Gambutu et al., 2015].

The Tactical level comprises the act of navigation to achieve the objective. It mainly includes activities related to perception and recognition in order to make decisions such as executing a lane change, overtaking, breaking, and defining speed limits.

Nowadays, driving systems mainly rely on neural networks and machine learning techniques to detect, recognize, and extract the surrounding environment information [Lin et al., 2018, You et al., 2018, Chen et al., 2018]. These intelligent-based approaches revealed adequate and promising methods to make empirical decisions and judgments, especially when accuracy and correctness are required in subjective scenarios [Li et al., 2018].

Finally, the Operational level involves innate vehicle actions. They encompass steering, speeding, braking, performing yaw balance, or any other source of actuation existing in the vehicle.

Many control structures are common in existing commercial technologies known for their functional, practical, and efficient driving assistance. With different concepts and purposes, they appear in several solutions such as emergency braking, adaptive cruise control, collision mitigation brake system, electronic stability program, electronic stability control among others [Yue et al., 2018].

The research described in this thesis is particularly concerned and concentrated on the operational vehicle level. Essentially, we cover the vehicle control structure. Moreover, we specialize in a Lyapunov-based method for analyzing, estimating, and enhancing stability using a control structure.

1.2 Vehicle Control

It is worth mentioning that, although separated, linkages among the three discussed layers should be frequent. For instance, it is natural that a low-level controller demands non-measurable signals that must be obtained from an estimator or extracted from a scene recognition. Depending on the application's complexity, this crossing information is essential to feed the controller with the references, or even the strategy can merge the layers into a single structure. A strict categorization, therefore, may be fuzzy.

Focusing on the operational level, within the vehicular control field, we grouped the research topics into different categories according to their objectives. Figure 1.2 provides the state-of-the-art overview in vehicle control.

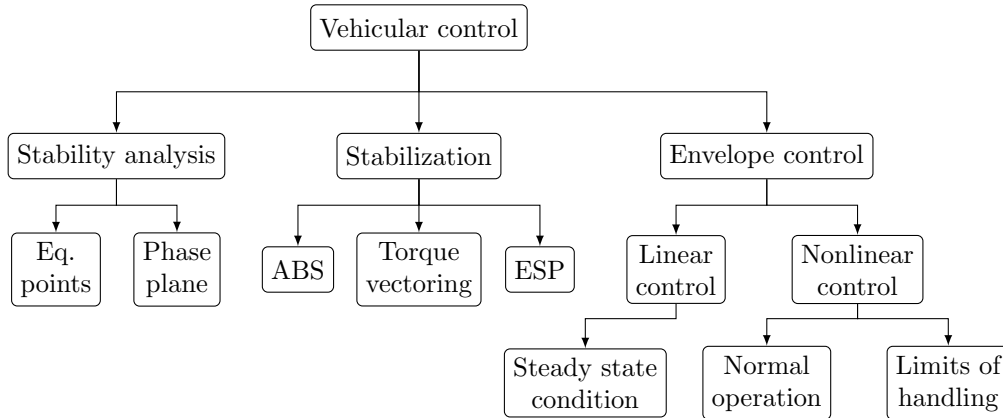


Figure 1.2. Layout of the operational vehicle control theory.

At the top level, the vehicle is separated into three main categories. The following sections discuss some of the present technologies and subjects of researches relevant to the design of vehicle controllers.

1.2.1 Stability analysis

The analysis of solutions of differential equations and the trajectories of dynamical systems is a standard topic of the control theory. From such analysis, one can describe and predict the behavior of initial conditions.

From a dynamical systems standpoint, the analysis begins investigating the equilibrium points. At this specific topic of interest, the concept of linearization naturally arises. In [True, 1999], it was shown that the linearized vehicle system is able to give valuable information and easy to perceive local properties of the nonlinear problem. In a similar fashion, [Sun et al., 2013] reported a method based on eigenvalue analysis of a linear vehicle model. However, the contributions of these analyses are strongly limited. The eigenvalues and the corresponding eigenvectors provide directions and capture the vehicle behaviors near the neighborhood of the equilibrium points. It should not be used to represent the system otherwise.

When it comes to phase portraits, on the other hand, they are a powerful visual medium that provides graphical insight into the system dynamics. For this reason, this topic is where the majority of vehicle stability analysis concentrates. As shown in [Hindiye and Christian Gerdes, 2014], given a set of control inputs and a two-state single-track model, the effect of changing parameters and the resulting range of possible trajectories are verified through a set of phase portrait plots. In [Hindiye, 2013], a bifurcation analysis is developed for a three-state bicycle model, including the longitudinal

dynamics and the effect of combined forces on tires. It was shown that the friction ellipse and saturation constraints are crucial to define the unstable equilibrium points. Four years later, [Cordeiro et al., 2017] extended the analysis to a four-wheel vehicle model, including the vertical forces distribution.

A closed-loop response analysis is proposed in [Beal and Boyd, 2019]. The coupled effects of longitudinal and lateral forces generated by the tires as a result of control actions are verified in three-dimensional phase portraits. The overall stability is discussed following the Lyapunov conditions statements.

Along similar lines, [Bobier-Tiu et al., 2018a] proposes a superimposition of phase portraits to design a control strategy. The phase planes are computed with the extremes of a steering angle control input and, as the main result, the largest range of feasible and stable closed-loop trajectories was identified.

1.2.2 Vehicle stabilization

The second category is the vehicle stabilization approaches. Within this division, one finds most of the existing commercial technologies in production vehicles. They are the well-known anti-lock brake system (ABS), torque vectoring (TV), and electronic stability program (ESP) which are known for assisting the drivers during maneuvers. These types of systems do not take any path information or dynamical analyses into account and focus only on vehicle stabilization.

The ABS stabilize the vehicle by adjusting the braking force in order to prevent excessive slide. The adjustment is made according to the available tire-road adhesion conditions [Aly et al., 2011]. The ESP stabilizes a vehicle by providing unequal braking torques. It creates a yaw motion that enables the vehicle to follow the desired driver's intention. A detailed explanation of how ESP operates and its proven importance by largely reducing accidents can be found in [Høye, 2011, Lutz et al., 2017]

Unlike ESP and ABS, that focus on controlling longitudinal inputs through the brake, the TV can provide yaw balance without degenerating the longitudinal motion. This methodology emerged with the ascension of electric vehicles. With two or more independent electric driven-wheels, the control possibilities are numerous [Ataei et al., 2019].

To optimally distribute the torque between wheels, several strategies formulated on different concepts have been proposed. They are mainly based or designed on the available friction, information about the friction ellipse, to avoid power loss, aiming improvement on the energy efficiency, or to increase handling performance [Smith et al., 2018, Chatzikomis et al., 2019, Yuan et al., 2018].

1.2.3 Envelope control

The envelope control usually uses a model-based controller to track the vehicle states into a desired point or region. A wide variety of control techniques have been explored for automotive and envelope control, ranging from classical linear techniques to more complex nonlinear methods.

The most popular actuating layout for vehicles is front-wheel steering, front-wheel drive, and brakes with a predefined brake-pressure proportion between the front and rear axles. The majority of works focus on operating these inputs in order to automatize the vehicle motion or automatize the act of driving. The first control applications we can find in the literature are those based on linearized models, especially in steady-state conditions. Due to its relative simplicity, lower computational resources demand, and the existence of a well-developed linear control theory, the expressive use of linear models is evident. For instance, the steering angle control problem to maintain the vehicle in the desired yaw rate was solved using a linear quadratic regulator (LQR) controller in [Park et al., 2001], pole placement in [Ackermann, 1990], PID controller in [Li et al., 2009], and the H_2 optimal controller [Rong-hui et al., 2007].

As new technologies become available and with the immersion of electric vehicles into the academy, naturally, these approaches soon advanced to more sophisticated and complex methodologies. To incorporate the nonlinear vehicle behavior under different operating conditions, nonlinear control strategies have been explored based on different structures such as in a model predictive control [Yuan et al., 2016], bifurcation analysis [Rossa and Mastinu, 2018], sliding modes control [Tota et al., 2018] and backstepping control [Depature et al., 2017].

A more recent trend in vehicle control is based on drifting. The inspiration behind this methodology is that it can drive a vehicle along a given path while utilizing the tire saturation without losing control, i.e., at the limits of handling. The implication for that is, with a full understanding of the friction limits, the closed-loop formulation can provide steering and throttle commands that drive the vehicle safely in a situation where other approaches would result in loss of control [Kegelman et al., 2016]. Exploring the new allowable window of operating conditions that would otherwise be infeasible have appeared recently in the literature [Kapania et al., 2016, Laurence et al., 2017, Goh et al., 2019].

1.3 Motivation

Numerous researches have been focused on and undertaken to improve the act of driving. As a consequence, considerable attention and efforts have been given to the development

of control strategies. As new technologies are being applied to vehicles, sensing and actuators' capabilities are getting better and accessible. This authority enables many new applications that will further improve safety, performance, and comfort [Lefèvre et al., 2015].

Within this field, despite all advantages that recent technologies incorporate to vehicle stability, progress on these systems naturally depends on our ability to understand the vehicle nonlinear behavior, especially under the influence of concurrent inputs, such as wheel torque allocation and steering angle commands.

Implementing controllers for such structures, individually or in some combinations, can result in actuator redundancy or in challenging problems of control allocation. Often, these dependencies may cause a lack of transparency or impairment of the overall vehicle motion [Johansen and Fossen, 2013]. In fact, it is generally difficult to produce a perceptive understanding of the vehicle response under a more complex control structure, moreover, predicting the combined effect of distinct inputs remains a challenge [Ataei et al., 2018].

A number of works are dedicated to improving vehicle handling and motion stability [Wang and Chen, 2018, Kati et al., 2018, Galluppi et al., 2019]. However, most of them are based on linearized models and a large majority of existing methods are not concerned about providing stability certificates.

In the current thesis, these exact questions are studied. The stability analysis and the control design synthesis are evaluated under an optimization problem. By means of Lyapunov's theorem along with the sum-of-squares programming advancements, stability certificates can be provided.

The analysis is mainly based on the region of attraction (RoA). Estimating and further enlarging the region of attraction is an important subject of study. The RoA is a safe subset of the state space in which the equilibrium point is stable. In other words, it describes the boundary on how far from equilibrium the vehicle can reach where stability is assured. Such characteristics respond if an unintentional spin is still safe or will lead to divergence. For instance, vehicle stability can be ensured by limiting the vehicle's motion to a portion of the state space, however, knowing these exact portions and limits is far from trivial.

The sum-of-squares programming framework explored in this thesis is also extended to a state feedback control problem. Now, we wish not only to estimate but also to design a control law that better expands the RoA while accounting for input saturation.

1.3.1 Sum-of-squares programming

Due to recent advances in polynomial optimization, based on sum-of-squares (SOS) relaxations, significant research has been performed on the development of Lyapunov-based analysis tools tractable by convex optimization [Parrilo, 2003]. The SOS technique effec-

tiveness has been extensively explored for computing efficient solutions to various complex problems, such as regions of attraction [Tacchi et al., 2018]; reachability sets [Jones and Peet, 2019]; reach-avoid sets [Landry et al., 2018]; and nonlinear control synthesis [Singh et al., 2020].

Regarding the local asymptotic stability problem, a challenging question is to establish suitable estimates for the region of attraction. A common way of obtaining RoA estimates is searching for an inner approximation given by the largest level set of a Lyapunov function (LF) such that the stability conditions hold. In the case of polynomial systems, several approaches have been recently proposed to deal with such a problem.

One subject of interest is the RoA computation for systems subject to modeling uncertainties. In [Topcu et al., 2010], an SOS-based algorithm combined with a branch-and-bound strategy was proposed. The system was described by vector fields affinely dependent on polynomial functions of the uncertain parameters. In [Iannelli et al., 2019b] the local stability analysis problem of uncertain systems is formulated by defining an augmented system comprising the polynomial and linear time-invariant system. An alternative solution for the dependence of the LF on the uncertain parameters is proposed in [Wang et al., 2020a]. The approach begins with an inner RoA estimation that is further improved by iterative computations of a parameter-dependent function.

Under the assumption of nominal vector fields, the problem of finding the RoA inner estimate has received considerably more attention. The technique usually leads to bilinear matrix inequality constraints and iteration schemes are employed [Jarvis-Wloszek et al., 2005, Papachristodoulou, 2005, Tan and Packard, 2008, Chesi, 2011b]. The problem of computing inner bounds on the RoA is presented in [Topcu et al., 2008]. The approach is intended to find the best possible estimate for the RoA using the largest level set of an LF. A variant of the algorithm is proposed in [Iannelli et al., 2019a], which aims to reduce the conservatism obtained using the invariant sets. The computational efforts and improvement on the level set estimates are reported.

The significance of these results, in conjunction with the availability of publicly available tools designed to convert the SOS relaxations into linear matrix inequalities, promoted the stability analysis and RoA estimation across disparate engineering fields, such as in-flight control [Chakraborty et al., 2011, Cunis et al., 2020], switched systems [Zheng et al., 2018], robotic systems [Ahmadi and Majumdar, 2019], and power systems [Izumi et al., 2020]. It is noteworthy, with certain restricted assumptions, the SOS approach has also been applied for non-polynomial dynamical systems [Pitarch et al., 2014, Chen et al., 2015, Wang et al., 2020b].

1.3.2 Region of attraction analysis for nonlinear vehicle dynamics

Within the vehicle stability field, early works have mainly relied on linear systems theory to guarantee local stability. Lyapunov's second method was first used in [Johnson and Huston, 1984] with a linearized vehicle model. The RoA estimate was then found manually by calculating the largest level set of the candidate function that fits within the region. Since then, Lyapunov-based methods were used aiming for more accurate and representative estimates of the RoA [Sadri and Wu, 2012, Németh et al., 2016].

In [Németh et al., 2014, 2016], the authors applied the SOS technique to the lateral stabilization problem of vehicle systems. A variant of the bicycle model is written and a two-stated slip angle dynamics is obtained. The tire forces are approximated by a 10th order polynomial function and the lateral stability is verified for given peak-bounded control input. In [Tamba and Nazaruiddin, 2018], an improvement is proposed for the polynomial tire force approximation and the estimated RoA is demonstrated for a second-order LF. The result appears conservative with similar representativeness of a neighborhood analysis, i.e., through the system linearization at the equilibrium.

A generalization is proposed in [Drummond et al., 2018] for refinement on the Lyapunov function candidates. The work deals with rational LF, which leads to tractable numerical solutions of polynomial Lyapunov inequalities. A simplified vehicle model is used for the relaxed RoA estimation and the results show some important conservatism.

In [Masouleh and Limebeer, 2016], the tire forces are approximated by a third-order polynomial function and the lateral vehicle model is written in terms of lateral velocity and yaw rate. A further improvement of this work is proposed in [Masouleh and Limebeer, 2017] where a rational polynomial approximation is developed. The rational representation allows for a better vehicle model approximation and an overall model accuracy is achieved. Additionally, the influences of different vehicle parameters and driving conditions on stability are presented.

Drawbacks of these approaches are the narrow range of validity, associated with the vehicle model, and the conservativeness in the estimation, due to inner approximation. Furthermore, the potential of the sum-of-squares programming for the control synthesis problem was not explored.

1.4 Scope and Objectives of the Work

For road vehicles, loss of stability may have critical safety implications. It is important to study the vehicle stability for secure and reliable maneuvers accomplishment. Simply determining whether the car, in a certain maneuver, is stable does not offer a complete portrait of how far the system is from the stability boundary. By finding the region of

attraction around the equilibrium point of the nonlinear system, we can determine the direction and dimension of the external disturbance that will cause the vehicle to cross into the unstable region.

In this context, the purpose of this thesis is to take advantage of such SOS programming advancements to investigate ground vehicles, mainly driven through stability analysis and control synthesis. Three specific objectives are listed:

- Address the region of attraction estimation of a nonlinear single-track vehicle model using the sum-of-squares programming. This includes writing the model as polynomial vector fields that must capture the nonlinearities inherent to the model.
- Address the SOS control synthesis. Explicitly synthesize a polynomial state feedback controller with input saturation to enlarge the provable region of attraction.
- Experimentally validates the SOS-based controller. This includes an experimental characterization of a scaled vehicle platform whose dynamics are similar to those of a full-sized vehicle.

1.5 Thesis Outline

The remainder of this thesis is arranged as follows.

Chapter 2: Vehicle Modeling

The focus of Chapter 2 is on modeling the vehicle dynamics' main aspects. It includes the fundamental equations of motion and tire models as well as statements of important simplifications, approximations, and linearizations.

Specifically, the chapter describes a modified version of the “bicycle” model: a two-state model of the lateral dynamics that incorporates the rear-drive force, resulting in a yaw moment input. An investigation is carried out to show that the proposed model indeed captures the relevant aspects of the vehicle motion and, therefore, meets the desired requirements.

Chapter 3: Mathematical Preliminaries

Chapter 3 gives a brief background on polynomials theory, introduces the important properties and concepts, and provides the mathematical preliminaries that will attain the needs for the work development. Central to the thesis is the Positivstellensatz, a theorem in real algebraic geometry that forms the pillars for the sum-of-squares theory. The theorem is exploited for the SOS program synthesis in the later chapter.

Chapter 4: Local Stability and Controller Synthesis

Chapter 4 shows the essential relationship between the existence of certain polynomials and convex optimization. The problem of certifying local stability is presented by means of Lyapunov's theorem along with the Positivstellensatz identity. To solve the resulting

SOS restrictions, we must apply the block coordinate descent method, resulting in an iterative procedure.

The algorithm shows how to search for Lyapunov functions to demonstrate local asymptotic stability and estimate the region of attraction. The approach is then extended to the control synthesis problem where the main objective is to expand the regions with a state feedback controller.

An important aspect of the SOS design tool is that the system must be written in an input-affine form. A workaround of this issue is discussed and some examples are provided for better understanding.

Chapter 5: RoA Estimation and State Feedback

Chapter 5 addresses the lateral stabilization problem of a nonlinear single-track vehicle model. The tire forces are approximated using rational functions that are shown to capture the tire's nonlinearities significantly better than polynomial functions.

The objective is to estimate the largest state-space region such that the closed-loop vehicle lateral stability can be guaranteed. The sum-of-squares programming technique is applied to find these maximum invariant sets while accounting for steering and yaw moment input saturations. The algorithm allows the region of attraction to be approximated by a level set of a Lyapunov function and the computation of polynomial state feedback control laws. The method is applied for both straight-line motion and cornering maneuver. Finally, a Monte-Carlo analysis is presented to show that the proposed SOS-based methodology can be used as a valid analysis and design tool considering a real vehicle application.

Chapter 6: Experimental Evaluation

Chapter 6 describes the use of 1:5-scale vehicle prototyping in evaluating state-of-the-art algorithms, particularly to demonstrate and facilitate application in advanced vehicle control and sensing systems. This test-bed platform, whose lateral dynamics are similar to those of a full-sized vehicle, is used to validate the polynomial controller.

Preliminarily, an identification process is proposed to determine the unknown model parameters necessary to correctly describe the vehicle behavior. The mathematical model, validated through a series of matching experiments, is then used for further analysis and control purposes. The SOS control design is employed to synthesize polynomials control laws that are verified experimentally.

For each presented characterization, a wide set of experiments were carried out using the scaled vehicle platform. A persistent agreement between expected (simulated) and achieved (measured) lateral response was obtained. The results demonstrate a systematic consistency regarding the platform test-bed and the behavior described by the mathematical model, as well as the predictions made through the SOS technique.

Chapter 7: Conclusion

Chapter 7 provides a summary of the thesis. The key characteristics of the region of

attraction estimation and control synthesis are exposed. The dissertation concludes by presenting future possible research directions, including improvements of the proposed vehicle model and the inclusion of performance criteria into the synthesis problem.

2 Vehicle Modeling

2.1 Introduction

A vehicle is a complex system bringing together a large number of mechanical and electronic elements. Broadly speaking, its motion dynamics can be divided into two subsystems. The first is the vehicle body motion described by the rigid body dynamics and kinematics. The second is given by the tire-ground interaction, which is the primary source of forces that moves the vehicle.

Depending on the required application, different vehicle models can be used. For a simulator design, modeling efforts are concentrated on reproducing as precisely as possible the behavior of individual vehicle components, comprehending vertical, translational, and rotational movements. For control, sensing, and estimation, a relatively simple three-state planar or even the reduced bicycle model can capture the desired motion. Besides, the model can be largely simplified by linearizing the vehicle around an arbitrary point, neglecting nonlinearities, allowing applications through the vastly and well-established tools of linear control theory [Rajamani, 2011].

Regardless of the model fidelity used for analysis, in practice, the relative complexity of the selected model should facilitate simple analysis techniques such as phase portraits, numerical integration and stability of equilibrium points. A major aspect presented in this chapter is the proper selection and approximation of the ordinary differential equations (ODEs) into a suitable model that must be written as polynomial vector fields. Ideally, the system should achieve an appropriate balance between intuitive simplicity and model fidelity.

2.2 Planar Model

The analysis and control design in this thesis rely on variants of a relatively simple planar vehicle model. We begin presenting the four-wheel planar model, depicted in Figure 2.1. Usually, there are two versions of the bicycle model in literature, with two and three states. The state vector is described in terms of the vehicle's longitudinal velocity u , lateral velocity v , and yaw rate r , this latter is the rotational velocity around the z-axis.

Moreover, all of them are specified at the center of gravity (CG)

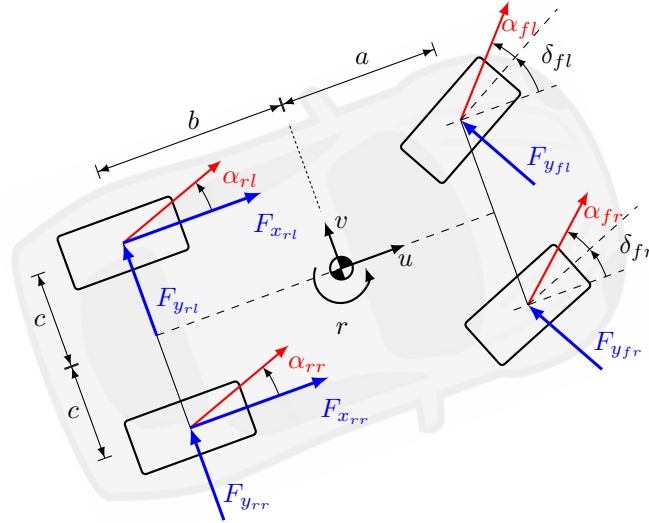


Figure 2.1. Four-wheel planar vehicle model.

By inspection of Figure 2.1, the lateral and longitudinal equations of motion are derived by analyzing the balance between forces and moments (Newton-Euler equations) in x , y and z -axis.

$$\begin{aligned}
 m(\dot{u} - rv) &= F_{x_{rl}} + F_{x_{rr}} - F_{y_{fl}} \sin \delta_{fl} - F_{y_{fr}} \sin \delta_{fr}, \\
 m(\dot{v} + ru) &= F_{y_{rl}} + F_{y_{rr}} + F_{y_{fl}} \cos \delta_{fl} + F_{y_{fr}} \cos \delta_{fr}, \\
 I_z \dot{r} &= a(F_{y_{fl}} \cos \delta_{fl} + F_{y_{fr}} \cos \delta_{fr}) - b(F_{y_{rl}} + F_{y_{rr}}) + c(F_{x_{rr}} - F_{x_{rl}}),
 \end{aligned} \tag{2.1}$$

where m is the vehicle mass, $F_{y_{ij}}$ and $F_{x_{ij}}$ are lateral and longitudinal forces. Subscripts $i \in \{f, r\}$ denotes front and rear wheels and $j \in \{l, r\}$ left and right quantities. I_z is the vehicle's yaw inertia and δ_{ij} is the tire steering angle. Distances a and b are measured from CG to front and rear axles, respectively, and c is half the distance between wheels on the same axle.

The four-wheel planar model incorporates rolling and pitching motion of the chassis. Since this dissertation is focused primarily on analyzing deviations around a steady-state cornering of the vehicle, the effects of load transfer, induced by those motions, can be neglected. As discussed in subsequent sections, this simplification brings simplicity and facilitate further developments while keeping model fidelity [Rajamani, 2011, Liu, 2013].

Also observe that this work is focused upon a vehicle with rear-wheel drive. To include the drive forces, that will be used for control design, we propose a model adaptation. We follow a modified version of the traditional bicycle model that incorporates the differential torque control at the rear axle.

From Figure 2.2, it is clear how we integrate the differential torque into the bicycle model. It should worth mentioning that the differential torque can only be achieved if we

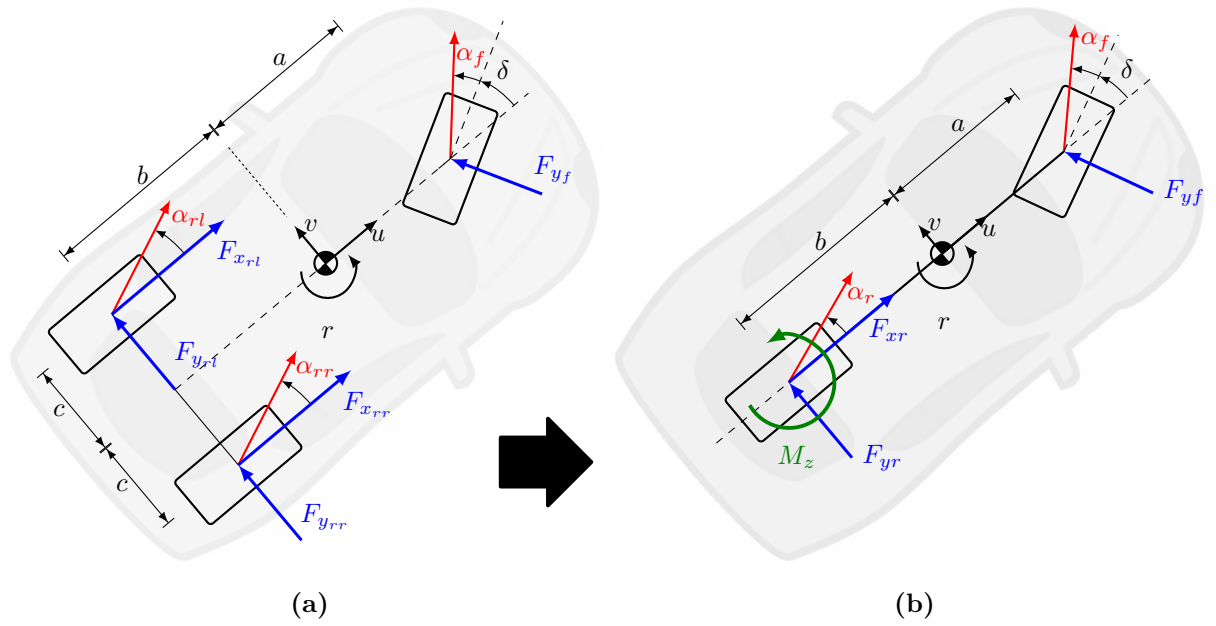


Figure 2.2. Modified bicycle model. In (a) the rear tire is expanded to show the independent longitudinal force inputs and (b) the bicycle model with an equivalent rear axle and a yaw moment input term.

are able to control the torques at each of the rear wheels individually, which is typically the case of electric vehicles driven by independent electric motors.

The problem of optimally distributing the torque between wheels is commonly denoted in literature by torque vectoring [Xu et al., 2019]. Differential torque control is intriguing from a vehicle control standpoint because it enables an additional way to generate a yaw moment. Moreover, different architectures also provide a range of control combinations, such as torque allocation between axles (front and rear), between wheels of the same axle (left and right), or a combination among them.

For the rear-wheel-drive layout depicted in Figure 2.2, the total yaw moment amount M_z generated by the independent rear drive wheels is

$$M_z = c(F_{x_{rr}} - F_{x_{rl}}). \quad (2.2)$$

In a similar form, the resulting longitudinal and lateral forces are given by the sum of the respective tire forces in the same axle

$$\begin{aligned} F_{xi} &= (F_{x_{ir}} + F_{x_{il}}), \\ F_{yi} &= (F_{y_{ir}} + F_{y_{il}}), \quad i \in \{f, r\}. \end{aligned} \quad (2.3)$$

In summary, the proposed bicycle model assumes a single tire at each axle with twice the force capability of the individual tires and a yaw moment input term that arises as

the result of the differential drive forces.

The bicycle equations of motion is derived by considering the lumped axles. Substituting (2.3) and (2.2) into (2.1), we have

$$\begin{aligned} m(\dot{u} - rv) &= F_{xr} - F_{yf} \sin \delta, \\ m(\dot{v} + ru) &= F_{yf} \cos \delta + F_{yr}, \\ I_z \dot{r} &= aF_{yf} \cos \delta - bF_{yr} + M_z. \end{aligned} \quad (2.4)$$

To analyze the lateral vehicle stability, we may simplify the dynamical model (2.4) considering a rectilinear uniform movement. A constant longitudinal velocity u_0 implies in $\dot{u} = 0$, resulting in the decoupling of longitudinal and lateral dynamics. The corresponding lateral model is then

$$\begin{aligned} m(\dot{v} + ru_0) &= F_{yf} + F_{yr}, \\ I_z \dot{r} &= aF_{yf} - bF_{yr} + M_z. \end{aligned} \quad (2.5)$$

The lateral forces play an important role in this work. The above discussion presents the tire's fundamentals, modeling, and simulation.

2.3 Tire Fundamentals

The response and performance of a vehicle are mainly influenced by the mechanical force and moment generating characteristics of the tires. Therefore, an adequate model is an essential component when it comes to vehicle stability analysis.

In the literature, one can find modeling approaches that concentrate their efforts to capture the more complex aspects of the tire, which include methodologies based upon finite element analysis [Patel et al., 2015, Ballo et al., 2018]. For control purposes, however, these techniques are prohibitively complex due to the computational cost, development time, and an excessively large number of required parameters. Instead, variants of a relatively simple Brush tire and Pacejka model are used in an endeavor to capture the most important aspects of tire behavior.

In these models, the lateral force generated by the tire is essentially dictated by a combination of two factors: the force demanded from the tire when cornering and the total force available from friction.

Lateral force can only be generated in a situation where there is sufficient force available from friction to feed the needs. Two main components usually govern the force available from friction, vertical load F_{zi} and available friction coefficient μ_i . The product $\mu_i F_{zi}$ delivers the maximum available force that the tire can reach.

The force demanded when cornering is the result (prominently) of the tire slip angle α_i . The slip angle α_i is characterized by the absolute speed components of the wheel,

computed at the local wheel coordinate system or wheel frame. From Figures 2.1 and 2.2, one can see α_i is the angle between the longitudinal u_w and lateral v_w velocity components of the absolute wheel velocity,

$$\alpha_i = \arctan \frac{v_w}{u_w}. \quad (2.6)$$

In Figure 2.3 we illustrate our discussion by plotting the lateral forces for two analytical models, the Pacejka and Brush tire models [Pacejka, 2012] and their linear approximation.

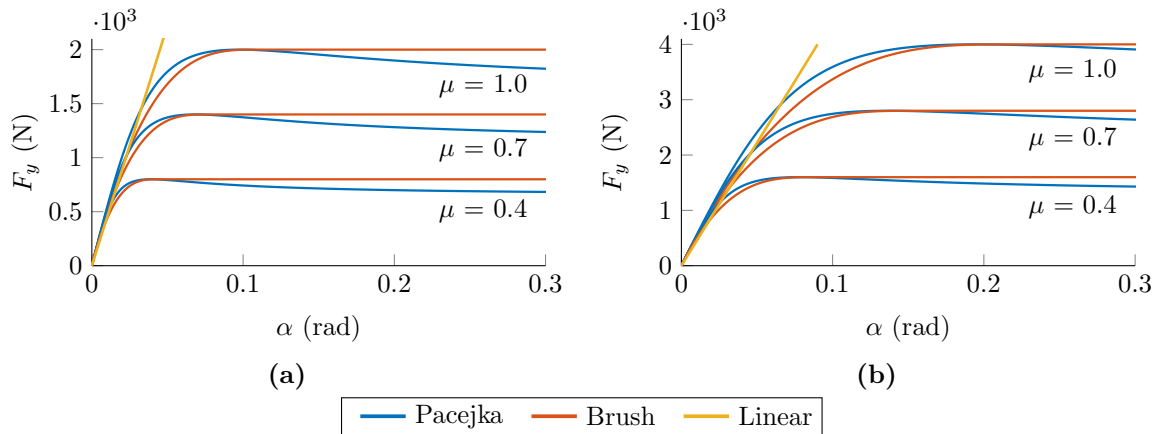


Figure 2.3. Corresponding lateral tire characteristic curve for Pacejka and Brush models. The results are shown for three values of friction coefficient μ . In (a) vertical load F_z is 2 kN and in (b) 4 kN.

The slip angles are a response of the steered wheels that translate to a lateral deflection at the tire's rubber elements in the contact patch (between tire and road). This generates a reaction force that increases linearly from zero to its maximum value, $\mu_i F_{zi}$. Beyond the maximum value, the tire is said to be saturated. In this case, increasing the slip angle does not lead to an increase in lateral forces.

Slip angle can be analytically determined by considering the planar motion kinematics, α_i is exactly written as

$$\alpha_f = \arctan \left(\frac{\cos \delta (v + ar) - \sin \delta u_0}{\cos \delta u_0 + \sin \delta (v + ar)} \right), \quad (2.7)$$

$$\alpha_r = \arctan \left(\frac{v - br}{u_0} \right).$$

Given that we are supposing constant longitudinal speed u_0 and since $u_0 \gg v$, we may assume sufficient small values of α_i such that the approximation $\arctan(\alpha_i) \approx \alpha_i$ is

valid [Rajamani, 2011]. The expression is then rewritten as

$$\begin{aligned}\alpha_f &= \frac{v + ar}{u_0} - \delta, \\ \alpha_r &= \frac{v - br}{u_0}.\end{aligned}\tag{2.8}$$

Observe that this assumption is just a simplification of (2.7), the tire forces nonlinearities are still taken into account through the tire models.

For the purposes of this dissertation, we will concentrate our attention on two analytical models that are briefly described: the Brush tire model and the Pacejka tire model.

2.3.1 Brush tire model

The Brush model assumes a rigid carcass surrounded by deformable and flexible brushes composed of elastic particles. The deflection of these elements along with the length of the contact patch produce a reactive force per unit of length available from friction.

There are multiple variants of brush tire models in the literature that show different substructures defining the interaction between the brushes and the road. Here we follow the model presented in [Pacejka, 2012, Ch. 3].

The analytical approximation that describes the nonlinear relationship between the tire force and slip angle is

$$F_{yi} = \begin{cases} -C_\alpha \tan \alpha_i \left(1 - \frac{C_\alpha}{3\mu_i F_{zi}} |\tan \alpha_i| + \frac{C_\alpha^2}{27\mu_i^2 F_{zi}^2} \tan^2 \alpha_i \right) & |\alpha_i| \leq \alpha_{sl_i}, \\ -\mu_i F_{zi} \text{sign}(\alpha_i) & |\alpha_i| > \alpha_{sl_i}, \end{cases}\tag{2.9}$$

with α_{sl_i} defined as

$$\alpha_{sl_i} = \arctan \left(\frac{3\mu_i F_{zi}}{C_\alpha} \right).$$

where C_α is the tire cornering stiffness, a measure of the tire ability to resist deformation, and α_{sl_i} is the slip angle threshold needed to reach the full sliding condition.

2.3.2 Pacejka tire model

The most common empirical model is the Pacejka tire model, also known as the so-called *Magic tire formula*, developed by Hans Pacejka [Pacejka, 2012, Ch. 4]. It is a data-driven empirical model, based on a trigonometric formula, which is capable of matching experimental data effectively. It provides coefficients which have clear relationships of

the curves to be fitted, such as typical shape and peak magnitude. The magic formula is written as

$$F_{yi}(\alpha_i) = D \sin(C \arctan(B(1 - E)\alpha_i + E \arctan(B\alpha_i))), \quad (2.10)$$

where constants B , C , D and E are the semi-empirical parameters. B corresponds to the stiffness factor that adjusts the initial derivative, C limits the sine function, defining the curve shape, D is the maximum value the force can reach, and factor E is introduced to control the curvature at the peak value. These parameters must be set to fit the measured data on the tire model.

2.4 Four-Wheel and Bicycle Model Analysis

In the last sections, we discussed the mathematical manipulations used to write the bicycle model. Here we show and compare both, four-wheel planar and bicycle models, in order to discuss the impact of these approximations. Moreover, we highlight their main characteristics.

The Pacejka model is a relatively more complex model, however, it is recognized as capable of presenting an excellent approximation for experimental forces data. On the other hand, the Brush model is simpler and depends only on the tire C_α parameter, in contrast to the four Pacejka parameters.

When experimentally working with a vehicle application, the parameter that can be estimated with moderate effort is exactly C_α . Therefore, in practice, the knowledge of this single parameter allows the straightforward employment of the Brush model.

For these reasons, we use the Pacejka model for simulation purposes with the sole objective of bringing greater representability of the vehicle's response in a simulation environment. The Brush model, on the other hand, will be used for analysis and control design.

2.4.1 Review and comparison

With the four-wheel planar motion, the load transfer effect for a steady-state maneuver can be determined as a function of the vehicle states. Changes in wheel loads, resulting from lateral acceleration, are formulated by applying force and momentum analysis. The vertical force distribution, derived from the two-dimensional roll and pitch dynamics, is illustrated in Figure 2.4.

With a rigid body assumption, the vertical forces distribution of a four-wheel planar

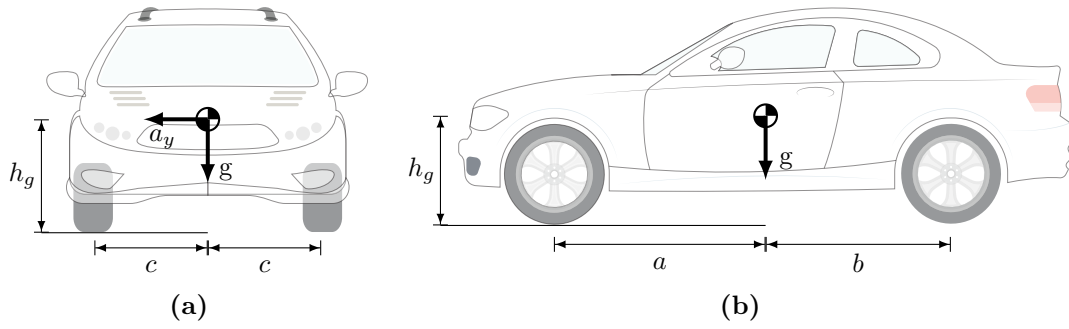


Figure 2.4. Two-dimensional vertical force distribution considering a steady-state condition.

model is

$$\begin{bmatrix} F_{zfl} \\ F_{zfr} \\ F_{zrl} \\ F_{zrr} \end{bmatrix} = \begin{bmatrix} c & -c & c & -c \\ 1 & 1 & 1 & 1 \\ a & 0 & -b & 0 \\ 0 & a & 0 & -b \end{bmatrix}^{-1} \begin{bmatrix} h_g m a_y \\ m g \\ 0 \\ 0 \end{bmatrix} \quad (2.11)$$

where $h_g = \bar{h}_g - \frac{mg}{4k_s}$, in which \bar{h}_g is the distance from the vehicle extremity to the ground with the suspension length in rest (nominal suspension length). The centripetal acceleration is defined as $a_y = (\sqrt{u_0^2 + v^2}) r$ and g is the gravitational acceleration.

The first equation of (2.11) ensures the balance between vertical forces and lateral acceleration. The second equation ensures the four wheels are in a vertical equilibrium. Third and fourth equations provide zero moment balance between front and rear wheels, or equivalently, zero longitudinal acceleration due to the constant longitudinal velocity.

For the bicycle model, load transfer is considerably simplified. Roll motion is neglected, resulting in static vertical forces. The lumped front and rear vertical forces are

$$\begin{aligned} F_{zf} &= b m g / (a + b), \\ F_{zr} &= a m g / (a + b). \end{aligned} \quad (2.12)$$

The complete vehicle model is assembled substituting the vertical forces and the tire models into (2.5), to create the bicycle model, or into (2.1) to assemble the four-wheel planar model.

In Figure 2.5, we present the trajectories achieved using both models. The figure depicts the existence of three equilibrium conditions and a local stable region. It goes without saying that in this comparison, despite all the linearizations and simplifications necessary to assemble the bicycle model, it presents a proper alignment between the bicycle and the four-wheel model response. In Figure 2.5a, we show a straight running scenario, i.e., the steering angle is set to zero. In this case, lateral acceleration is con-

siderably diminished, reducing the effect of load transfer, which results in well-aligned trajectories. On the other hand, for a cornering maneuver with a constant steering angle, shown in Figure (2.5b), one can note a slight disparity among the trajectories where the differences mainly arise across the unstable region. Despite these discrepancies, the equilibrium points of the two systems are equivalent and the trajectories of the stable region are coincident.

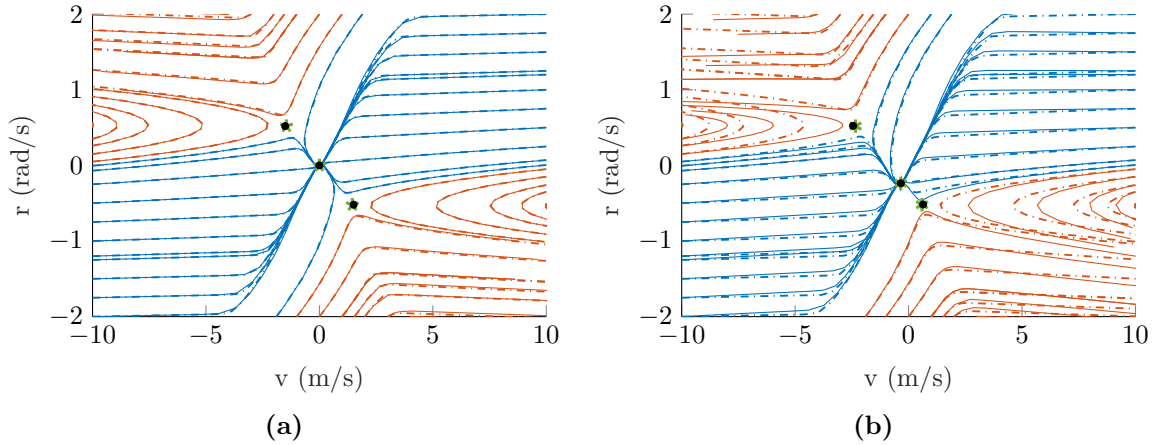


Figure 2.5. Phase portrait of the approximated bicycle model (dashed lines) and the complete planar vehicle model (solid lines). The vehicle is set at constant longitudinal velocity u_0 of 10 m/s. Green stars and black dots are equilibrium points of the bicycle and planar models, respectively. In (a) steering angle is set to 0 degrees and in (b) steering angle is set to -5 degrees.

As we are interested in estimating the region of attraction around the stable equilibrium point, we can confidently use the bicycle model without losing meaningful behavior properties. The bicycle model, in terms of accuracy and representation, correctly describes the trajectories of the system.

2.5 Linear model

Finally, we can describe the vehicle motion in its simplest version. At low levels of lateral excitation, a linear tire model efficiently describes the behavior of the forces (see Figure 2.3). This fact results in a useful mathematical description to develop a linearized version of the bicycle model [Rajamani, 2011]. It assumes a direct relationship between the tire slip angle and its lateral force

$$\begin{aligned} F_{yf} &= 2C_\alpha\alpha_f, \\ F_{yr} &= 2C_\alpha\alpha_r. \end{aligned} \tag{2.13}$$

For the nonlinearities induced by the steering angle δ , the small-angle approximation $\cos \delta \approx 1$ is used, a reasonable assumption within the context of the vehicle in the study.

For a steering angle range of $|\delta| \leq 22^\circ$, the approximation on $\cos \delta$ induces a relative error less than 7.85%.

The substitution of slip angles (2.8) into the linear tire force equations (2.13) and then into (2.4) yields the differential equations

$$\begin{aligned} \dot{v} &= \underbrace{\frac{-4C_\alpha}{mu_0}}_{a_{11}} v + \underbrace{\left(\frac{2C_\alpha(b-a)}{mu_0} - u_0 \right)}_{a_{12}} r + \underbrace{\frac{2C_\alpha}{m}}_{b_{11}} \delta \\ \dot{r} &= \underbrace{\frac{2C_\alpha(b-a)}{I_z u_0}}_{a_{21}} v + \underbrace{\frac{-2C_\alpha(a^2+b^2)}{I_z u_0}}_{a_{22}} r + \underbrace{\frac{2C_\alpha a}{I_z}}_{b_{21}} \delta + \underbrace{\frac{1}{I_z}}_{b_{22}} M_z \end{aligned} \quad (2.14)$$

where a_{ij} and b_{ij} are the A and B matrices elements of the generalized form

$$\dot{x} = Ax + Bu, \quad (2.15)$$

where $x = [v, r]^T$ and $u = [\delta, M_z]^T$. Note that, just as before, longitudinal velocity u_0 is not a vehicle state, but rather a model parameter. Matrices A and B are therefore

$$A = \begin{bmatrix} \frac{-4C_\alpha}{mu_0} & \frac{2C_\alpha(b-a)}{mu_0} - u_0 \\ \frac{2C_\alpha(b-a)}{I_z u_0} & \frac{-2C_\alpha(a^2+b^2)}{I_z u_0} \end{bmatrix}, \quad B = \begin{bmatrix} \frac{2C_\alpha}{m} & 0 \\ \frac{2C_\alpha a}{I_z} & \frac{1}{I_z} \end{bmatrix}.$$

For a more detailed and comprehensive analysis of the lateral vehicle model and its linearization, see [Rajamani, 2011, Chapter 2].

In the context of this thesis, the linearized system is used to provide the quadratic Lyapunov function candidates (V_0) derived from the linearized vehicle model associated with the Lyapunov equation. Besides that, (2.15) is used to compute the LQR gains used for initial candidates \bar{K}_0 .

2.6 Final Remarks

In the current chapter, different dynamic models for vehicles are presented in a variety of complexity levels. Two steady-state tire forces models have been discussed: the brush model and the Pacejka Magic Formula. Most remarkably, the chapter shows the nonlinear single-track bicycle model response matches those achieved with the more complex four-wheel model.

3 Mathematical Preliminaries

In this chapter, we present the mathematical background and preliminaries that are the heart of the theory employed in this thesis. We first recall the standard representation of polynomials, sum-of-squares polynomials, and monomial basis. The chapter proceeds by introducing the Positivstellensatz, a central theorem in real algebraic geometry that provides an important identity that will be explored in later chapters.

We then briefly describe the SOSTOOLS, a software that facilitates the search for a sum of squares decomposition given a polynomial structure or constraints.

3.1 Background on Polynomials

One of the most important mathematical objects in this thesis is the polynomial. We will define the set of multivariate polynomials in n variables and with real coefficients as $\mathbb{R}[x_1, \dots, x_n] = \mathbb{R}[x]$. Let us start with the fundamental definitions.

Definition 1 Let $x = (x_1, \dots, x_n)$ and $\alpha = (\alpha_1, \dots, \alpha_n)$ with $x \in \mathbb{R}^n$ and $\alpha \in \mathbb{N}^n$. A **monomial** in n variables is a function that maps $m_\alpha(x) : \mathbb{R}^n \rightarrow \mathbb{R}$ and defined as $m_\alpha(x) = x^\alpha = x^{\alpha_1} x^{\alpha_2} \dots x^{\alpha_n}$. The degree of a monomial is identified as $\deg(m_\alpha) = \sum_{i=1}^n \alpha_i$.

For a general pair of n variables with degree $d = \deg(m_\alpha)$, the monomial list will be a vector with $\binom{n+d}{d}$ elements. As an example, with $n = 2$ and $d = 2$, the vector of all monomials is $[1, x_1, x_2, x_1^2, x_1x_2, x_2^2]^T$.

Definition 2 A **polynomial** in (x_1, \dots, x_n) is defined as a linear combination of a finite set of monomials $\{m_{\alpha_j}(x)\}_{j=1}^k$ with real coefficients $\{c_j\}_{j=1}^k \in \mathbb{R}$. A polynomial $f \in \mathbb{R}[x]$ is written as

$$f(x) = \sum_{j=1}^k c_j m_{\alpha_j}(x). \quad (3.1)$$

The degree of $f(x)$, denoted by $\deg(f(x))$, is defined as the maximum degree of the monomials in it. Or, equivalently, $\deg(f(x)) = \max_j \deg(m_{\alpha_j})$ associated with the non-zero c_j .

A concept over polynomials that will play a central role in this work is the notion of the sum-of-squares. Its importance relies on the fact that an explicit expression of f as a sum of squares is a certificate of positivity for f .

3.1.1 Sum-of-squares polynomials

As the name might suggest, a polynomial is SOS if it can be represented as sums of squares of other polynomials. If a polynomial in n variables can be written as a sum of squares components of real polynomials, then clearly it must take only nonnegative values in \mathbb{R}^n . In fact, the SOS decomposition gives an immediate verification of the polynomial positivity on \mathbb{R}^n . Its simple and basic definition is stated as follows.

Definition 3 (*Sum of squares polynomial*) We denote by $\Sigma_n \subset \mathbb{R}[x]$, $x \in \mathbb{R}^n$, the set of polynomials that can be decomposed as the sum of square (SOS) of polynomials. A polynomial $p \in \mathbb{R}[x]$ admits a sum of squares decomposition if there exists polynomials f_i , $i = \{1, \dots, N\}$ such that

$$\Sigma_n = \left\{ p(x) \in \mathbb{R}[x] \mid p(x) = \sum_{i=1}^N f_i^2(x), \quad f_i(x) \in \mathbb{R}[x], \quad i = \{1, \dots, N\} \right\}. \quad (3.2)$$

From (3.2) it is clear that, given any $p \in \Sigma_n$, then $p \geq 0$ on \mathbb{R}^n and must always be of even degree. It is also known that p is a sum of squares if and only if there exists a positive semidefinite matrix Q and a finite vector of monomials $Z(x)$ such that

$$p(x) = Z(x)^T Q Z(x). \quad (3.3)$$

This representation is utilized to express a sufficient condition for the positive semidefiniteness of any SOS polynomial in terms of the so-called Gram matrix Q . Polynomial $p(x)$ being an SOS is equivalent to $Q \geq 0$.

Searching for the equivalence between p and Q was proposed in [Powers and Wörmann, 1998]. The problem was written as one of testing emptiness of a semi-algebraic set and the verification was cast as an instance of the quantifier elimination procedure. Years later, Parrilo [Parrilo, 2003] demonstrated that searching for the existence of Q for a given p can be formulated as a convex problem using semidefinite programming.

3.2 Positivstellensatz

Having introduced SOS polynomials, we now can make the algebraic definitions that are necessary to present one of the fundamental theorems of real algebraic geometry. The

Positivstellensatz, firstly presented in [Stengle, 1974], provides an equivalence relation between the emptiness of a semi-algebraic set, composed by a finite set of polynomial equalities and inequalities, to an algebraic relationship. We begin with a few definitions that are used in the theorem.

Definition 4 Given polynomials $\{g_1, \dots, g_t\} \in \mathbb{R}[x]$, the **Multiplicative Monoid** generated by the g_i is the set of all finite or countably infinite products of g_i , including 1, defined to be the empty product. It is denoted as $\mathcal{M}(g_1, \dots, g_t)$.

For the sake of example:

$$\mathcal{M}(\phi) = 1,$$

$$\mathcal{M}(g_1) = \{g_1^{k_1} \mid k_1 \in \mathbb{Z}_+\},$$

$$\mathcal{M}(g_1, g_2) = \{g_1^{k_1} g_2^{k_2} \mid k_1, k_2 \in \mathbb{Z}_+\}.$$

Definition 5 Given polynomials $\{f_1, \dots, f_s\} \in \mathbb{R}[x]$, the smallest algebraic **Cone** generated by the f_j is the set

$$\mathcal{C}(f_1, \dots, f_s) = \left\{ q_0 + \sum_{i=1}^{2^s-1} b_i q_i \mid b_i \in \mathcal{M}(f_1, \dots, f_s), q_i \in \Sigma_n \right\}.$$

For the sake of example:

$$\mathcal{C}(f_1) = \{q_0 + f_1 q_1 \mid q_0, q_1 \in \Sigma_n\},$$

$$\mathcal{C}(f_1, f_2) = \{q_0 + f_1 q_1 + f_2 q_2 + f_1 f_2 q_3 \mid q_0, \dots, q_3 \in \Sigma_n\}.$$

Definition 6 Given polynomials $\{h_1, \dots, h_u\} \in \mathbb{R}[x]$, the **Ideal** generated by the h_i is the set

$$\mathcal{I}(h_1, \dots, h_u) = \left\{ \sum_{i=1}^u h_i p_i \mid p_i \in \Sigma_n \right\}.$$

With these definitions we can proceed by stating the Positivstellensatz theorem

Theorem 1 [Bochnak et al., 1998, Theorem 4.4.2] Given polynomials $\{f_1, \dots, f_s\}$, $\{g_1, \dots, g_t\}$ and $\{h_1, \dots, h_u\}$, then the following properties are equivalent:

(i) The set

$$\left\{ x \in \mathbb{R}^n \mid \begin{array}{l} f_1 \geq 0, \dots, f_s \geq 0 \\ g_1 \neq 0, \dots, g_t \neq 0 \\ h_1 = 0, \dots, h_u = 0 \end{array} \right\} \quad (3.4)$$

is empty.

(ii) There exist polynomials $f \in \mathcal{C}(f_1 \dots f_s)$, $g \in \mathcal{M}(g_1 \dots g_t)$ and $h \in \mathcal{I}(h_1 \dots h_u)$ such that

$$f + g^2 + h = 0. \quad (3.5)$$

The Positivstellensatz states that, for a system of real polynomial equalities and inequalities, either there exists a solution or a certain polynomial identity that does not satisfy (3.5), certifying that no solution exists. From here on, for simplicity, we will also refer to the Positivstellensatz theorem as P-satz.

These realizations have opened the way for algorithmic analysis of nonlinear systems. The construction of an equivalent semidefinite program for computing the SOS decomposition has been subject of study in subsequent years since Parrilo's work [Parrilo, 2000, Jarvis-Wloszek, 2003, Jarvis-Wloszek et al., 2003, Anderson and Papachristodoulou, 2015].

The significance of these results allowed the development of frameworks and toolboxes that automate the conversion between SOS decompositions into semidefinite programming (SDP). This theoretical to practical improvement arose quite naturally out of the need for a parser responsible for the conversion between SOS conditions to the corresponding semidefinite program. As one may suppose, writing out the SDPs explicitly can become a complex and ungrateful task when the polynomials involved are of high orders.

In order to achieve this particular conversion, a number of software packages were created. Between the relevant ones, we can mention the SOSTOOLS [Papachristodoulou et al., 2013], Drake [Tedrake and the Drake Development Team, 2019], SOSOPT [Seiler, 2013], SMRSOFT [Chesi, 2011a] and YALMIP [Lofberg, 2009]. Throughout this work, SOSTOOLS will be used to formulate and solve all sum-of-squares programs.

Before following on, an important mention is regarded about the notation applied in this chapter and those which follows from here on. As the reader may have noticed, we often omit the polynomials arguments, i.e., polynomials $f(x)$ and $p(x)$ were also simply written as f and p , respectively. It makes the expressions apparently simple and readable. We hope this abuse of notation will not confuse the reader.

4 Local Stability and Controller Synthesis

4.1 Introduction

In this chapter, we will build on the methodology firstly introduced in [Parrilo, 2000], followed by the work of [Jarvis-Wloszek, 2003, Jarvis-Wloszek et al., 2003], and show how non-negativity conditions for polynomials can be relaxed to assume a sum-of-squares decomposition. Most importantly, how it is achieved algorithmically using semidefinite programming. The SOS programs, algorithms, and theorems stated here form the pillars of the theory that will attain the needs for the thesis.

The principle of sum-of-squares polynomials and relaxations, presented in Chapter 3, is central to the understanding of this section. It relies on the idea that testing non-negativeness of polynomials can be written as a sequence of problems with sum-of-squares decomposition, implemented via SDP.

Let us begin with the system

$$\dot{x} = f(x), \tag{4.1}$$

where $x \in \mathbb{R}^n$ is the state variables, $f : \mathcal{D} \rightarrow \mathbb{R}^n$ is a vector of polynomial state functions with $\mathcal{D} \subset \mathbb{R}^n$. Without loss of generality, it is assumed that the equilibrium point of interest $\bar{x} \in \mathcal{D}$ is at the origin of \mathbb{R}^n , therefore, $f(\bar{x}) = 0$.

Using a Lyapunov function along with SOS relaxations, we can characterize the stability of (4.1) by checking the non-negativity of a Lyapunov function, written explicitly as a polynomial function. In other words, it is possible to pose the theoretic Lyapunov stability arguments as a problem that searches for SOS polynomials that, if feasible, certifies the origin is a stable equilibrium of the system.

Here, we are interested in systems with non-global stability. In many instances, local stability analysis may be required. In practice, when dealing with physical models, such as in the robotic field, global asymptotic stability is hardly verified. Due to the nature of these systems, it is more likely to see a domain of attraction locally arranged around the equilibrium point.

4.2 Local Stability

Using the stability definitions, local asymptotic stability is verified through the existence of a Lyapunov function [Khalil, 2002, Theorem 4.1]. The conditions are stated in the following theorem:

Theorem 2 *Let $\mathcal{D} \subset \mathbb{R}^n$ be a domain containing the equilibrium point $x = 0$ of the system (4.1). Let $V : \mathcal{D} \rightarrow \mathbb{R}$ be a continuously differentiable function such that*

$$\begin{aligned} V(0) &= 0, \\ V(x) &> 0 \quad \text{on } \mathcal{D} \setminus \{0\}, \end{aligned}$$

and

$$\dot{V}(x) = \frac{\partial V}{\partial x} f(x) < 0 \quad \text{on } \mathcal{D} \setminus \{0\},$$

then the system (4.1) is asymptotically stable around $x = 0$. Moreover, any bounded region and strictly contained in \mathcal{D} , i.e., $\Omega_\gamma = \{x \in \mathcal{D} \mid V(x) \leq \gamma\}$, describes a positively invariant region that is an estimate of the region of attraction.

The algorithm presented below works to find the largest region Ω_γ , defined by a level set of the Lyapunov function, which in line with the Theorem 2 is invariant and contained in the region of attraction. The larger the region is, the more one can confidently claim the representativeness of the estimate.

This central idea of inner estimation originally firstly appeared in the context of the construction of Lyapunov functions using sum-of-squares in [Papachristodoulou and Prajna, 2002] and of a state feedback controller design in [Jarvis-Wloszek et al., 2003, Jarvis-Wloszek, 2003]. The mathematical manipulations and a slightly modified version of the *expanding interior algorithm* are discussed as follows.

4.3 Expanding Interior Algorithm

As the algorithm's name may suggest, this method obtains inner bounds approximations of the region of attraction. To fit the assumptions of Theorem 2 into an SOS program, we must restrict our search over polynomials, i.e., $V(x) \in \mathbb{R}[x]$. Moreover, we define the region \mathcal{S}_β , parameterized in β , that will be contained in a level set of the Lyapunov function

$$\mathcal{S}_\beta = \{x \in \mathcal{D} \mid s(x) \leq \beta\}, \quad (4.2)$$

where $s(x)$ is a given positive definite polynomial and $\beta \geq 0$. A representative region of attraction can be estimated if we could maximize β subject to the constraint that all points in \mathcal{S}_β converge to origin. Additionally, we benefit from the level sets of the Lyapunov function to constitute the estimated RoA. Following Theorem 2, this invariant region is defined as

$$\Omega_\gamma = \{x \in \mathcal{D} \mid V(x) \leq \gamma\}. \quad (4.3)$$

Then, imposing that \mathcal{S}_β must be contained in Ω_γ , results in the following set containment constraint

$$\{x \in \mathcal{D} \mid s(x) \leq \beta\} \subseteq \{x \in \mathcal{D} \mid V(x) \leq \gamma\}. \quad (4.4)$$

Additionally, for the third theorem's assumption, we must ensure that $\dot{V}(x)$ is negative definite in \mathcal{D} . The requirement of Theorem 2 for asymptotic stability becomes

$$\{x \in \mathcal{D} \mid V(x) \leq \gamma\} \subseteq \{x \in \mathcal{D} \mid \dot{V}(x) < 0\}. \quad (4.5)$$

If one find a $V(x)$ that satisfies the aforementioned conditions and for $\gamma > 0$ such that $x \in \mathcal{D}$, then the origin of (4.1) is asymptotically stable. Furthermore, the invariant set we can demonstrate that converges to the origin is the level set γ of $V(x)$ that is contained in \mathcal{D} . Therefore, region Ω_γ , defined in (4.3), is then our estimative of the region of attraction.

In order to find the largest estimate of the region of attraction, we must maximize β for a fixed $s(x)$ which indirectly forces region Ω_γ to grow as well. Note that this is enforced by restriction (4.4). With this approach, the level set β of $s(x)$ gives the shape of the region over we check the Lyapunov statements. For this reason, $s(x)$ is also referred to as the shaping function.

To accommodate these assumptions into a suitable SOS programming framework, it is necessary to formulate the above semi-algebraic sets and set containments into a computationally tractable SDP problem. The standard approach firstly invokes the Positivstellensatz theorem and manages to consider polynomial systems and then restrict the set of candidate Lyapunov functions to be polynomials [Jarvis-Wloszek et al., 2003, Jarvis-Wloszek, 2003].

As discussed in Section 3.2, the P-satz provides the basis of sufficient conditions to verify that a given semi-algebraic set is empty. Therefore, we can reformulate restrictions (4.2)-(4.5) as one of testing emptiness of a given set. By doing so, the problem is rewritten

as

$$\begin{aligned}
& \max_{V(x) \in \mathbb{R}[x], V(0)=0} \beta \\
& \text{s.t.} \\
& \{x \in \mathcal{D} \mid V(x) \leq 0, x \neq 0\} = \phi, \\
& \{x \in \mathcal{D} \mid s(x) \leq \beta, V(x) \geq \gamma, V(x) \neq \gamma\} = \phi, \\
& \{x \in \mathcal{D} \mid V(x) \leq \gamma, \dot{V}(x) \geq 0, x \neq 0\} = \phi.
\end{aligned} \tag{4.6}$$

If we could find any $V(x)$ such that the subsets (4.6) are indeed empty, then the Lyapunov theorem holds. Observe that the P-satz conditions are only valid for sets defined by polynomial functions, i.e., for semi-algebraic sets, which is not the case of (4.6) due to the $x \neq 0$ term. To circumvent this issue, it is used positive definite polynomials $\varphi_1, \varphi_2 \in \Sigma_n$ that replaces $x \neq 0$ with $\varphi_i(x) \neq 0$. Rearranging the terms and using polynomials $\varphi_i(x)$, problem (4.6) takes the form

$$\begin{aligned}
& \max_{V(x) \in \mathbb{R}[x], V(0)=0} \beta \\
& \text{s.t.} \\
& \{x \in \mathcal{D} \mid -V(x) \geq 0, \varphi_1(x) \neq 0\} = \phi, \\
& \{x \in \mathcal{D} \mid \beta - s(x) \geq 0, V(x) - \gamma \geq 0, V(x) \neq \gamma\} = \phi, \\
& \{x \in \mathcal{D} \mid \gamma - V(x) \geq 0, \dot{V}(x) \geq 0, \varphi_2(x) \neq 0\} = \phi.
\end{aligned} \tag{4.7}$$

Which are in a suitable form to apply the P-satz. Remember that the inequality and inequation conditions become the cone and monoid generated by their arguments, respectively. Therefore, (4.7) is rewritten as

$$\begin{aligned}
& \max_{\substack{V(x) \in \mathbb{R}[x], V(0)=0, \\ k_1, k_2, k_3 \in \mathbb{Z}_+, \\ q_0, \dots, q_9 \in \Sigma_n}} \beta \\
& \text{s.t.} \\
& \underbrace{q_0 - Vq_1}_{\mathcal{C}(-V)} + \underbrace{\varphi_1^{2k_1}}_{\mathcal{M}(\varphi_1)} = 0, \\
& \underbrace{q_2 + (\beta - s)q_3 + (V - \gamma)q_4 + (\beta - s)(V - \gamma)q_5}_{\mathcal{C}(\beta-s, V-\gamma)} + \underbrace{(V - \gamma)^{2k_2}}_{\mathcal{M}(V-\gamma)} = 0, \\
& \underbrace{q_6 + (\gamma - V)q_7 + \dot{V}q_8 + (\gamma - V)\dot{V}q_9}_{\mathcal{C}(\gamma-V, \dot{V})} + \underbrace{\varphi_2^{2k_3}}_{\mathcal{M}(\varphi_2)} = 0,
\end{aligned} \tag{4.8}$$

where the underbraces highlight the cone and monoid terms. These constraints, however, are yet not tractable by SDP. This general form is nonconvex and must be simplified.

Following [Jarvis-Wloszek et al., 2003], polynomials q 's and constants k 's should be

specified appropriately. To begin, the simplest choice of k is to define $k_1 = k_2 = k_3 = 1$. It keeps the problem's overall degree low and considerably facilitates further simplifications. Additionally, the product of SOS polynomials yields an SOS polynomial. This fortunate equivalence allows us to substitute q_0 for $q_0 \varphi_1$ and q_6, \dots, q_8 for $q_6 \varphi_2, \dots, q_8 \varphi_2$.

For the first restriction we take $q_1 = \varphi_1$ and further factor out the φ_1 term. Within the second equation, the concern is due to $(V - \gamma)^2$ term, which is quadratic in the decision variables of V . The exponent can be removed by factoring out $(V - \gamma)$. To do so, we must pick $q_2 = q_3 = 0$. Similarly, third restriction is quadratic due to $V \dot{V}$. Chose $q_9 = 0$ and, by factoring φ_2 out, the three achieved restrictions are

$$\begin{aligned} q_0 - V + \varphi_1 &= 0, \\ q_4 + (\beta - s)q_5 + (V - \gamma) &= 0, \\ q_6 + (\gamma - V)q_7 + \dot{V}q_8 + \varphi_2 &= 0. \end{aligned} \tag{4.9}$$

Note that the identity $V - \varphi_1 = q_0$ is equivalent to $V - \varphi_1 \in \Sigma_n$. That is if we could find any representation of $V - \varphi_1$ such that it can be written as an arbitrary sum-of-squares polynomial (in this case, represented by q_0), then, the first restriction of (4.9) is satisfied. Extending this discussion to second and third conditions, the task of finding the maximum β , originally formulated in (4.6), is written as the following sum-of-squares program

$$\begin{aligned} \max_{\substack{V(x) \in \mathbb{R}[x], \\ q_5, q_7, q_8 \in \Sigma_n.}} & \beta \\ \text{s.t.} & \\ & V - \varphi_1 \in \Sigma_n, \\ & \left((s - \beta)q_5 - (V - \gamma) \right) \in \Sigma_n, \\ & \left((V - \gamma)q_7 - \varphi_2 - \dot{V}q_8 \right) \in \Sigma_n. \end{aligned} \tag{4.10}$$

The optimization problem guarantees that $V(x)$ is positive definite (first restriction) and that $\dot{V}(x)$ is negative definite (third restriction). If a solution exists, the stability properties of Theorem 2 holds, testifying asymptotically stability of the origin of system (4.1).

For concreteness, the above method obtains inner bounds of the region of attraction given by the level sets of functions $V(x)$ and $s(x)$. The most representative RoA estimate we can obtain is the largest level set γ of $V(x)$ which is obtained through the maximization of β such that $\mathcal{S}_\beta \subseteq \Omega_\gamma$ (second restriction of 4.10).

An illustration of the discussed set containment regions is presented in Figure 4.1. By expanding \mathcal{S}_β , we indirectly force Ω_γ to increase as well. Over the iterations, region Ω_γ

can change in shape and pattern. On the other hand, \mathcal{S}_β is defined by the fixed shaping function $s(x)$ and the alignment of this function will dictate the directions in which \mathcal{S}_β will enlarge. A poor choice of $s(x)$ may precociously hit the stability boundary, which makes it more difficult for the algorithm to approximate the RoA with reasonable levels of accuracy, limiting its expansion.

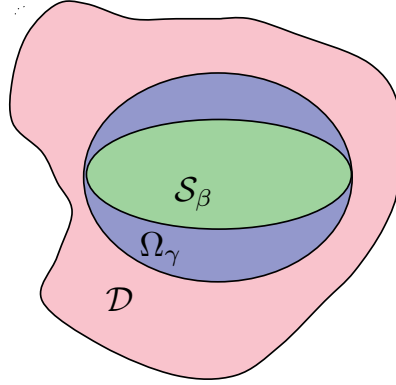


Figure 4.1. Illustration of the containment regions. The pink area stands for the true RoA. The blue area indicates the inner estimate and the green area is the region defined by the shaping function $s(x)$, strictly contained in Ω_γ .

Before solving the optimization problem, one can note that the constraints of problem (4.10) are bilinear in the decision variables due to the products of β q_5 , $(V - \gamma)$ q_7 and \dot{V} q_8 . This issue can be tractable by decomposing the optimization into sub-steps of convex problems with an iterative bounding procedure. It is an application of the block-coordinate descent method [Shen et al., 2017] that relies on fixing some of the decision polynomials and handle restrictions separately through an iterative algorithm. The algorithm is stated as follows.

Algorithm 1 *Iterative bounding procedure*

Let i be the iteration index and begin with $i = 1$. Specify the desired degrees that will be considered for the SOS polynomials: $\deg(V)$, $\deg(q_5)$, $\deg(q_7)$, $\deg(q_8)$, $\deg(\varphi_1)$, and $\deg(\varphi_2)$.

Designate polynomials φ_k to be $\varphi_k = \epsilon_k \sum_{j=1}^n x_j^{\deg(\varphi_k)}$ with $k \in \{1, 2\}$ and for sufficient small $\epsilon_k > 0$. Pick an arbitrary SOS polynomial to be the shaping function s and, starting from an initial Lyapunov function candidate $V^{(i=0)} = V_0$, proceed to Gamma step.

(i) **Gamma step**

Set $V = V^{(i-1)}$ and solve the linesearch on γ :

$$\begin{aligned} & \max_{q_7, q_8 \in \Sigma_n.} \gamma \\ & \text{s.t.} \\ & \left((V - \gamma)q_7 - \varphi_2 - \dot{V}q_8 \right) \in \Sigma_n. \end{aligned} \tag{4.11}$$

Set $\gamma^{(i)} = \gamma$, $q_7^{(i)} = q_7$, $q_8^{(i)} = q_8$ and proceed to Beta-step.

(ii) **Beta step**

Set $V = V^{(i-1)}$, $\gamma = \gamma^{(i-1)}$ and solve the linesearch on β :

$$\begin{aligned} & \max_{q_5 \in \Sigma_n.} \beta \\ & \text{s.t.} \\ & \left((s - \beta)q_5 - (V - \gamma) \right) \in \Sigma_n. \end{aligned} \tag{4.12}$$

Set $\beta^{(i)} = \beta$, $q_5^{(i)} = q_5$ and continue to Lyapunov function step.

(iii) **Lyapunov function step**

Set $\gamma = \gamma^{(i)}$, $\beta = \beta^{(i)}$, $q_5 = q_5^{(i)}$, $q_7 = q_7^{(i)}$ and $q_8 = q_8^{(i)}$ and solve problem (4.10) to find V . Set $V^{(i)} = V$ and check if β no longer improves, i.e., if $\beta^{(i)} - \beta^{(i-1)} \leq$ tolerance, conclude the iterations, otherwise increment i and return to γ -Step.

Remarks and Properties of Algorithm 1

A question that the reader may pose at this point, is the real need of the region \mathcal{S}_β since without the set containment $\mathcal{S}_\beta \subseteq \Omega_\gamma$ we could still be searching for a $V(x)$ while maximizing γ subject to the Lyapunov conditions. However, in this case, seeking to find the largest domain $\Omega_\gamma = \{x \in \mathcal{D} \mid V(x) \leq \gamma\}$ would be translated to a problem that, starting from a feasible point, scales $V(x)$ to increase γ such that the stability criterion holds. Increasing γ would not necessarily lead to an expansion of the RoA, but rather a rate tradeoff between γ and V .

For this reason, the variable sized region \mathcal{S}_β , defined by the fixed-function $s(x)$, is included. Maximizing β , on the other hand, indeed increase region $s(x) < \beta$ and, since it is contained in Ω_γ , forces $V(x) \leq \gamma$ to increase as well, not simply scaling itself.

Algorithm 1 also requires an initial Lyapunov function $V_0(x)$. The preferred and simplest choice is the quadratic Lyapunov function $V_0 = x^T P x$ derived from the linearized

system. This does not preclude the choice of any other candidate function.

Additionally, for polynomials $p_0, p_1 \in \Sigma_n$, in order to satisfy $p_0 - p_1 \geq 0$, the degree of p_0 must be equal or higher the degree of p_1 . From Program (4.10), the following degree bounds are recognized

$$\begin{aligned} \deg(V) &\geq \deg(\varphi_1), \\ \deg(q_5) + \deg(s) &\geq \deg(V), \\ \deg(q_7) &\geq \deg(f) + \deg(q_8) - 1, \\ \deg(V) + \deg(q_7) &\geq \deg(\varphi_2). \end{aligned} \tag{4.13}$$

Finally, for polynomials φ_k defined as

$$\varphi_k = \epsilon_k \sum_{j=1}^n x_j^{\deg(\varphi_k)}, \quad k \in \{1, 2\}, \tag{4.14}$$

it is desirable small values for coefficients ϵ_k . Otherwise, the program will be excessively conservative to impose positive and negative definiteness constraints over V and \dot{V} , respectively.

4.3.1 Numerical example

The discussion made above is verified through an academic example. Given the third order polynomial system

$$\begin{aligned} \dot{x}_1 &= x_2, \\ \dot{x}_2 &= -(1 - x_1^2)x_1 - x_2, \end{aligned} \tag{4.15}$$

we desire to estimate its RoA.

For the sake of this example, let us search for a second order Lyapunov function. From (4.13) and choosing the smallest degrees combination, we pick $\deg(q_8)=0$ and $\deg(q_5)=\deg(q_7)=2$. Polynomials φ_1 and φ_2 are chosen to be $10^{-6}x^T x$. Moreover, Algorithm 1 is solved considering two orthogonally arranged shaping functions

$$\begin{aligned} s_1(x) &= 1.34x_1^2 + 1.22x_1x_2 + 0.74x_2^2, \\ s_2(x) &= 1.34x_1^2 - 1.22x_1x_2 + 0.74x_2^2. \end{aligned} \tag{4.16}$$

The quadratic Lyapunov function candidate $V_0 = x^T P x$ is derived from the linearization of (4.15).

The results are shown in Figure 4.2. The system has one equilibrium point at the origin and the thin blue and orange lines are the systems stable and unstable trajectories, respectively. One can note $s_1(x)$ was chosen to have level sets that more closely align with the actual region of attraction, the opposite is verified for $s_2(x)$.

By choosing $s_1(x)$ as the shape function, the algorithm took 14 iterations to reach the stop criterion. On the other hand, by taking $s_2(x)$, four iterations were sufficient to \mathcal{S}_β reach the boundary. With this deliberately poor choice, the algorithm tries to expand the region over areas where the level sets cannot follow, limiting its enlargement.

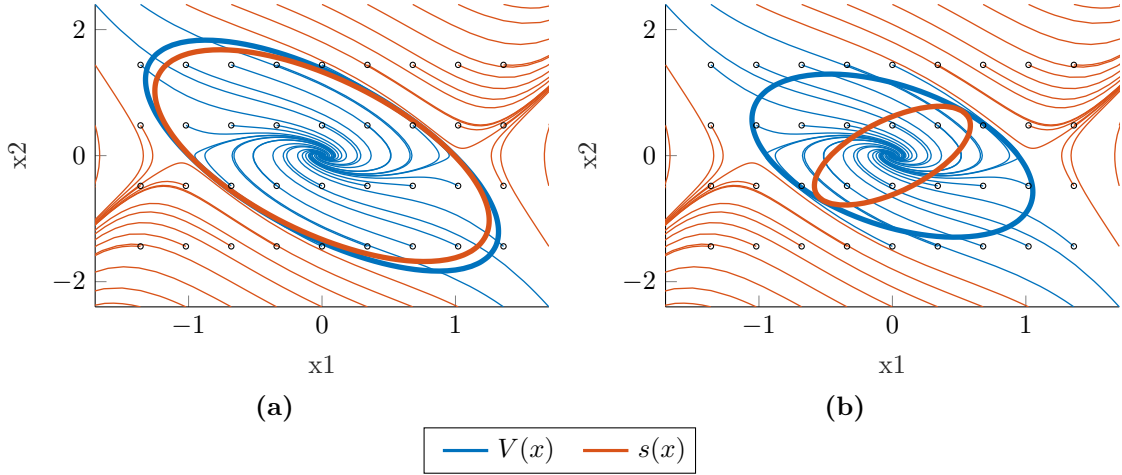


Figure 4.2. Phase portrait is shown in the background with initial conditions denoted by black dots. The estimated regions Ω_γ and \mathcal{S}_β are shown by the ellipses. The regions are obtained by picking (a) $s_1(x)$ and (b) $s_2(x)$.

4.4 Expanding the RoA with State Feedback

Now that we are able to estimate the region of attraction of a polynomial system, we move forward to the problem of designing controllers for enlarging the RoA.

Consider the system

$$\dot{x} = f(x) + g(x)u \quad (4.17)$$

where $x \in \mathbb{R}^n$ is the state variables, $u \in \mathbb{R}^m$ is the control input vector, $f : \mathcal{D} \rightarrow \mathbb{R}^n$ is a vector of polynomial state functions, $g : \mathcal{D} \rightarrow \mathbb{R}^{n \times m}$ is a matrix of polynomial control functions affine in u , with $\mathcal{D} \subset \mathbb{R}^n$. Without loss of generality, it is assumed that the equilibrium point of interest $\bar{x} \in \mathcal{D}$ is at the origin of \mathbb{R}^n .

Allowing input u to be generated by a polynomial $K(x)$, i.e., $u = K(x)$ with $K(x) \in \mathbb{R}[x]$ and $K(0) = 0$, the system (4.17) becomes

$$\dot{x} = f(x) + g(x)K(x) \quad (4.18)$$

and the optimization (4.10) can be extended to a problem that, besides $V(x)$, searches for some as of yet unknown $K(x)$ candidate.

4.4.1 Expanding interior state feedback design

The state feedback controller design works in similar form of Program (4.10) and Algorithm 1. We follow the steps of the *expanding interior algorithm* development, presented in Section 4.3.

Again we restrict our search over polynomials and describe the invariant semi-algebraic sets as

$$\begin{aligned}\mathcal{S}_\beta &= \{x \in \mathcal{D} \mid s(x) \leq \beta\}, \\ \Omega_\gamma &= \{x \in \mathcal{D} \mid V(x) \leq \gamma\}.\end{aligned}\tag{4.19}$$

such that $\mathcal{S}_\beta \subseteq \Omega_\gamma$. From the Lyapunov theorem and considering the closed-loop system (4.18), we now must satisfy

$$\{x \in \mathcal{D} \mid V(x) \leq \gamma\} \subseteq \{x \in \mathcal{D} \mid \frac{\partial V(x)}{\partial x}(f(x) + g(x)K(x)) < 0\}.\tag{4.20}$$

Similarly, if we can find V and K that satisfy the stability statements, then (4.18) is asymptotically stable. Moreover, the largest RoA we can show that converges to the origin is the level set γ of $V(x)$ contained in \mathcal{D} .

Reformulating these semi-algebraic sets into a problem of testing emptiness, invoking P-satz, and by making similar considerations discussed in the previous section, we find the following SOS program

$$\begin{aligned}& \max_{\substack{V(x) \in \mathbb{R}[x], \\ K(x) \in \mathbb{R}[x], \\ q_5, q_7, q_8 \in \Sigma_n.}} \beta \\ & \text{s.t.} \\ & V - \varphi_1 \in \Sigma_n, \\ & \left((s - \beta)q_5 - (V - \gamma) \right) \in \Sigma_n, \\ & \left((V - \gamma)q_7 - \varphi_2 - \frac{\partial V}{\partial x}(f + gK)q_8 \right) \in \Sigma_n.\end{aligned}\tag{4.21}$$

The optimization problem guarantees that $V(x)$ is positive definite and $\dot{V}(x)$ is negative definite over the closed-loop system. We can now state the algorithm to design a controller to enlarge the RoA estimate.

Once more, the constraints are bilinear in the decision variables. The workaround for this issue is to break (4.21) into sub-steps of convex problems. Although similar to Algorithm 1, we must include one new step that is responsible for designing the control law $K(x)$. The algorithm is detailed as follows.

Algorithm 2 Iterative bounding procedure - state feedback

Let i be the iteration index and begin with $i = 1$. Specify the desired degrees that will be considered for the SOS polynomials: $\deg(V)$, $\deg(K)$, $\deg(q_5)$, $\deg(q_7)$, $\deg(q_8)$, $\deg(\varphi_1)$, and $\deg(\varphi_2)$.

Designate polynomials φ_k to be $\varphi_k = \epsilon_k \sum_{j=1}^n x_i^{d_{\varphi_k}}$ with $k \in \{1, 2\}$ and for sufficient small $\epsilon_k > 0$. Pick an arbitrary positive polynomial to be the shaping function s and, starting from an initial Lyapunov function candidate $V^{(i=0)} = V_0$ and SOS polynomial $q_8^{(i=0)} = 1$, proceed to Control design step.

(i) Control design step

Set $V = V^{(i-1)}$, $q_8 = q_8^{(i-1)}$ and solve the linesearch on γ to obtain K :

$$\begin{aligned} & \max_{q_7, q_8 \in \Sigma_n} \gamma \\ & \text{s.t.} \\ & \left((V - \gamma)q_7 - \varphi_2 - \frac{\partial V}{\partial x}(f + gK)q_8 \right) \in \Sigma_n. \end{aligned} \quad (4.22)$$

Set $K^{(i)} = K$ and proceed to Gamma step.

(ii) Gamma step

Set $V = V^{(i-1)}$, $K = K^{(i-1)}$ and solve the linesearch on γ :

$$\begin{aligned} & \max_{q_7, q_8 \in \Sigma_n} \gamma \\ & \text{s.t.} \\ & \left((V - \gamma)q_7 - \varphi_2 - \frac{\partial V}{\partial x}(f + gK)q_8 \right) \in \Sigma_n. \end{aligned} \quad (4.23)$$

Set $\gamma^{(i)} = \gamma$, $q_7^{(i)} = q_7$, $q_8^{(i)} = q_8$ and proceed to Beta step.

(iii) Beta step

Set $V = V^{(i-1)}$, $\gamma = \gamma^{(i-1)}$ and solve the linesearch on β :

$$\begin{aligned} & \max_{q_5 \in \Sigma_n} \beta \\ & \text{s.t.} \\ & \left((s - \beta)q_5 - (V - \gamma) \right) \in \Sigma_n. \end{aligned} \quad (4.24)$$

Set $\beta^{(i)} = \beta$, $q_5^{(i)} = q_5$ and continue to the Lyapunov function step.

(iv) **Lyapunov function step**

Set $K = K^{(i)}$, $\gamma = \gamma^{(i)}$, $\beta = \beta^{(i)}$, $q_5 = q_5^{(i)}$, $q_7 = q_7^{(i)}$ and $q_8 = q_8^{(i)}$ and search for a V such that (4.21) holds. Set $V^{(i)} = V$ and check if β no longer improves, i.e., if $\beta^{(i)} - \beta^{(i-1)} \leq \text{tolerance}$, conclude the iterations, otherwise increment i and return to Control design step.

Remarks and Properties of Algorithm 2

To ensure that Algorithm 2 starts from a feasible point, the linearization of the system must be controllable. Since we begin with the quadratic Lyapunov function $V_0(x)$ derived from the same linearization, then the *control design step* will stabilize the nonlinear system near to the origin.

Note that, unlike function V , K does not have non-negativity constraints. We only need to ensure that $K(0) = 0$, therefore, K must have no constant terms. Additionally, it is possible to search for polynomial control laws of arbitrary degree.

Concerning to positivity and feasibility of Program (4.21), the degrees restrictions that polynomials V , K , q 's and φ 's must hold are

$$\begin{aligned} \deg(V) &\geq \deg(\varphi_1), \\ \deg(q_5) + \deg(s) &\geq \deg(V), \\ \deg(q_7) &\geq \max(\deg(f), \deg(gK)) + \deg(q_8) - 1, \\ \deg(V) + \deg(q_7) &\geq \deg(\varphi_2). \end{aligned} \tag{4.25}$$

4.4.2 Input saturation

Expanding the region of attraction with state feedback is a problem that resumes synthesizing a state feedback controller $u = K(x)$ with $K(x) \in \mathbb{R}[x]$. This control law is responsible for enlarging the invariant set Ω_γ such that the origin is an asymptotically stable equilibrium point of the closed-loop system.

If we decide to project a state feedback control law for systems where the actuator saturations are known, then it is desirable to include upper and lower bounds restrictions in the control design process. Otherwise, we would be generating stability certificates over areas where the trajectories of the system could not flow due to limitations on the actuator.

Therefore, one wishes to design state feedback controller such that $u_{lb} \leq K(x) \leq u_{ub}$

holds. By taking into account these restrictions, the two set containments are obtained

$$\begin{aligned} \{x \in \mathcal{D} \mid V(x) \leq \gamma\} &\subseteq \{x \in \mathcal{D} \mid K(x) \leq u_{ub}\}, \\ \{x \in \mathcal{D} \mid V(x) \leq \gamma\} &\subseteq \{x \in \mathcal{D} \mid K(x) \geq u_{lb}\}. \end{aligned} \quad (4.26)$$

Rewriting these semi-algebraic sets into a problem of testing emptiness, we have

$$\begin{aligned} \{x \in \mathcal{D} \mid V(x) \leq \gamma, K(x) \geq u_{ub}, K(x) \neq u_{ub}\} &= \phi, \\ \{x \in \mathcal{D} \mid V(x) \leq \gamma, K(x) \leq u_{lb}, K(x) \neq u_{lb}\} &= \phi. \end{aligned} \quad (4.27)$$

By invoking P-satz, the restrictions become

$$\begin{aligned} \underbrace{q_{10} + (\gamma - V)q_{11} + (K - u_{ub})q_{12} + (\gamma - V)(K - u_{ub})q_{13}}_{\mathcal{C}(\gamma-V, K-u_{ub})} + \underbrace{(K - u_{ub})^{2k_4}}_{\mathcal{M}(K-u_{ub})} &= 0, \\ \underbrace{q_{14} + (\gamma - V)q_{15} + (-K + u_{lb})q_{16} + (\gamma - V)(-K + u_{lb})q_{17}}_{\mathcal{C}(\gamma-V, -K+u_{lb})} + \underbrace{(K - u_{lb})^{2k_5}}_{\mathcal{M}(K-u_{lb})} &= 0. \end{aligned} \quad (4.28)$$

Choosing $k_4 = k_5 = 1$, $q_{10} = q_{11} = q_{14} = q_{15} = 0$, and factoring out the $(\pm K \mp u_{\{ub, lb\}})$ terms, we obtain the SOS restrictions

$$\begin{aligned} ((u_{ub} - K) + (V - \gamma)q_{13}) &\in \Sigma_n, \\ ((K - u_{lb}) + (V - \gamma)q_{17}) &\in \Sigma_n, \\ q_{13}, q_{17} &\in \Sigma_n. \end{aligned} \quad (4.29)$$

which now can be included in Program (4.21). More specifically, it must be incorporated in Algorithm 2 through the *control design* (i), *gamma* (ii) and *Lyapunov function* (iv) steps.

By the same reasons discussed earlier, when it comes to the polynomial degrees choices, we must be careful to ensure

$$\begin{aligned} \deg(V) + \deg(q_{13}) &\geq \deg(K), \\ \deg(V) + \deg(q_{17}) &\geq \deg(K). \end{aligned}$$

4.5 Non-Affine in Control Nonlinear Systems

The state feedback control synthesis given above assumes that the control signals enter affinely in the closed-loop state-space equations, while in practice this may not be the case.

The control problem for general non-affine nonlinear systems inspired researchers for

decades. One main challenge lies in obtaining the inverse of the nonlinear function to employ feedback equivalence. For example, to stabilize $\dot{x} = x - u^2$ one can choose $u = \sqrt{(a+1)x}$, but soon encounter imaginary values whenever $x < 0$. Multiple solutions, some of which are not feasible in a physical plant, are the additional difficulties of such systems [Narang, 2012]. In order to consider non-affine in control systems for use in the SOS theory, we consider numerical approximations that provide constructive forms for the control variable.

The simplest approach that approximates $\dot{x} = f(x, u)$ to an affine in control system is to evaluate a linearization around a steady input \bar{u} . To this approach, we refer “input linearization” (IL). Correspondingly, we can also linearize the closed-loop system under the coefficients of a steady control law $\bar{K}(x)$. To this approach, we refer “control linearization” (CL). Although sounding similar, these methodologies differ in their characteristics. The following discussion shows how we achieve these linearizations and their main aspects.

4.5.1 Input linearization (IL)

Given the nonlinear system

$$\dot{x} = f(x) + g(x, u), \quad (4.30)$$

we wish to linearize g over a steady input \bar{u} . The linear behavior of the control actuation around \bar{u} is achieved by its first-order approximation

$$g(x, u) \approx g(x, \bar{u}) + \left. \frac{\partial g(x, u)}{\partial u} \right|_{u=\bar{u}} (u - \bar{u}). \quad (4.31)$$

Hence, substituting (4.31) into (4.30) we have

$$\dot{x} \approx \underbrace{f(x) + g(x, \bar{u}) - \left. \frac{\partial g(x, u)}{\partial u} \right|_{u=\bar{u}} \bar{u}}_{\bar{f}_{IL}(x)} + \underbrace{\left. \frac{\partial g(x, u)}{\partial u} \right|_{u=\bar{u}}}_{\bar{g}_{IL}(x)} u, \quad (4.32)$$

expressed in the general affine input form as

$$\dot{x} \approx \bar{f}_{IL}(x) + \bar{g}_{IL}(x)u. \quad (4.33)$$

The main shortcoming associated with this linearization is well-known: the validity of this approach is restricted to a narrow region around the operating input \bar{u} . The resulting $\bar{g}_{IL}(x)u$ term does not consider any information about the control law structure, but rather the constant steady input. Since we know that $K(x)$ is a polynomial function by design and also computed iteratively, we can expand the idea by linearizing the closed-

loop system over the control gain coefficients.

4.5.2 Control linearization (CL)

Given a polynomial control law function $\bar{K}(x)$, the first order approximation of the closed-loop control vector function over the coefficients of $K(x)$ is

$$g(x, K(x)) \approx g(x, \bar{K}(x)) + \left. \frac{\partial g(x, u)}{\partial u} \right|_{u=\bar{K}(x)} (K(x) - \bar{K}(x)). \quad (4.34)$$

Substituting (4.34) into (4.30), we have

$$\dot{x} \approx \underbrace{f(x) + g(x, \bar{K}(x)) - \left. \frac{\partial g(x, u)}{\partial u} \right|_{u=\bar{K}(x)} \bar{K}(x)}_{\bar{f}_{CL}(x)} + \underbrace{\left. \frac{\partial g(x, u)}{\partial u} \right|_{u=\bar{K}(x)} K(x)}_{\bar{g}_{CL}(x)}, \quad (4.35)$$

that is rewritten in the general input-affine form

$$\dot{x} \approx \bar{f}_{CL}(x) + \bar{g}_{CL}(x)u, \quad (4.36)$$

with $u = K(x)$. Note that the chain partial derivative $\frac{\partial g(x, u)}{\partial u}$ in (4.35) is evaluated at $\bar{K}(x)$. We are analyzing the systems' closed-loop behavior along its trajectories. For instance, if the nonlinear system is already an input affine system, then (4.36) falls on a particular case of (4.33). To highlight the differences between both linearizations, we show a discussion under an example.

4.5.3 Illustrative example

Given a two dimensional non affine in control system

$$\dot{x} = f(x) + u^2, \quad (4.37)$$

with $x = [x_1 \ x_2]^T$. The problem of synthesizing an SOS first order state feedback control law $u = K(x)$, i.e., $K(x) = k_1x_1 + k_2x_2$, is summarized in finding coefficients k_i , $i \in \{1, 2\}$, such that (4.22) holds. For simplicity, a first-order polynomial $K(x)$ was selected, however, without loss of generality, it can be extended to a polynomial of arbitrary degree.

The closed loop system (4.37) would take the form

$$\dot{x} = f(x) + (k_1x_1 + k_2x_2)^2,$$

which, for the control synthesis problem, is nonlinear in the decision variables k_i . Following the input linearization, the behavior of (4.37) around \bar{u} is

$$\dot{x} \approx \underbrace{f(x) + \bar{u}^2 - 2\bar{u}}_{\bar{f}_{IL}(x)} + \underbrace{2\bar{u}}_{\bar{g}_{IL}(x)} u, \quad (4.38)$$

which is now affine in control and searching for arguments k_i of the control law $u = K(x) = k_1x_1 + k_2x_2$ is now a convex problem. The main remark about IL is that, by using system (4.38), any estimated region of attraction may degrade when the level sets of $K(x)$ deviate from \bar{u} . We are assuming the linearization is valid through the entire estimated RoA, not only near the neighborhood of \bar{u} .

On the other hand, manipulating (4.37) around a steady control law $\bar{K}(x) = \bar{k}_1x_1 + \bar{k}_2x_2$ and following the CL approach, we have

$$\dot{x} \approx \bar{f}_{CL}(x) + \underbrace{2(\bar{k}_1x_1 + \bar{k}_2x_2)}_{\bar{g}_{CL}(x)}(x_1k_1 + x_2k_2), \quad (4.39)$$

where $\bar{f}_{CL}(x)$ is the input-independent term.

Now, the system is linearized around the stable system, that is, around the trajectories within the domain stabilized by the control law $\bar{K}(x)$, in contrast with the former, linearized specifically around the point \bar{u} .

This characteristic can be explicitly seen by inspecting the control vector functions $\bar{g}_{IL}(x)$ and $\bar{g}_{CL}(x)$. The first becomes a constant, while the second is a function of x with behavior defined by constants \bar{k}_i .

An interesting characteristic about CL is that it allows us to synthesize a new control law while enforcing small variations for the coefficients of $\bar{K}(x)$. This is an attempt to keep the linearization reliable since the closed-loop system will be near the system to which it was approximated. It is achieved by considering conditions

$$\begin{aligned} \zeta_i - (k_i - \bar{k}_i) &\geq 0, \\ \zeta_i + (k_i - \bar{k}_i) &\geq 0, \end{aligned} \quad (4.40)$$

where ζ_i are positive values. These restrictions ensure $|k_i - \bar{k}_i| \leq \zeta_i$ and, with sufficient small ζ_i , the distortions due linearization should be mitigated.

For each iteration of Algorithm 2, we search for $K(x)$ in which coefficients are near $\bar{K}(x)$. With this iterative approach, the region of attraction is expanded by synthesizing a new control law that moves small steps towards the optimum controller. Additionally, each suboptimal $K(x)$ obtained from iteration t is used as the steady $\bar{K}(x)$ of iteration $t + 1$. Obviously, the algorithm requires an initial candidate $\bar{K}_0(x)$. To illustrate the

current discussion, we present a theoretical application example.

4.6 Theoretical Example

Numerical example. Let us consider a two dimensional fifth order nonlinear ODE

$$\begin{aligned}\dot{x}_1 &= -2x_1 + x_2 + x_1^3 + x_2^5 - u^3, \\ \dot{x}_2 &= -x_1 - x_2 + x_1^2 x_2^5 + u/4,\end{aligned}\tag{4.41}$$

where $|u| \leq 5$. The equilibrium point is at the origin and eigenvalues of the open-loop linearized system are $-1.5 \pm 0.866i$, therefore, (4.41) is locally stable.

Following the degrees bounds recognized in (4.25), we choose

$$\begin{aligned}\deg(\varphi_1) &= \deg(V), \\ \deg(q_5) &= \max\{\deg(V) - \deg(s), 2\}, \\ \deg(q_8) &= 2, \\ \deg(q_7) &= \deg(g) + \deg(q_7) + \deg(K) - 1, \\ \deg(\varphi_2) &= \deg(q_8), \\ \deg(q_{13}) &= \deg(q_{17}) = 2.\end{aligned}\tag{4.42}$$

To enhance the estimation, we search for V of degrees 2, 4, 6, and 8. As discussed in [Masouleh and Limebeer, 2017], searching for higher-order functions can improve our representation of the RoA. Moreover, we set $s(x) = x^T x$ and constants ϵ_1 and ϵ_2 are chosen to be 10^{-6} and 10^{-8} , respectively.

4.6.1 Estimating the RoA

We now solve Algorithm 1 with the objective to estimate the RoA for an open-loop scenario, i.e., with $u = 0$. The result is shown in Figure 4.3. Phase plane is shown in the background with trajectories starting from black dots and the estimated RoAs are shown as a sub-level set of Lyapunov functions with degrees varying from 2 up to 8.

By construction, higher-order polynomials contain the lower ones. Therefore, increasing the Lyapunov function order should lead to a more representative estimation of the true RoA. Quantitatively, these improvements can be measured by the RoAs surfaces area. The computed areas are 5.81, 6.48, 6.97, and 7.05 achieved with functions of order 2, 4, 6, and 8, respectively. This motivates the use of high order functions to improve the estimation.

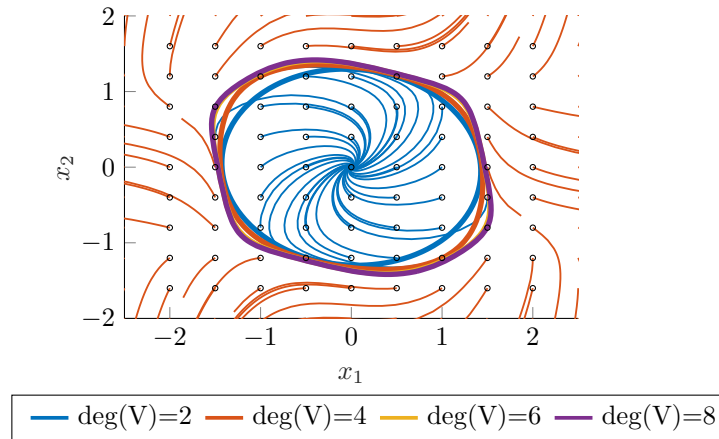


Figure 4.3. In the background is shown the phase portrait of the open-loop response with initial conditions denoted by black dots. The estimated RoAs for Lyapunov Functions of degrees 2, 4, 6, and 8.

4.6.2 Expanding the RoA

We can now look to find state feedback controllers that expand the RoA. Since system (4.15) is non-affine in control, a numerical approximation must be evaluated. We follow the steps proposed in Section 4.6 and evaluate the IL and CL approaches. The linearizations are performed around $\bar{u} = 0$ and $\bar{K}_0(x) = 0.39x_1 - 2.54x_2$, which is an LQR gain computed using the classical Ricatti equation [Chen, 1998]. We choose $Q = \text{diag}(1.5, 3)$ and $R = 0.1$, where Q and R are with SI units. The input saturation is included ($|u| = |K(x)| \leq 5$), ζ_i is specified as 0.25, and we search for a first order polynomial control law.

Note that, performing the IL method, the linearization will result in the static control input vector $g_{IL}(x) = [0 \ 1/4]^T$. It does not incorporate any information about the x_1 dynamics. On the other hand, by evaluating the CL approximation, the algorithm begins with $g_{CL}(x) = [-3\bar{K}_0^2 \ 1/4]^T$. One should note that g_{CL} is changed iteratively as new values of \bar{K} are obtained.

The estimated RoAs are presented in Figure 4.4, where the phase plane of the open-loop system is shown in the background. With the IL method, the controller mainly expands the RoA towards x_2 direction, whereas the CL approach combines information of both axis and the estimated RoA is efficiently enlarged.

Table 4.1 shows the RoAs estimated area. In agreement with Figure 4.4, the regions computed through the CL approximation are considerably larger if compared to the results achieved using the IL. Also, as discussed earlier, we obtain a more representative estimation of the actual RoA as we increase the Lyapunov function order.

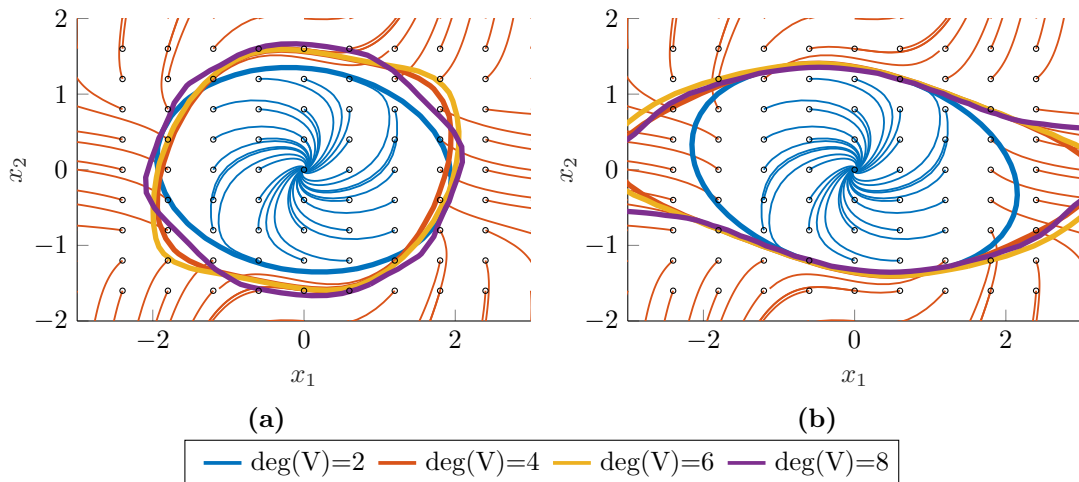


Figure 4.4. The estimated RoAs of the closed-loop system are demonstrated using Lyapunov functions of orders 2, 4, 6 and 8, computed evaluating (a) IL and (b) CL linearizations, respectively.

Table 4.1. RoA's estimated area under a state feedback controller for different degrees of V .

Method	deg(V)			
	2	4	6	8
IL	8.2472	9.8072	10.3758	10.6230
CL	9.1516	12.1425	12.9978	13.7323

4.7 Final Remarks

In this chapter, we presented the state feedback control synthesis problem using SOS relaxations introduced in [Jarvis-Wloszek et al., 2003, Jarvis-Wloszek et al., 2005] and developed a method to design polynomial controllers for a class of non-affine nonlinear systems. The main idea behind this approach is to use first-order approximations that provide constructive forms for the control variable. We have seen how the synthesis and stability analysis problems can be solved algorithmically.

The following publication was produced presenting the results of this chapter (Ribeiro, Fioravanti, Moutinho & de Paiva 2020a):

- A. M. Ribeiro, A. R. Fioravanti, A. Moutinho and E. C. de Paiva. Control Design Based on Sum-of-Squares Programming for Non-affine in Input Systems. In *IEEE 6th International Conference on Control Science and Systems Engineering (ICC-SSE)*, Beijing, China, July 17-19, 2020.
<https://doi.org/10.1109/ICCSSE50399.2020.9171951>

5 RoA Estimation and State Feedback

5.1 Introduction

In this chapter, we will investigate how the analysis questions for the vehicle nonlinear system described by ordinary differential equations can be answered using sums-of-squares (SOS) relaxations. Our immediate goal is to attain vehicle stability analysis and controller synthesis while accounting for input saturation using SOS programming.

To begin, one should recall that the SOS theory can only be applied to systems described by polynomial functions. Therefore, to assemble the vehicle lateral dynamics, we must guarantee that all functions involved are polynomials in their arguments. Unfortunately, none of the tire models (2.9)-(2.10) fall in this class of functions. The solution that overcomes this issue is to replace the non-polynomial functions with polynomial models that reasonably approximates the desired system behavior. In the forthcoming sections, compositions of polynomial and rational polynomial functions are explored as reasonable approximations for evaluation of the SOS programming.

5.2 Polynomial Approximation

The first and simplest function that can replace the nonlinear tire models is

$$F_{yi}(\alpha_i) = \sum_{j=0}^q p_{ij} \alpha_i^j = p_{i0} + p_{i1} \alpha_i + p_{i2} \alpha_i^2 + \cdots + p_{iq} \alpha_i^q \quad (5.1)$$

where q is the polynomial order, p_{ij} are the polynomial coefficients and α_i are the tire slip angles:

$$\alpha_f = \frac{v + ar}{u_0} - \delta, \quad \alpha_r = \frac{v - br}{u_0}. \quad (5.2)$$

Given the data points computed from the nonlinear tire function, the coefficients p_{ij} are found using the least-squares algorithm in order to produce the best fit. Although polynomial models have a simple form, the fitting is inevitably sensitive to data.

As shown in Figure 5.1, the fitting error decreases as the polynomial order increases. We cannot, nonetheless, overly increase the polynomial degree to reduce the errors since

it potentially leads to unstable models or requires a prohibitive computational effort, restricting their use with SOS decompositions.

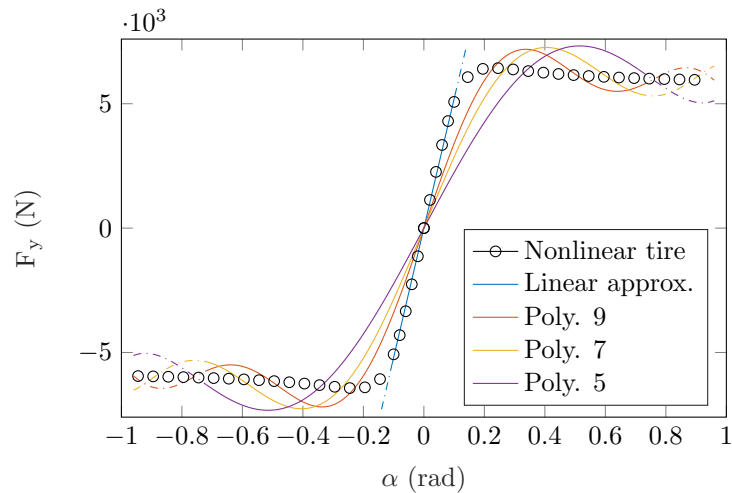


Figure 5.1. Tire forces approximation. The Pacejka data points are shown as black circles along with 5th, 7th, and 9th order polynomial fits.

Furthermore, observe that α_i are written in terms of states x and input δ . As a consequence, approximation (5.1) necessarily contains elements with exponents of order q and terms with arguments $\delta, \delta^2 \dots \delta^q$ will appear. This makes the polynomial model non-affine in the input δ .

5.2.1 Region of attraction estimation

We will now focus our attention on estimating the RoA around the stable equilibrium point. The system is assembled using a 7th order polynomial tire model (5.1), which is substituted into (2.8) and (2.5). This results in two polynomial ODEs that describe the lateral dynamics with states $x = [v, r]^T$ and input $u = [\delta, M_z]$.

All the necessary model structural parameters are default vehicle parameters available in the literature [Cordeiro, 2017]. In the following and forthcoming results, the corresponding parameters listed in Table 5.1 are used.

The stability analysis is performed using the iterative bounding procedure described in Algorithm 1. This algorithm requires an initial Lyapunov function candidate at the first iteration. Following the suggestion made in the majority of works focused on estimating the RoA using SOS constraints, an easy and good choice is the quadratic Lyapunov function $V_{lin} = x^T P x$ derived from the linearized vehicle model associated with the Lyapunov equation [Tamba and Nazaruddin, 2018, Iannelli et al., 2019a].

Based on the author's experience, the solution to an SOS optimization problem can have several numerical difficulties. To avoid these potential adversities, the degrees of polynomials q_5 , q_7 , and q_8 , are chosen to be as small as possible, such that the degrees

Table 5.1. Vehicle and tire model main physical parameters.

Symbol	Parameter name	Value	Unit
m	Vehicle mass	1500	kg
I_z	Yaw inertia	1350	$\frac{kg}{m^2}$
a	Distance from CG to front wheels	1.5	m
b	Distance from CG to rear wheels	2	m
c	Half of wheelbase distance	0.9	m
r_w	Wheel radius	0.25	m
C_α	Tire cornering stiffness	55	kN
C_σ	Tire longitudinal stiffness	120	kN
δ_{max}	Steering saturation	20	deg
$M_{z_{max}}$	Differential moment saturation	1200	N

bounds (4.25) are recognized, therefore, we pick

$$\begin{aligned}
 \deg(\varphi_1) &= \deg(V), \\
 \deg(q_5) &= \max\{\deg(V) - \deg(s), 2\}, \\
 \deg(q_8) &= 2, \\
 \deg(q_7) &= \deg(f) + \deg(q_8) - 1, \\
 \deg(\varphi_2) &= \deg(q_7).
 \end{aligned}$$

Polynomials φ_k are defined with constants ϵ_k of magnitudes 10^{-6} and the Lyapunov function degree is selected to vary from 2 to 8. Now, remains the choice of shaping function $s(x)$. This function gives dimensional scaling and reflects the influence of certain directions in the state space. As its name suggests, the importance relies on the fact that $s(x)$ provides the shape and patterns of the regions over which we will be verifying the Lyapunov conditions. To understand these characteristics, we evaluate Algorithm 1 for two intuitive positive functions: $s(x) = x^T x$ and $s(x) = V_{lin}$.

Straight Running Maneuver

As a first application, we estimate the region of attraction for a straight running maneuver. Steering angle δ is set to 0 degree with constant longitudinal speed $u_0 = 10 \text{ m/s}$. RoA estimates for different Lyapunov function degrees are shown in Figure 5.2. Phase portrait is shown in the background along with the equilibrium points, denoted by black dots.

The conservativeness of the results in Figure 5.2a is attributed to the shaping function.

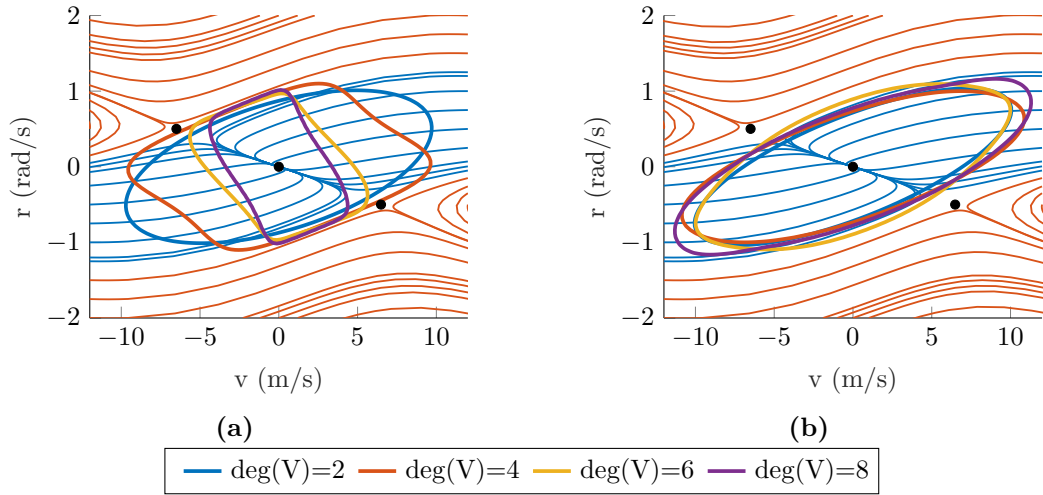


Figure 5.2. In background we present phase plane for the vehicle model assemble with polynomial approximation for the straight running maneuver. RoA estimates are shown using (a) $s(x) = x^T x$ and (b) $s(x) = V_{lin}$.

In this case, the RoA estimates are not enlarging in all directions. On the other hand, when using $s(x) = V_{lin}$, we are providing a function locally aligned with the RoA and thus might be used to obtain a better estimate, as depicted in Figure 5.2b.

Cornering maneuver

As a second verification, we consider a constant cornering maneuver. The steering angle is set to 5 degrees with constant longitudinal velocity $u_0 = 10 \text{ m/s}$. As shown in Figure 5.3, the phase plane is no longer symmetric and the equilibrium point x_{eq} is not at the origin. The system must be shifted to the origin via a change of variables. Given the nonzero equilibrium point $x_{eq} \neq 0$ and considering $\bar{x} = x - x_{eq}$, the derivative of \bar{x} is

$$\dot{\bar{x}} = \dot{x} = f(x) + g(x)u = f(\bar{x} + x_{eq}) + g(\bar{x} + x_{eq})u, \quad (5.3)$$

which can now be used to formulate the SOS problem.

The non-symmetry of the system trajectories makes it more difficult for the algorithm to approximate the RoA with the prior levels of accuracy. This is due to $s(x)$ hitting the stability boundary close to the equilibrium, thereby inhibiting the enlargement of the estimated RoA.

This characteristic can be graphically seen by plotting the shaping function level sets. From Figure 5.4, we can see clearly that region \mathcal{S}_β (red) is contained in region Ω_γ (blue), imposed by the set containment

$$\{x \in \mathcal{D} \mid s(x) \leq \beta\} \subseteq \{x \in \mathcal{D} \mid V(x) \leq \gamma\}.$$

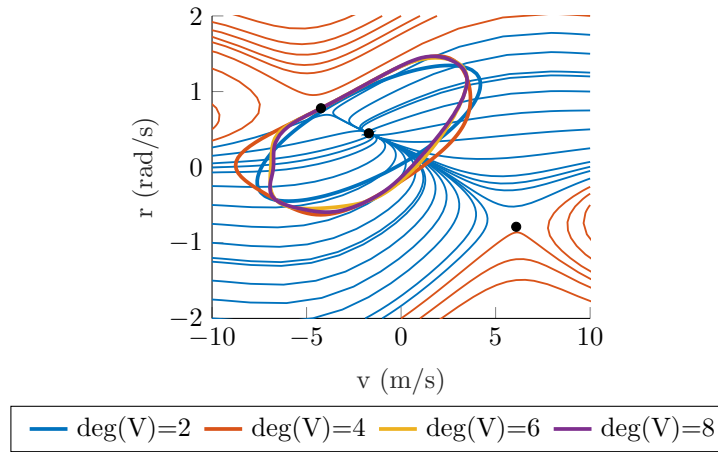


Figure 5.3. RoA estimates for a constant cornering maneuver using $s(x) = Vlin$.

Note that the level set β of $s(x)$ has no room for enhancement. In both cases, the stability boundary was reached and the effectiveness of the estimation is defined by the shaping function alignment.

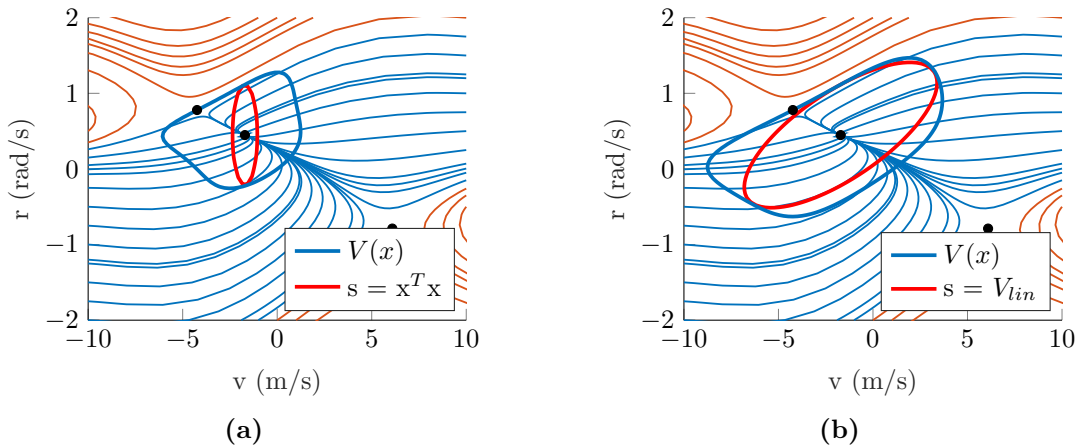


Figure 5.4. Influence of $s(x)$ on the RoA estimate. $V(x)$ is a 4th order polynomial function. In (a) $s(x) = x^T x$ and (b) $s(x) = V_{lin}$.

In an attempt to find a more representative estimation, we follow the suggestion presented in [Masouleh and Limebeer, 2017]. A Lyapunov function of lower degree shall be used as the shaping function for higher-order searches, in this case, $s(x)$ is bootstrapped with the previous Lyapunov function. For example, $s(x)$ is defined as our best second-order $V(x)$, obtained from previous runs, when searching for a fourth-order $V(x)$, and so on. The idea comes from the fact that as the degree of the Lyapunov function is increased, region Ω_γ better aligns with the gradient and, therefore, is a suitable $s(x)$ candidate for new searches. The solution comes with the drawback of systematically increasing the order of SOS polynomials and the fact that it must be run multiple times.

This approach will be employed for the remaining analysis in this work. The improve-

ment in doing so can be seen in Figure 5.5. In contrast with the results in Figure 5.3, the largest region's area we can show that are stable went from 14.95 to 21.04.

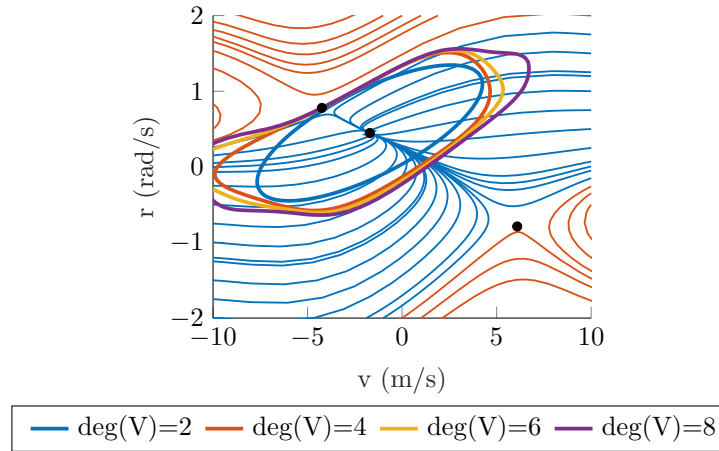


Figure 5.5. RoA estimate for the case where function $s(x)$ is defined as the previous Lyapunov function.

Interestingly, when we boost $s(x)$ to be our best $V(x)$, we search for a region that contains the previous one. Therefore, we should expect better estimations for each new run, a characteristic that motivates increasing the degree of the Lyapunov function being sought. This is confirmed by analyzing the estimated RoA's areas for each of the discussed methods, as shown in Table 5.2.

Table 5.2. Rising area of the estimated RoA as increasing the order of polynomial $V(x)$.

$s(x)$	$\deg(V)$			
	2	4	6	8
V_{lin}	11.5631	14.9534	13.0326	12.8980
Bootstrapped	11.6949	16.3942	18.6345	21.0372

5.2.2 Expanding the RoA with state feedback and input saturation

Now that the RoA can be estimated properly, we wish to design a state feedback controller that expands these regions. For the application, it is crucial to account for input saturation inherent to the vehicle under study.

As we mentioned before, the polynomial tire model approximation makes the resulting system non-affine in the input δ . Closer inspection of model

$$\begin{aligned} \dot{v} &= \frac{F_{yf} + F_{yr}}{m} - ru_0, \\ \dot{r} &= \frac{aF_{yf} - bF_{yr} + M_z}{I_z}, \end{aligned} \quad (5.4)$$

one can see that input M_z only affects \dot{r} . Recall that $x = [v, r]^T$, $u = [\delta, M_z]$, and lateral forces F_{yi} are functions of x and δ ($F_{yi}(v, r, \delta)$). The above system is rewritten in a general form

$$\dot{x} = f(x) + g_1(x, \delta) + \underbrace{\begin{bmatrix} 0 \\ 1/I_z \end{bmatrix}}_{g_2(x)} M_z, \quad (5.5)$$

where $g_2(x)$ is explicitly obtained. The definition of $g_1(x)$, on the other hand, requires some abstraction. Due to the 7th order polynomial (5.1), the control actuation has elements of the form

$$g_1(x, \delta) = g_{1_1}(x)\delta + g_{1_2}(x)\delta^2 + \dots + g_{1_7}(x)\delta^7. \quad (5.6)$$

As addressed in Chapter 4, to use the tools provided by Algorithm 2, $g_1(x, \delta)$ must be affine in δ . For this reason, (5.6) is reduced here to its first order approximation

$$g_1(x, \delta) \approx g_1(x, \bar{\delta}) + \left. \frac{\partial g_1}{\partial \delta} \right|_{x, \bar{\delta}} (\delta - \bar{\delta}). \quad (5.7)$$

Hence, substituting (5.7) into (5.5)

$$\dot{x} = \underbrace{f(x) + g_1(x, \bar{\delta}) - \left. \frac{\partial g_1}{\partial \delta} \right|_{x, \bar{\delta}} \bar{\delta}}_{\bar{f}(x)} + \underbrace{\left. \frac{\partial g_1}{\partial \delta} \right|_{x, \bar{\delta}}}_{\bar{g}_1(x)} \delta + g_2(x)M_z, \quad (5.8)$$

which can be written as

$$\dot{x} = \bar{f}(x) + \bar{g}_1(x)\delta + g_2(x)M_z, \quad (5.9)$$

where \dot{x} is affine in δ and M_z and thus, the iterative bounding procedure can be applied. Now we can search for control laws $K_1(x)$ and $K_2(x)$ that expand the region of attraction of the vehicle system.

We will now focus our attention on expanding the RoA with state feedback and input saturation. In an attempt to get better estimates, as discussed above, $s(x)$ is bootstrapped by the previous Lyapunov function. Again, the steering angle is set to 5 degrees with a constant longitudinal velocity of $u_0 = 10m/s$. The controller saturation bounds are $|\delta| \leq 20$ degrees and $|M_z| \leq 1200$ Nm.

Parameters initialization of Algorithm 2 are kept the same with a slight modification:

$$\begin{aligned} \deg(q_7) &= \deg(g) + \deg(K) + \deg(q_8) - 1, \\ \deg(q_{\{13,17\}}) &= \max\{\deg(K) - \deg(V), 2\}. \end{aligned}$$

For the same reasons that motivate the search over high order Lyapunov Function, we also search for control functions of degrees up to 4 in an attempt to obtain better results. Figure 5.6 shows the RoA estimates for certain combinations of K and V . It is straightforward to see that RoA estimates are indeed increased with a state feedback controller. The RoA surpasses the upper stability boundary, also comprehending the saddle point, indicating that the covered portion is now stabilized by the control law. Most importantly, satisfying the input saturation constraints.

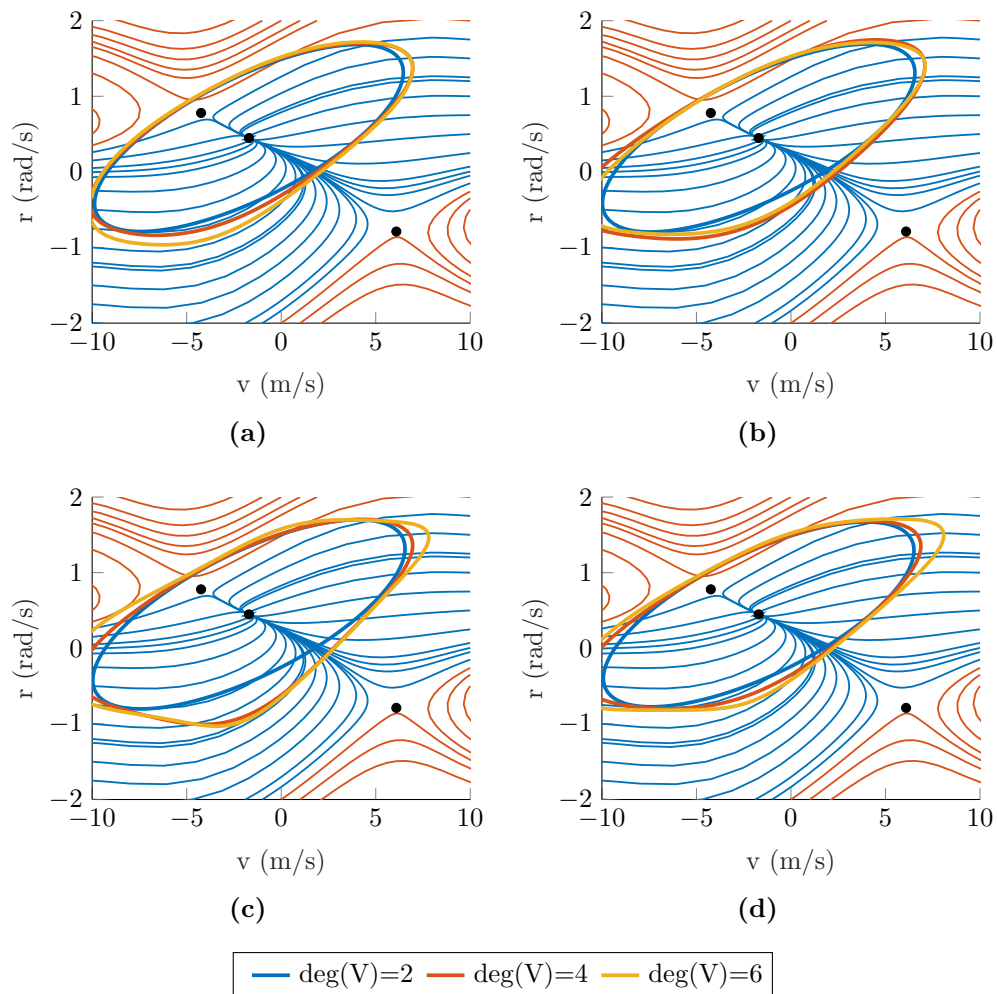


Figure 5.6. Estimated RoA of the controlled system for a constant cornering maneuver. In the background, we show the phase plane of the open-loop system. RoA is estimated by considering control laws K of (a) first-, (b) second-, (c) third-, and (d) fourth-orders.

Increasing the controller degree slightly expands the RoA estimates. In fact, the higher-order polynomial controller contains the lower ones, thus RoA is indeed expected to increase as far as numerical ill-conditioning arises. For these simulations, searching for a Lyapunov function of order 8 resulted in numerical failure. The rationale for this failure is that, by growing the order of K and V , high degree monomials are used in the SOS program, as consequence, the number of variables increases and the order of the

polynomial coefficients become vastly different.

Table 4.1 shows the area of the RoA estimates as a metric of comparison. It follows that the area increases as we increase the order of polynomials $K_i(x)$ and $V(x)$. As expected, increasing the Lyapunov function order gives a more representative estimate of the RoA and, similarly, increasing $K(x)$ order also potentially leads to improvements since we widen the search space.

The discussion is confirmed in the Table 4.1. The results are, however, marginally improving. Moreover, for $\deg(K) = 4$, the estimation started to be compromised, noticed by the decrease in RoA estimation.

Table 5.3. Area of the estimated RoA under a polynomial state feedback controller of arbitrary degree.

deg(K)	deg(V)		
	2	4	6
1	22.5626	24.2682	26.0119
2	23.2137	27.4919	25.7333
3	23.3177	27.8489	30.2255
4	22.7976	25.0768	27.7607

In practice, the preferred controller would be chosen according to its ability to expand the region of attraction. Clearly, the larger the RoA's area, the larger the set of initial conditions for which the controller will asymptotically stabilize the system. Additionally, one concern at the control design stage is the numerical conditioning of the control gains. The computed gains are shown in Table 5.4, occasional numerical bad-scaling or ill-conditioning are not observed.

Variables \bar{v} and \bar{r} are expressed in their respective coordinate system, i.e., $\bar{v} = v - v_{eq}$ and $\bar{r} = r - r_{eq}$. Note that the coefficients of K_1 and K_2 are related to their respective inputs that considerably differ in order of magnitude. $K_1(x)$ is with respect to input δ , expressed in radians, and $K_2(x)$ with respect to M_z , given in kNm . Furthermore, the polynomial's coefficients of odd exponents have significantly smaller values than their even pairs. This is comprehensible, since they always make a positive contribution to the control effort, regardless of the error.

5.2.3 SOS vs LQR control performance

We now wish to compare the control synthesis using SOS decomposition with other known control design techniques. Among the optimal controllers in control theory, the linear quadratic regulator is a well-known design approach that provides practical feedback

Table 5.4. Polynomial control gains K_i of degrees varying from 1 to 4 obtained with the sixth-order Lyapunov Functions. K_1 and K_2 are the state feedback control gains of inputs δ and M_z , respectively.

First-order
$K_1(x) = -0.038\bar{v} + 0.099\bar{r}$
$K_2(x) = 154.39\bar{v} - 839.35\bar{r}$
Second-order
$K_1(x) = 1.69 \times 10^{-3}\bar{v}^2 - 0.04\bar{v}\bar{r} + 0.06\bar{r}^2 - 0.01\bar{v} + 0.03\bar{r}$
$K_2(x) = -5.24\bar{v}^2 + 84.43\bar{v}\bar{r} - 172.28\bar{r}^2 + 101.14\bar{v} - 814.33\bar{r}$
Third-order
$K_1(x) = 0.006\bar{v}^2\bar{r} - 0.03\bar{v}\bar{r}^2 + 0.07\bar{r}^3 - 0.04\bar{v}\bar{r} + 0.07\bar{r}^2 - 0.003\bar{v} - 0.04\bar{r}$
$K_2(x) = -1.39\bar{v}^3 + 2.09\bar{v}^2\bar{r} + 36.29\bar{v}\bar{r}^2 - 75.80\bar{r}^3 - 4.55\bar{v}^2 + 70.89\bar{v}\bar{r} - 218.28\bar{r}^2 +$ $+134.05\bar{v} - 637.57\bar{r}$
Fourth-order
$K_1(x) = -2 \times 10^{-4}\bar{v}^4 + 2.6 \times 10^{-4}\bar{v}^3\bar{r} + 0.01\bar{v}^2\bar{r}^2 - 0.05\bar{v}\bar{r}^3 + 0.07\bar{r}^4 - 1.9 \times 10^{-4}\bar{v}^3 +$ $+0.01\bar{v}^2\bar{r} - 0.06\bar{v}\bar{r}^2 + 0.13\bar{r}^3 + 3.1 \times 10^{-3}\bar{v}^2 - 0.02\bar{v}\bar{r} - 0.02\bar{r}^2 - 0.01\bar{v} + 0.11\bar{r}$
$K_2(x) = 0.1\bar{v}^4 - 0.96\bar{v}^3\bar{r} - 6.5\bar{v}^2\bar{r}^2 + 73\bar{v}\bar{r}^3 - 111.4\bar{r}^4 - 0.25\bar{v}^3 - 6.54\bar{v}^2\bar{r} + 73.59\bar{v}\bar{r}^2 -$ $-220.30\bar{r}^3 - 7.94\bar{v}^2 + 87.12\bar{v}\bar{r} - 184.51\bar{r}^2 + 82.47\bar{v} - 395.69\bar{r}$

gains. We use the linear system (2.15) (see Chapter 2, Section 2.5)

Control gain is calculated by $K = R^{-1}B^T P$ where P can be found by solving the continuous-time algebraic Riccati equation. The quadratic components, Q and R , that establish a compromise between control effort and performance, are chosen to be

$$Q = \begin{bmatrix} 5 & 0 \\ 0 & 50 \end{bmatrix}, \quad R = \begin{bmatrix} 1 \times 10^3 & 0 \\ 0 & 4 \times 10^{-3} \end{bmatrix}, \quad (5.10)$$

where Q and R are with the international system units.

Given the control gain, we can evaluate Algorithm 1. In this case, we are not synthesizing a control law, but rather, estimating the region of attraction of the closed-loop system. We must nonetheless include at the algorithm's steps (i) and (iii) the input saturation constraints.

Figure 5.7 shows the estimated RoA for the system under the LQR control. Comparing to Figure 5.6, the region is very similar in shape and alignment, but not in size. The estimated RoA clearly comprehends the upper saddle point and surpasses the boundary of the open-loop plant, however, due to the fixed controller law, the algorithm quickly converges.

The areas of the estimated RoAs are shown in Table 5.5. As expected, the region enlarges as we increase the Lyapunov function order. Comparing with the areas of Table

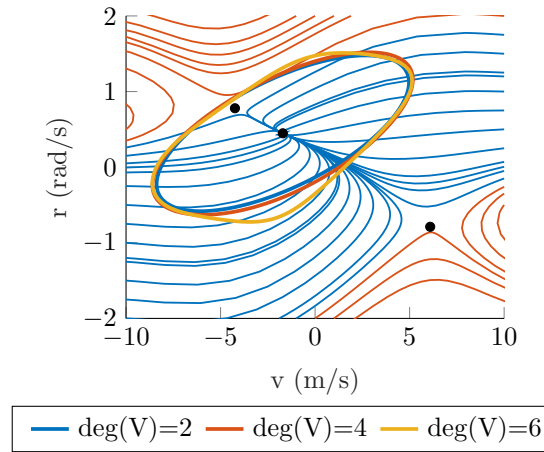


Figure 5.7. Estimated region of attraction for the system under the LQR control. In the background are shown the phase plane of the open-loop plant. Lyapunov functions are shown for different degrees.

5.3, the estimated RoA under an LQR control gain is remarkably lower.

Table 5.5. Area of the estimated RoAs for the system under the LQR control.

deg(V)	2	4	6
Area	16.3337	17.6150	18.7786

5.3 Rational Polynomial Approximation

Although polynomial models have a simple form, the fitting is sensitive to the data chosen. Any polynomial is radially unbounded, consequently, the approximation deteriorates outside the data range. Moreover, the fitting error decreases as the order of the polynomial is increased. However, overly increasing the polynomial order inevitably leads to unstable models, restricting their use. Following the suggestion made in [Masouleh and Limebeer, 2017], a constructive tire force approximation is achieved utilizing the class of rational polynomial functions. Therefore, we choose

$$F_{y_i}(\alpha) = \frac{F_{y_i}^N}{F_{y_i}^D} = \frac{p_{i1}\alpha_i + p_{i2}\alpha_i^2 + p_{i3}\alpha_i^3}{q_{i1} + q_{i2}\alpha_i^2 + \alpha_i^4}, \quad (5.11)$$

where coefficients p_{ij} and q_{ij} are found with the least-squares algorithm. $F_{y_i}^N$ and $F_{y_i}^D$ are the numerator and denominator terms with $i \in \{f, r\}$. For small values of α_i the rational function reduces approximately to its linear model ($p_{i1}\alpha_i/q_{i1}$) and, for higher α_i values, the function scales to the horizontal asymptotes, coinciding to the force saturation. A comparison between the rational function (5.11) and a 7th-order polynomial model (5.1)

are shown in Figure 5.8. The fitting errors are evident.

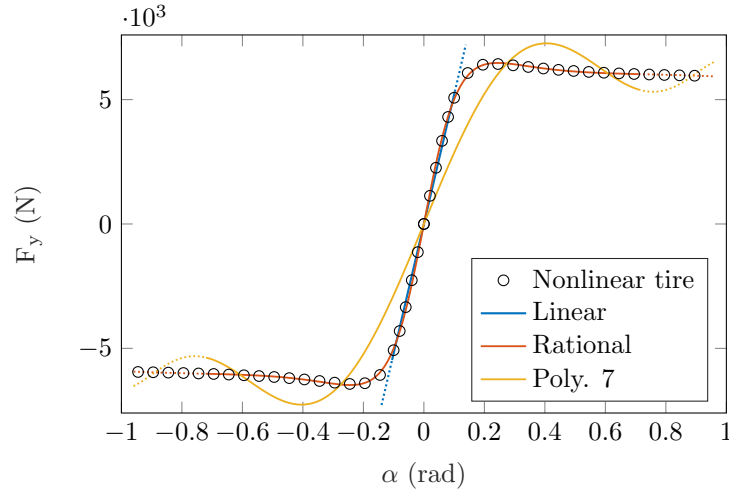


Figure 5.8. Pacejka’s nonlinear tire force and its polynomial approximations using the linear, rational, and polynomial models.

To validate the rational approximation and justify its usage, we compare the phase plane of the resulting models. The trajectories of the bicycle model using the magic formula tire (solid lines) and its polynomial approximation (dashed lines) are shown in Figure 5.9. Left and right plots present the trajectory of the system assembled with the 7th-order polynomial approximation (5.1) and the rational model (5.11), respectively.

Note that the approximation deviates the equilibrium points. In particular, the polynomial approximation causes the stable region to appear larger than it really is and errors in the trajectory are strongly noticeable. On the other hand, the rational model approximation shows a satisfactory trajectory agreement. We can, therefore, make use of the rational approximation to estimate the RoA expecting more accurate and reliable results.

The system of rational polynomial ordinary differential equations are obtained by substituting the rational polynomial approximation (5.11) into (2.5). Again, the two complete equations describe the lateral dynamics with states $x = [v, r]^T$ and inputs $u = [\delta, M_z]^T$, which takes the form

$$\begin{aligned} \dot{v} &= \frac{\frac{F_{y_f}^N}{F_{y_f}^D} + \frac{F_{y_r}^N}{F_{y_r}^D} - mru_0}{m}, \\ \dot{r} &= \frac{a\frac{F_{y_f}^N}{F_{y_f}^D} - b\frac{F_{y_r}^N}{F_{y_r}^D} + M_z}{I_z}. \end{aligned} \tag{5.12}$$

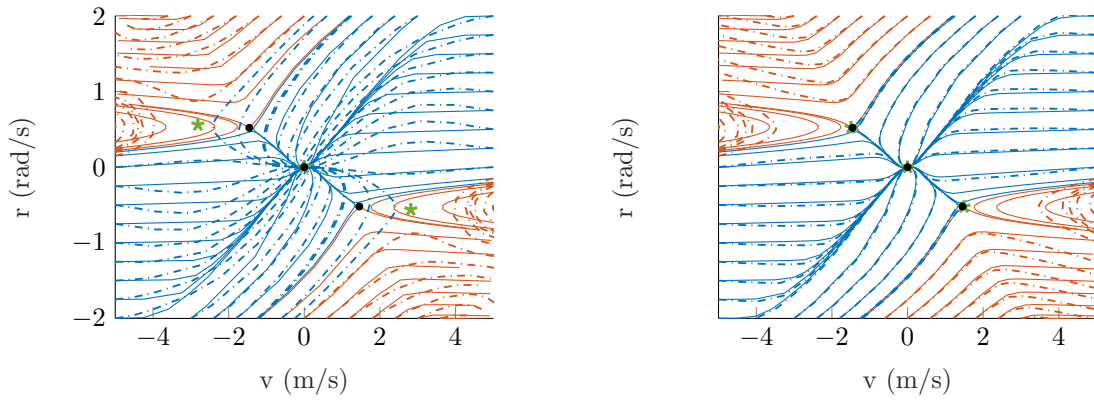


Figure 5.9. Phase portrait for the bicycle model using the magic formula tire (solid lines) and the approximated polynomial tire (dashed lines). Black dots and green stars are equilibrium points of the real and approximated model, respectively. On the left, the system is assembled with a 7th order polynomial tire force approximation, and on right with the rational polynomial approximation.

Rearranging the terms, (5.12) can be expressed as

$$\dot{v} = \frac{(F_{y_f}^N F_{y_r}^D + F_{y_r}^N F_{y_f}^D - m r u_0 F_{y_f}^D F_{y_r}^D) I_z}{d(x, u)}, \quad (5.13)$$

$$\dot{r} = \frac{(a F_{y_f}^N F_{y_r}^D - b F_{y_r}^N F_{y_f}^D + M_z F_{y_f}^D F_{y_r}^D) m}{d(x, u)} \quad (5.14)$$

with $d(x, u)$ being the common denominator

$$d(x, u) = F_{y_f}^D F_{y_r}^D m I_z. \quad (5.15)$$

It is important to note that $F_{y_f}^N$ and $F_{y_f}^D$ are functions of states x and input δ . This increases considerably the complexity of our algorithm. With a closer inspection of (5.14), we see a product of inputs in the $M_z F_{y_f}^D F_{y_r}^D$ term (product of δ and M_z). In addition, due to the polynomial approximation (5.11), lateral forces $F_{y_f}^N$ and $F_{y_f}^D$ necessarily contain elements with exponents of third and fourth orders. This makes the resulting model non-affine in the input δ . Its general representation is

$$\dot{x} = \frac{f_n(x) + g_n(x, u)}{d(x, u)} \quad (5.16)$$

where $f_n : \mathcal{D} \rightarrow \mathbb{R}^n$ is a vector of polynomial state functions, $g_n : \mathcal{D} \rightarrow \mathbb{R}^n$ is a vector of polynomial control functions and $d : \mathcal{D} \rightarrow \mathbb{R}$ the polynomial denominator function. Along the same lines as before, an approximation in order to make the system affine in u

is necessary.

Given the rational state space representation (5.16), the input-affine approximation is achieved by a linearization over a given input $\bar{u} = \bar{K}(x)$. It captures the linear behavior of the control actuation $g_n(x, u)$ around the stable system, i.e., around the trajectories within the domain stabilized by the control law $\bar{K}(x)$. Likewise, the denominator $d(x, u)$ has nonlinear inputs elements and must be approximated to an input-affine function. With $u = K(x)$ and for a given input $\bar{u} = \bar{K}(x)$, the first-order approximation of elements $g_n(x, u)$ and $d(x, u)$ are

$$\begin{aligned} g_n(x, K(x)) &\approx g(x, \bar{K}(x)) + \left. \frac{\partial g(x, u)}{\partial u} \right|_{u=\bar{K}(x)} (K(x) - \bar{K}(x)), \\ d(x, K(x)) &\approx d(x, \bar{K}(x)) + \left. \frac{\partial d(x, u)}{\partial u} \right|_{u=\bar{K}(x)} (K(x) - \bar{K}(x)). \end{aligned} \quad (5.17)$$

The partial derivatives are evaluated at the known control $\bar{K}(x)$, and $K(x)$ is the yet unknown polynomial state feedback control law we wish to find. For instance, (5.17) is linear in the arguments of $K(x)$ and searching for the coefficients of this control law is now a convex problem.

By applying Algorithm 2, the region of attraction is expanded iteratively. At each iteration, the algorithm searches for a new $K(x)$ such that the solution moves towards the optimum β , in Program (4.21). Furthermore, each sub-optimal $K(x)$ obtained from iteration k is used as $\bar{K}(x)$ of iteration $k + 1$. The algorithm requires an initial candidate $\bar{K}_0(x)$.

Substituting (5.17) into (5.16), reorganizing the corresponding terms and for our particular case of two inputs, $u_1 = K_1(x)$ and $u_2 = K_2(x)$, the state space representation can be written as

$$\dot{x} \approx \frac{\bar{f}_n(x) + g_{n1}(x)K_1 + g_{n2}(x)K_1K_2}{d_f(x) + d_g(x)K_1} \quad (5.18)$$

where $\bar{f}_n(x)$ is the input-independent term, $g_{n1}(x)$ and $g_{n2}(x)$ are the control input vectors, $d_f(x)$ is the input-independent denominator term, and $d_g(x)$ the control input denominator term.

Extending the SOS non-negativeness conditions for rational functions have been shown appropriate in practical computations, as in [Masouleh and Limebeer, 2017, Drummond et al., 2018]. When the system of interest is of the form (5.18), SOS restriction (4.22) takes the form

$$\left(-\frac{\partial V}{\partial x} \left(\frac{\bar{f}_n + g_{n1}K_1 + g_{n2}K_1K_2}{(d_f + d_gK_1)} \right) q_8 - \varphi_2 + (V - \gamma)q_7 \right) \in \Sigma_n. \quad (5.19)$$

By multiplying (5.19) for the non-zero denominator $(d_f + d_g K_1)$, we achieve the restriction

$$\left(-\frac{\partial V}{\partial x} (\bar{f}_n + g_{n1} K_1 + g_{n2} K_1 K_2) q_8 - (d_f + d_g K_1) \varphi_2 + (d_f + d_g K_1) (V - \gamma) q_7 \right) \in \Sigma_n, \quad (5.20)$$

that can be now tractable using Algorithm 2.

Note that, due to $K_1 K_2$ term, there is still the product of the decision variables. The *Control design step (i)* of Algorithm 2 must be decomposed into two sub-steps, (i.1) and (i.2). We must hold fixed K_1 while searching for K_2 and vice versa. Therefore, instead (i) we now have (i.1) and (i.2):

(i.1) **K_1 -Step**: Maximize γ with V , K_2 and q_2 fixed to obtain K_1 such that (5.20) holds;

(i.2) **K_2 -Step**: Maximize γ with V , K_1 and q_2 fixed to obtain K_2 such that (5.20) holds;

set $K_1^{(i)} = K_1$, $K_2^{(i)} = K_2$ and proceed to the Algorithm's *Gamma step (ii)*.

As before, input saturation restrictions should be included accordingly. The remaining steps proceeds normally.

5.3.1 RoA estimation and state feedback design

The vehicle model is assembled using the rational model and the RoA estimation and its expansion through state feedback are shown for two scenarios. First, the equilibrium point is located at the origin, representing a straight running scenario, and second, the analysis is developed for a constant cornering maneuver.

Straight running scenario

As a first application, we estimate the RoA for a straight running condition. Steering angle is set to 0 degree with constant longitudinal speed $u_0 = 10$ m/s. The results are shown in Figure 5.10, where the phase portrait of the polynomial vehicle model is shown in the background along with the equilibrium points, denoted by black dots. Moreover, regions Ω_γ , which are our estimates of the region of attraction, are shown for four Lyapunov functions with different degrees.

Consistent with the results presented above, the RoA estimates become more representative as we increase the degree of $V(x)$. Given all the manipulations necessary to handle the class of rational polynomial models, Figure 5.10 is a strong indicator of correctness.

Now we wish to design a state feedback controller that expands the aforementioned regions. The RoA estimates for the closed-loop system are presented in Figure 5.11. It is straightforward to verify that the RoA estimations are increased with the state feedback

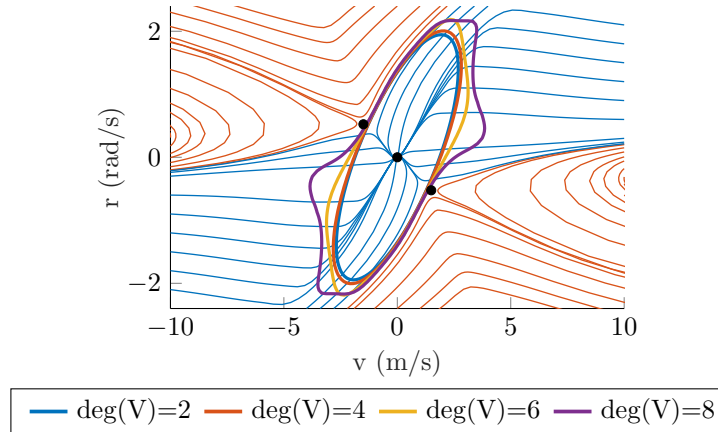


Figure 5.10. RoA estimates for a straight running scenario ($\delta = 0$) with constant longitudinal speed $u_0 = 10$ m/s. Lyapunov functions are shown for different degrees. In the background, we show the phase plane of the open-loop system, with blue and orange lines representing the stable and unstable trajectories, respectively.

controller. The RoA surpasses the stability boundary, also comprehending the saddle points, indicating that the covered portion is now stabilized by the control law. Most importantly, satisfying the input saturation constraints.

Although we have imposed a steering saturation constraint of 20 degrees, the maximum and minimum values of the steering commands achievable with points inside the RoA are 7.56 and -7.56 degrees, respectively. Beyond a certain value, the force generated by the tire is friction-limited (see Figure 5.8), meaning that increasing the steering angle not necessarily leads to an increase in the lateral response.

For the RoA computation, searching for an 8th order Lyapunov function resulted in numerical failure. The rationale for this failure is that, by growing the order of V , high degree monomials are used in the SOS program, as consequence, the number of variables increases and the order of the polynomial coefficients becomes vastly different, resulting in numerical ill-conditioning problems.

To numerically quantify these improvements, we report in Table 5.6 the RoA surfaces area. The progress we obtain advancing in the search of $V(x)$ of higher orders is evident. Moreover, as expected, the surface area is considerably larger for the closed-loop scenario.

Table 5.6. Estimated RoA areas (m rad/s²) for the open-loop and closed-loop scenarios of the straight running maneuver. NP: Numerical Problems.

Case study	deg(V)			
	2	4	6	8
open-loop	11.4173	12.0566	13.9910	15.8461
closed-loop	21.8949	29.9276	31.2915	NP

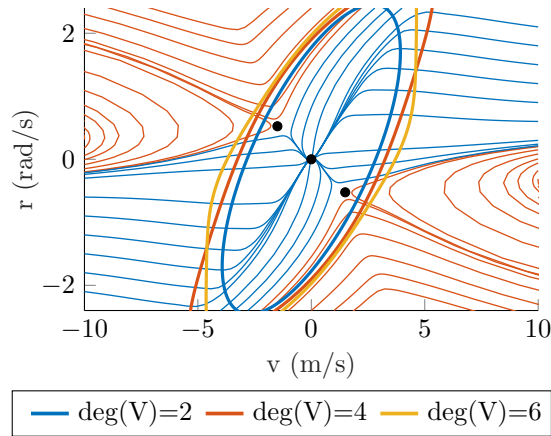


Figure 5.11. Estimated RoA of the controlled system for a straight running maneuver. In the background, we show the phase plane of the open-loop system. The estimated RoA under a control law $K(x)$ overcomes unstable paths around the saddle points. Furthermore, the input saturation bounds recognized in Table 6.1 are used in the control design.

Cornering maneuver

As a second verification, we consider a constant cornering maneuver. The steering angle is set to -5 degrees with constant longitudinal velocity $u_0 = 10$ m/s. As shown in Figure 5.12, the phase plane is no longer symmetric and the equilibrium point is not at the origin, which means that the system must be shifted to the origin via a change of variables $\bar{x} = x - x_{eq}$.

From Figure 5.12, one can note the estimated RoAs are remarkably smaller when compared to those obtained for the straight running maneuver. As the equilibrium is now displaced from the origin and more close to the stability boundary, the enlargement of the estimated region Ω_γ is compromised. The shift of the \mathcal{S}_β region closer to the stability boundary makes it more difficult for the algorithm to approximate the RoA with the prior levels of accuracy, limiting its expansion.

We now design a state feedback that expands the RoA. Again, we search for a first-order polynomial control law $u = K(\bar{x})$ with $K(\bar{x}) \in \mathbb{R}[x]$ while accounting for input saturation.

The estimated RoAs for the closed-loop system are shown in Figure 5.13. As one might expect and in agreement with the previous results, better estimations are obtained for higher-order $V(x)$. For the same reasons discussed previously, designing a control law $K(\bar{x})$ while searching for an 8th order Lyapunov function resulted in numerical failure.

Furthermore, the maximum and minimum values of the steering commands achievable with points inside the RoA are 11.64 and -9.79 degrees, respectively. The values are no longer symmetric simply because the feasible region for the cornering maneuver is asymmetric about the equilibrium.

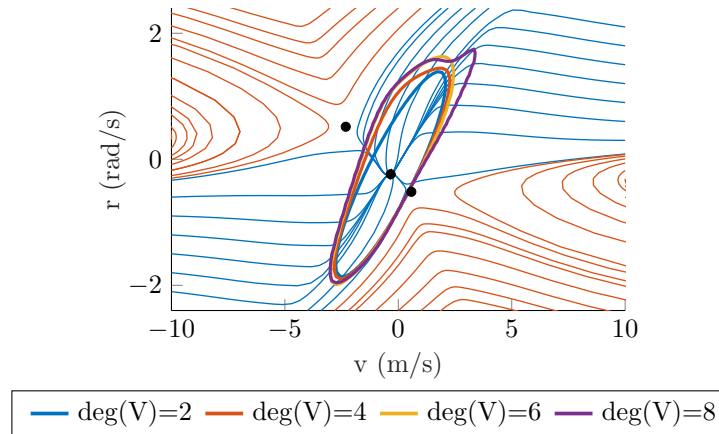


Figure 5.12. RoA estimates for the open-loop maneuver. The vehicle steering angle $\bar{\delta}$ is set to -5 degrees with constant longitudinal speed $u_0 = 10 \text{ m/s}$. The regions are estimated varying the degree of V from 2 to 8.

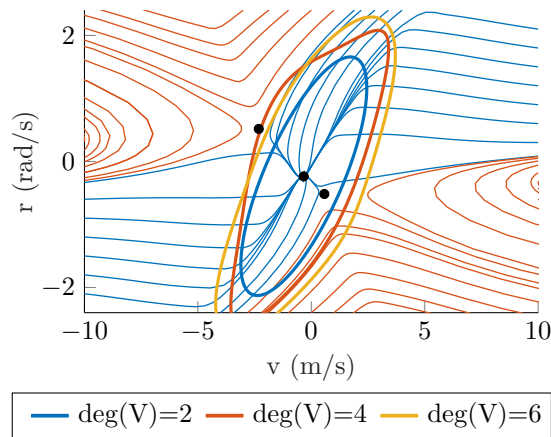


Figure 5.13. RoA estimates for the closed-loop maneuver. Phase plane is shown in the background. The regions are estimated varying the degree of $V(x)$ for a left-turn maneuver while synthesizing a first-order control law $K(x)$. Steering angle is set to -5 degrees with constant longitudinal speed $u_0 = 10 \text{ m/s}$.

The progress we obtain as advancing in the search of $V(\bar{x})$ and using the polynomial control law is shown in Table 5.7. Due to the asymmetric phase plane, the estimated RoA surface area is considerably smaller when compared to the straight running maneuver.

Table 5.7. Estimated RoA areas (m rad/s^2) for the open-loop and closed-loop scenarios of the constant cornering maneuver. NP: Numerical Problems.

Case study	deg(V)			
	2	4	6	8
open-loop	5.9247	7.1092	8.2808	9.0824
closed-loop	11.1227	17.5590	21.2290	NP

All the analyses were performed on a 4.00 GHz desktop PC with 32 GB RAM. The algorithm is iterative and the analysis and synthesis problems feature three and five steps, respectively. Table 5.8 summarizes the computational statistics for each of the above simulations. The computational times, given in seconds, are the total amount of time required to reach the stopping criterion.

Table 5.8. Computational statistics of Algorithms 1 and 2 for the open- and closed-loop analysis, respectively. NP: Numerical Problems.

Maneuver	Case study	Computational time (seconds)			
		deg(V)=2	deg(V)=4	deg(V)=6	deg(V)=8
Straight	open-loop	43.98	116.00	259.52	315.96
	closed-loop	286.40	363.14	584.57	NP
Cornering	open-loop	91.55	209.56	280.36	374.95
	closed-loop	353.54	595.78	1090.87	NP

5.3.2 Control performance evaluation

As mentioned, the SOS control design procedure is performed iteratively. At each iteration, the coefficients weights of $K(\bar{x})$ are found in order to optimize the given criterion.

As mentioned, in practice, the preferred controller would be chosen according to its ability to expand the region of attraction. Thereby, we choose the control gain that produces the largest area, in this case, obtained with the sixth-order Lyapunov function (see Table 5.7). The control gain of the latest iteration is

$$K(\bar{x}) = \begin{bmatrix} K_1(\bar{x}) \\ K_2(\bar{x}) \end{bmatrix} = \begin{bmatrix} 0.0598 \bar{v} - 0.0827 \bar{r} \\ 79.7875 \bar{v} - 91.0377 \bar{r} \end{bmatrix}. \quad (5.21)$$

The control gain performance is verified via simulation. The overall structure is presented in the block diagram of Figure 5.14 where $K(\bar{x})$ is the polynomial state feedback gain coupled with the feedforward value. Note that the control law is written in terms of the variable \bar{x} .

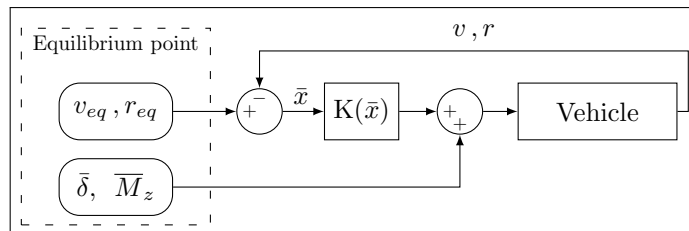


Figure 5.14. State feedback and feedforward tracking controller diagram.

Under the set of conditions and approximations made for synthesis purposes regarding the bicycle model, the predictions given in Section 5.3.1 are now validated through a higher-fidelity model. It includes the steering, powertrain, and suspension systems and uses the Pacejka tire model for the tire-ground interaction forces. The physical vehicle parameters are listed in Table 5.1. All values were extracted from [Cordeiro, 2017, Ribeiro, 2016] where the complete vehicle modeling and data validation are given. The simulator dynamics is formulated as a 32-states model. The vehicle is configured to simulate an independent rear-wheel drive vehicle, providing references of the vehicle states and measured signals.

The performance of the proposed controller is examined through a transition between equilibrium points. The vehicle starts from the origin and is set on an equilibrium point corresponding to a steering angle $\delta = -20^\circ$ and $u_0 = 8 \text{ m/s}$. At instant $t=5$ seconds, we change the desired point. The new reference is the stable equilibrium of Figure 5.13, achieved with $\delta = -5^\circ$ degrees and $u_0 = 10 \text{ m/s}$. In summary, the vehicle slightly accelerates with a decrease in steering angle.

The maneuver is evaluated under open and closed-loop scenarios. For the latter, the control law (5.21) is used to stabilize the system. The resulting response is discussed by highlighting three main stages, as displayed in Figures 5.15 and 5.16.

During stage (I) the vehicle is at equilibrium point $x_{eq} = [-0.9 \ -0.67]^T$. At 5 s the desired equilibrium point is changed. The longitudinal velocity reference u_0 is set from 8 to 10 m/s, which creates a small acceleration. Moreover, $\bar{\delta}$ is set to -5° . The desired equilibrium corresponds to the stable point (black dot) localized at the center of the phase-plane of Figure 5.15.

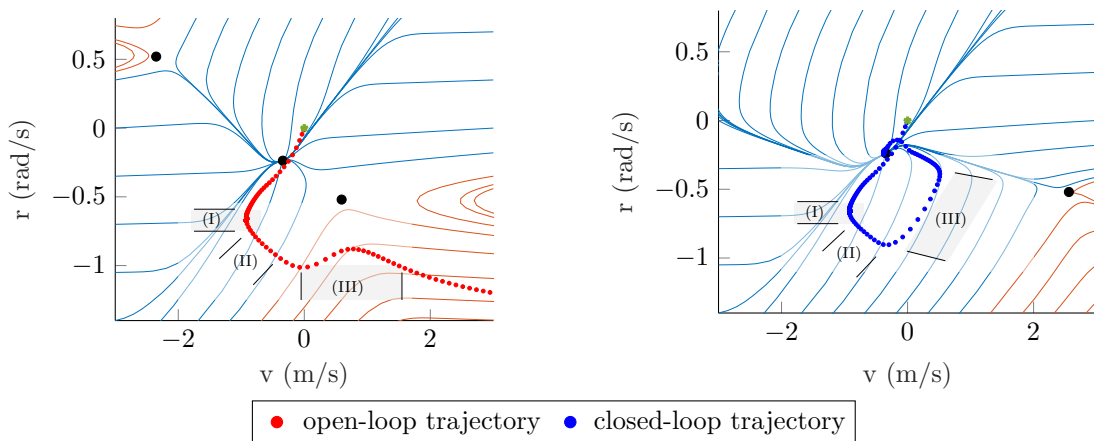


Figure 5.15. State trajectories (starting from the origin, shown as green stars) of the open and closed-loop scenarios. Phase plane are shown in the background for $\delta = -5^\circ$ and $u_0 = 10 \text{ m/s}$. Equilibrium points are denoted by black dots. On the right, the closed-loop trajectories are shown with the input saturation bounds recognized in Table 6.1.

The transient response is exhibited in stage (II). As the vehicle increases longitudinal

speed, lateral and angular velocities, v and r , slightly increase and decrease, respectively (see Figure 5.16). For the open-loop scenario, these deviations are sufficient to cross the stability boundary, as shown in Figure 5.15. On the other hand, for the closed-loop scenario, the state trajectory is still inside the domain of attraction of the closed-loop system, therefore, it is ensured that the vehicle will reach the desired equilibrium point.

Finally, stage (III) shows the maneuver completion. The open-loop response diverges and severely loses longitudinal speed. This is the reason for the poor agreement of the actual trajectory (red dots) with the one expected in the phase plane. In contrast, the closed-loop scenario converges to the desired equilibrium point and we can see a good agreement between the expected and the achieved trajectories. Figure 5.16 displays these responses over time.

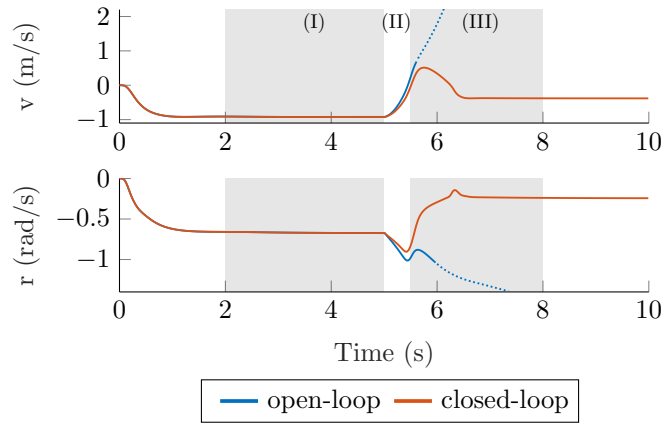


Figure 5.16. Vehicle lateral v and angular r velocities response of the open and closed-loop systems. The main stages are highlighted in three intervals and trajectory indicated by dots diverges.

The control efforts are shown in Figure 5.17. It should be mentioned that the yaw moment command must be transformed into torque references for the electric motors. This is achieved by approximating

$$\begin{aligned} T_l &= T_{l_0} + \Delta F_{x,l} r_w, \\ T_r &= T_{r_0} + \Delta F_{x,r} r_w, \end{aligned} \quad (5.22)$$

while satisfying the corrective yaw moment balance

$$M_z = \frac{c}{2} (\Delta F_{x,l} - \Delta F_{x,r}). \quad (5.23)$$

where T_l and T_r are the torque references for the left and right wheels, respectively, r_w is the wheel radius, and c is the wheel track. T_{l_0} and T_{r_0} are the torque values that generate the traction forces to sustain the vehicle in the desired forward velocity. Since we consider

constant longitudinal speed, we use a low-level PI controller that determines whether to increase or decrease the T_{l_0} and T_{r_0} , according to variations on the longitudinal speed. $\Delta F_{x,l}$ and $\Delta F_{x,r}$ are the amounts of change in the longitudinal forces necessary in order to generate the corrective yaw moment M_z .

The technique that optimally distributes the torque between the wheels is commonly denoted in literature by torque vectoring [Ataei et al., 2019]. The strategies are formulated based on different concepts, such as the available friction, information about the friction ellipse, to avoid power loss, aiming to increase energy efficiency or increasing the handling performance [Smith et al., 2018, Chatzikomis et al., 2019, Yuan et al., 2018]. To simplify the torque allocation, we choose a symmetric distribution, i.e., $\Delta F_{x,l} = -\Delta F_{x,r}$, corresponding to a force demand evenly distributed between wheels. With this assumption, (5.23) has one solution and torques T_l and T_r are straightforwardly obtained.

It can be observed in Figure 5.17 that, due to the equal torque distribution enforced by the low-level controller, the yaw moment is zero for the open-loop response. On the other hand, the yaw moment of the controlled vehicle does not return to zero. Because of the difference between the expected and achieved equilibrium point, a nonzero value is computed by the control law.

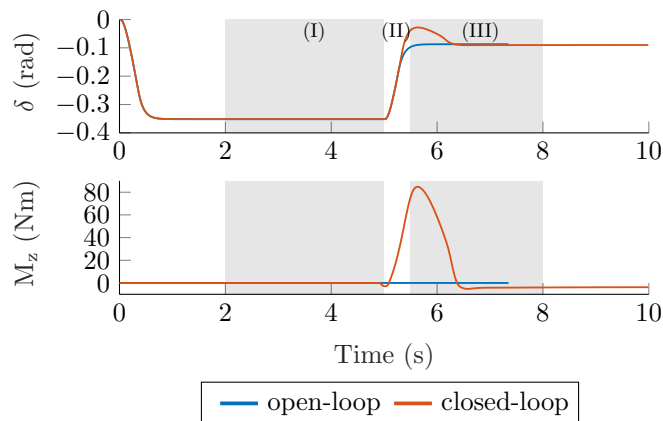


Figure 5.17. Comparison between the feedforward and the applied inputs by the proposed controller.

Although the expected equilibrium point was $x_{eq} = [-0.33, -0.24]^T$, the reached point was $x = [-0.37, -0.24]^T$. This difference is attributed due to the discrepancies between the approximated rational polynomial and the complete nonlinear model. Despite that, the controller was capable to stabilize the vehicle in the proposed scenario.

To illustrate the vehicle spatial response, we show in Figure 5.18 the performed trajectory for both scenarios. The transition between equilibrium points occurs at instant $t=5$ s and, at $t=5.5$ s the open-loop response crosses the stability boundary and the vehicle diverges.

The simulation results for this maneuver show that the obtained controller can prop-

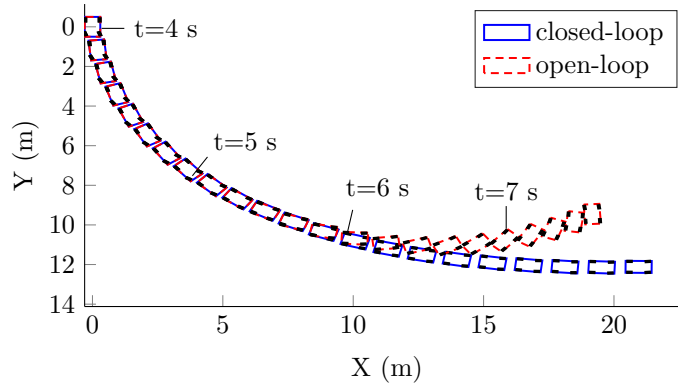


Figure 5.18. Vehicle trajectory and orientation.

erly provide handling improvement by applying a steering angle correction and an additional torque between the left and right wheels to achieve the yaw moment balance. Most importantly is that these results are a verification of the aforementioned region of attraction analysis. With the proposed closed-loop maneuver, the vehicle states remain inside the estimated RoA and, despite all the model simplifications proposed in this work, the stability certificate was valid, even when evaluated in a complete and representative vehicle model.

5.3.3 Effect of model dissimilarity

While the lumped tire model used throughout this work reflects the effect of lateral weight transfer upon the net lateral force capability at the front and rear wheels, it does not capture the effect of load transfer upon the individual wheels at an axle. Although the previous section showed a practical application where the vehicle stability was safeguarded by a stability certificate, obtained with the RoA estimation, special care should be taken due to implications of model dissimilarities.

Numerous studies about vehicle dynamics and stability [Wang and Chen, 2018, Kati et al., 2018, Galluppi et al., 2019, Németh et al., 2014, 2016, Tamba and Nazaruddin, 2018, Drummond et al., 2018, Masouleh and Limebeer, 2016, 2017] have hinted at the importance of design simplification for the development and application of their methodology, but to date, to the best of our knowledge, none have performed any rigorous analysis of this factor. The simplification should be warranted only if the final design outcome does not degrade substantially. Hence, there is a need to quantify the impact of the proposed approximations on the overall system performance.

The main shortcomings of the simplified bicycle model are well known: load transfer effects are neglected. The load transfer has a significant impact on tire behavior and thus, on vehicle stability. To determine the impact of these unmodeled effects in our analysis, we present a statistical validation of the predictions made in Section 5.3.1 using a higher

fidelity model. A Monte-Carlo analysis of initial conditions is employed to generate points inside and outside the predicted RoA.

Figure 5.19 shows the vehicle response for the straight running scenario, acquired from the higher fidelity model, and the largest estimated RoA, obtained using the bicycle model. Blue and orange dots are the initial conditions of the converging and diverging trajectories, respectively. It is noteworthy that all initial conditions inside the RoA should always converge to the origin, nonetheless, due to the divergence between the simplified and more elaborated model, some disparity among the predictions is observed.

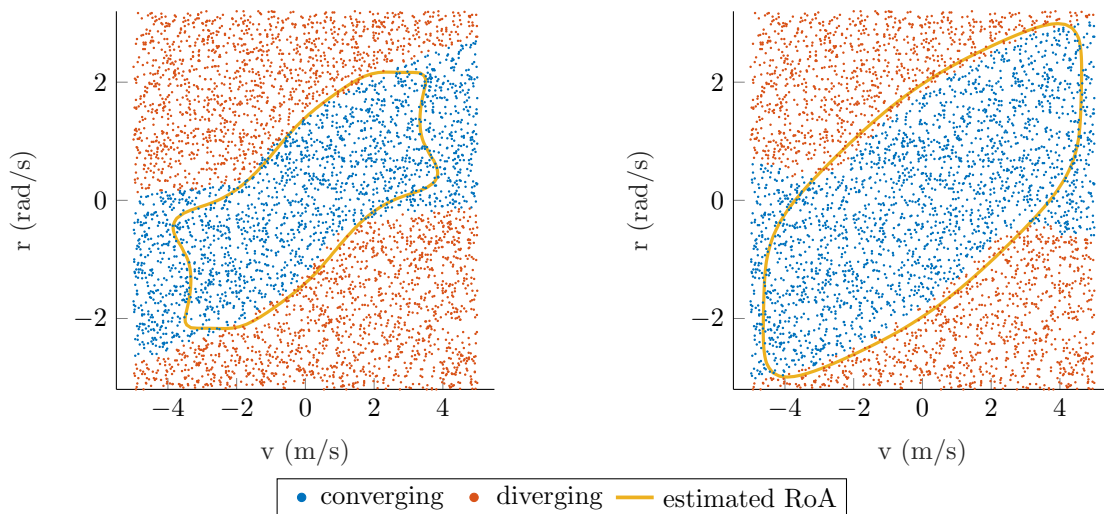


Figure 5.19. Vehicle response for the straight running scenario. The results are shown for the open-loop (left) and closed-loop (right) systems. Blue and orange dots are the initial conditions of the converging and diverging trajectories, respectively. The estimated RoA is the largest level set obtained in Section 5.3.1.

One can note in Figure 5.19, the diverging points within the RoA are located at the upper and lower boundaries of the level set curve. In fact, during the transient state trajectory, the vehicle expects varying levels of lateral acceleration, which tends to be larger as the distance between the initial condition and the equilibrium point increases. Since lateral acceleration strongly influences the vehicle's roll dynamics and therefore, the load transfer, divergences are more likely to occur when higher values of lateral acceleration are observed.

Table 5.9 reports on the statistical results of the converging and diverging trajectories. We can notice that the number of diverging results for the closed-loop scenario is considerably larger than the open-loop. With the bicycle model, we ignore the load transfer, regardless of the steering pattern incorporated by the closed-loop dynamics. This result is supported by the findings in [Liu et al., 1997], which showed that the factors associated with the steering angle had a great impact on the rollover analysis.

With respect to the cornering maneuver, where non-zero lateral accelerations are intrinsically observed, the number of divergent occurrences should be higher. As shown

in Figure 5.20, this is true for the closed-loop system. For the same reasons discussed above, the resulting steering pattern confers meaningful behavior properties that are not accounted for in the simplified model.

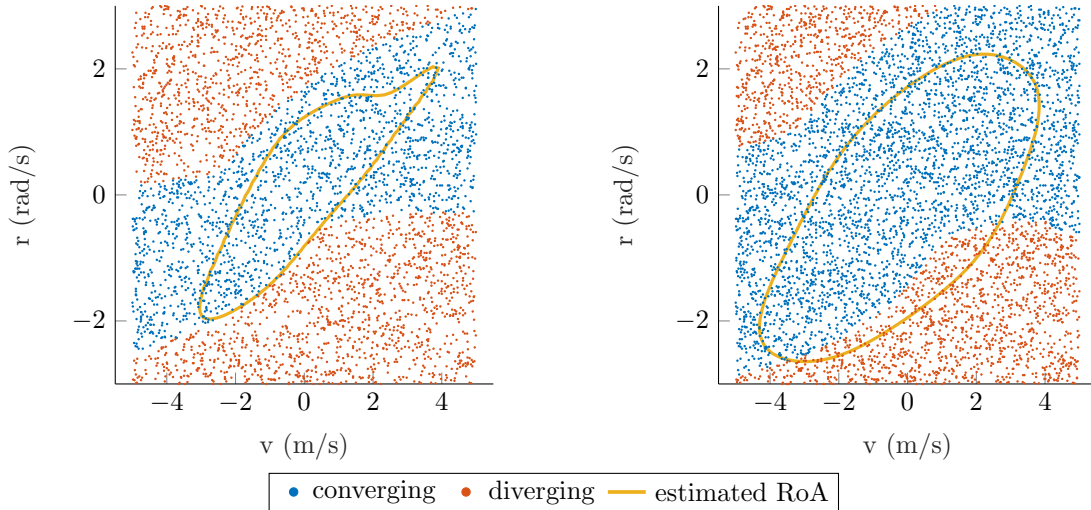


Figure 5.20. Results of the cornering maneuver for the open-loop (left) and closed-loop (right) system. Blue and orange dots are the initial conditions of the converging and diverging trajectories, respectively. The estimated RoA is the largest level set obtained in section 5.3.1.

However, for the open-loop cornering maneuver, an important characteristic is observed. Surprisingly, the RoA matches with the nonlinear vehicle behavior. The reason is that the estimated RoA, due to the conservatism in the overall estimation, did not hit the upper boundary of the stability region, where are located the highest values of lateral acceleration.

Table 5.9. A Monte-Carlo analysis of initial conditions inside the predicted ROA.

Maneuver	Case study	N ^o of points inside the RoA	Converging trajectories (%)	Diverging trajectories (%)
Straight	open-loop	1274	96.39	3.61
	closed-loop	2071	93.95	6.05
Cornering	open-loop	642	100	0.00
	closed-loop	2114	91.34	8.66

This characteristic leads to a second important reflection that is the number of stable occurrences that we were not able to estimate. Given the range plot of Figures 5.19 and 5.20, we report the number of stable trajectories and their portion covered by the estimation in Table 5.10.

By computing the invariant set around an equilibrium using the method discussed in this paper, an inner region of attraction is established. The best possible estimate for the

Table 5.10. A Monte-Carlo analysis of initial conditions located outside the predicted region of attraction.

Maneuver	Case study	N° of stable trajectories	Estimated portion (%)
Straight	open-loop	1981	61.99
	closed-loop	2300	84.39
Cornering	open-loop	1843	34.83
	closed-loop	3485	56.01

RoA using the Lyapunov function is given by the largest level curve of V . The size of the invariant set, however, may not be as representative as we might wish.

Because the feasible region for the cornering maneuver is asymmetric about the equilibrium, the region of attraction is inevitably more restrained when compared to the straight running motion. Moreover, any region calculated using a function that is symmetric about the equilibrium, such as an ellipsoid, ends up being rather conservative. Intuitively, this motivated our search over high order Lyapunov functions. In addition, for the synthesis problem, by restricting the range of operation for the controller, imposed by the input saturation constraints, we force an infeasible region that also limits the stability statements that can be made using the LF.

Despite the aforementioned negative effects associated with the load transfer behavior, the SOS-based controller is, indeed, able to obtain a large region of convergence around the desired equilibrium. This property is presented in Table 5.11 which shows the stabilized region achieved with the control law. These results are a strong indication that the proposed sum-of-squares methodology can be used as a valid analysis and design tool.

Table 5.11. Open-loop and closed-loop stable region of Figures 5.19 and 5.20.

Maneuver	Case study	Stable area (% of total)
Straight	open-loop	40.20
	closed-loop	52.61
Cornering	open-loop	40.75
	closed-loop	63.05

Regarding the disparity observed between the discussed models, two refinements to the design may enhance the fidelity of the analysis: the incorporation of the load transfer effects and the inclusion of longitudinal dynamics. With a three-state and four-wheel planar model, the wheels can be modeled individually and the coupling between the tire lateral and longitudinal forces considered. Nonetheless, the feasibility of the problem relies upon the resulting model being polynomial in its arguments. Moreover, the SOS polynomials will be a function of three arguments, which considerably elevates the problem complexity. Complexity, numerical conditioning, and an increase in the overall degree of

the vector field are notorious problems in SOS applications.

5.4 Final Remarks

In this chapter, we have shown how the sum-of-squares technique can be used in the stability analysis of a nonlinear vehicle system. The methodology, based on the construction of appropriate Lyapunov function certificates, is carried out using the tools provided by the SOS technique. Furthermore, estimating the region of attraction and designing a nonlinear state feedback control were explored algorithmically.

The ordinary differential equations of the well-known bicycle dynamics model are approximated by a rational polynomial vector field and two concomitant inputs are considered in the control design process, the steering angle, and yaw moment balance. The resulting model falls on a class of non-affine in the input system transforming the control design into a nonconvex problem. To circumvent this issue, we proposed an affine linearization, allowing the use of the SOS decomposition.

Two main subjects are approached in this work, the region of attraction estimation and its expansion through a nonlinear state feedback controller. Additionally, the proposed technique is capable of including the input saturation limits associated with the system actuator dynamics. The obtained control gains are validated under a simulation environment. Open and closed-loop scenarios are proposed to highlight the stability boundary of a vehicle system.

Concerning the model fidelity and validity, the efforts presented in this chapter were concentrated on the tire rational polynomial representation, which resulted in a suitable approximation. However, in particular, it was shown that the vehicle load transfer, especially resulting from the steering pattern, figures prominently in the vehicle stability. Because of this characteristic, a small divergence between the discussed models is reported.

The following publications were produced presenting the results of this chapter (Ribeiro, Fioravanti, Moutinho & de Paiva 2020b) and (Ribeiro, Fioravanti, Moutinho & de Paiva 2020c):

- A. M. Ribeiro, A. R. Fioravanti, A. Moutinho and E. C. d. Paiva. Sum-of-squares approach for ground vehicle lateral control under tire saturation forces. In *21th IFAC World Congress*, Berlin, Germany, July 11-17, 2020.
<https://doi.org/10.1016/j.ifacol.2020.12.1398>
- A. M. Ribeiro, A. R. Fioravanti, A. Moutinho and E. C. d. Paiva. Nonlinear state-feedback design for vehicle lateral control using sum-of-squares programming. *Vehicle System Dynamics*, 2020.
<https://doi.org/10.1080/00423114.2020.1844905>

6 Experimental Evaluation

6.1 Introduction

Car-like robots have shortened the path of building, testing, validating, and scaling algorithms for large scale cars. They account for nonholonomic constraints, imposed by the steering and propulsion systems, in agreement with today's conventional automotive vehicle basis, and are able to incorporate the complexity, uncertainties, and sensing capability introduced by real environments.

The car-like vehicle must follow certain restricted navigation laws, invariant of the path. Historically, this limited maneuverability motivated strategies that meet a variety of constraints, most remarkably, we mention the curvature restriction. In [Dubins, 1957] it was proposed a path planning algorithm that generates a minimal length trajectory that incorporates an average curvature restriction. Since then, the smoothness of a path has been considered as a challenging problem due to the nonholonomic constraint. In [Villagra et al., 2012] the shortest path is designed with bounded continuous curvature and bounded curvature derivative and [Liang et al., 2005] incorporated considerations of curvature constraint using cubic spirals segments to generate feasible trajectories. For smoothing the discontinuity between two geometric segments, the clothoid was used to generate a continuous-curvature path [Gim et al., 2017], also subjected to velocity constraints in [Frego et al., 2016].

Due to cost concerns, these strategies are often firstly presented for scaled vehicles. Moreover, for simplicity, most of the available strategies designed for car-like robots are mainly based on kinematics analysis. In many instances this may be a reasonable choice, however, for applications that require sufficient longitudinal velocity and experience a fairly lateral excitation, a dynamic analysis is necessary [Khalifa et al., 2019].

Towards this end, control strategies for car-like robots based on the vehicle dynamics naturally appeared in the literature [Ozcan and Ankarali, 2019, Hwang, 2016, Chen and Zhu, 2017]. This characteristic has led to an important reflection: the matching of the well-known dynamic response of a full-sized vehicle with the scaled car-like robot. Such concern was raised in [Polley et al., 2006] that provided insights and understanding of realistic nonlinear tire behavior for smaller vehicles. The authors concluded that the shapes of the force curves are qualitatively similar between scaled and full-sized tires. In

[Lapapong et al., 2009], a broadly dynamic similitude analysis is discussed and a close equivalence is observed for a wide range of input frequencies. The scaled car-like vehicle response matches the predictions from planar and non-planar dynamic models.

Scaled car-like vehicles can be used as valid and credible platforms. However, in practice, there are variables and coefficients present in the dynamical model which are difficult to measure or require dedicated facilities to be identified, often not easily available. The solution may be the use of estimation and identification schemes. Within this context, this work presents a comprehensive validation of a scaled car-like vehicle and thorough experimental testing. We present a parameter identification strategy, a stability analysis, and a model-based path following control that validates the vehicle as a reliable and valid vehicle platform for further studies.

The remaining sections of this Chapter are organized as follows. In Section 6.2, the motivations and characterization of the vehicle in the study are presented. Section 6.3 introduces the vehicle dynamic mathematical model. Section 6.4 shows the parameter identification method and an extensive validation which compares the agreement between numerical simulations with experimental data. In Section 6.5 the steady-state analysis is carried out and the vehicle equilibrium condition is identified. In Section 6.6 the SOS-based controller is verified experimentally, the identified parameters are used to assemble the vehicle dynamics and the steady conditions are used as the desired references.

6.2 Motivations

A four-wheeled 1:5-scale vehicle is used for the validation experiment. The platform, shown in Figure 6.1a, is based on an adapted HPI Baja 5B SS chassis with an independent rear-wheel drive and a steering system that follows the Ackermann geometry. It uses the ROS meta operating system as middleware and is equipped with a collection of commercial sensors such as encoders, global positioning system (GPS), inertial measurement unit (IMU), camera, light detection and ranging (LIDAR), and others. See [Nogueira et al., 2018] for a complete vehicle description and architecture exposition.

The major upgrades of the off-the-shelf chassis are the steering system geometry, given in Figure 6.1b, and the electric and independent rear-wheel drive, shown in Figure 6.1c.

Scaled driving platforms are largely employed in diverse theoretical fields as a useful complement to existing methods for testing proposed strategies. The motivation for using scaled vehicles is that it considerably simplifies the experimental validation task while keeping the same level of sensing capabilities of a full-sized vehicle. Recent progress and many publications are found detailing scaled test-beds for path planning [Berntorp et al., 2019, Pinto et al., 2019], filtering and estimation [Antunes et al., 2019], dynamic response analysis [Lapapong et al., 2009, Kozłowski, 2019], rollover prevention [Katzourakis et al.,

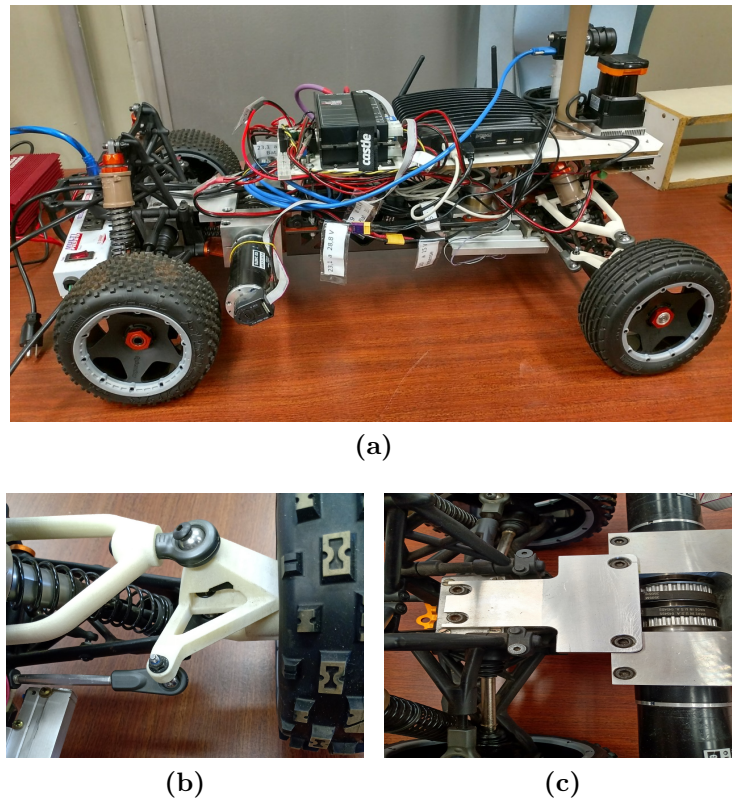


Figure 6.1. (a) Four-wheeled 1:5-scale platform. (b) Ackermann steering geometry. (c) The independent rear-wheel drive.

2010, Treetipsounthorn and Phanomchoeng, 2018], and for control validation in general [Yamaguchi et al., 2015, Karaman et al., 2017, Goswami et al., 2018, Bulsara et al., 2020]. A notorious platform is described in the AutoRally project [Goldfain et al., 2019]. It is an open-source, 1:5-scale vehicle test-bed, conceived for development in autonomous vehicle technologies.

Although these vehicles are designed and intended for different purposes, they all share common essential headlines: time, cost, and safety considerations to facilitate routine testing and experimentation. The vehicle depicted in Figure 6.1 also follows these considerations. The platform is large enough to effectively capture vertical dynamics and all their side effects, such as weight transfer, and to accommodate a range of sensors, allowing the validation of state-of-the-art algorithms.

From a practical point of view, elaborate strategies usually require the knowledge of parameters that have to be estimated. Regarding lateral vehicle dynamics, two meaningful fundamental and yet hard to know coefficients are the tire cornering stiffness and yaw moment inertia.

To validate and justify the scaled vehicle in the discussion, a model-based identification, analysis, and control schemes are proposed as a means of characterization of the scaled vehicle. In the next section, we review the vehicle modeling and follow to the proposed strategies used for identification and control.

6.3 Vehicle Modeling

The vehicle motion can be described by mathematical models with different levels of complexity and realism. For the purposes of this work, we will analyze the vehicle lateral motion and a proper balance between model fidelity and simplicity can be achieved using the nonlinear single-track model, also known as the bicycle model, depicted in Figure 6.2. A brief review of this model, presented in detail by Chapter 2, is given here.

The model assumes a single tire at each axle with twice the force capability of the individual tires. Additionally, it considers pure planar motion, neglecting roll and pitch dynamics.

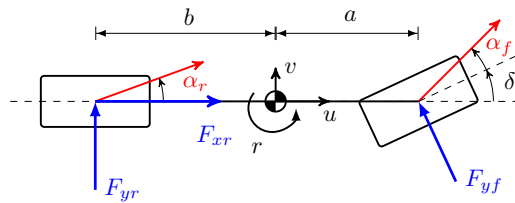


Figure 6.2. Diagram of the bicycle model.

The equations of motion are derived by analyzing the balance between forces and moments. From Figure 6.2, the lateral equations of motion are

$$\begin{aligned} m(\dot{v} + ru_0) &= F_{yf} \cos \delta + F_{yr}, \\ I_z \dot{r} &= aF_{yf} \cos \delta - bF_{yr}, \end{aligned} \quad (6.1)$$

where m is the vehicle mass, I_z is the yaw moment of inertia, and F_{yi} are the lateral forces with subscript $i \in \{f, r\}$ denoting front and rear wheels. Constants a and b are the distances from the center of gravity to front and rear axles, respectively, δ is the front tire steering angle and α_i are the tire slip angles. Finally, v , r , and u_0 are the vehicle lateral, angular, and longitudinal speeds. Observe that the decoupling between lateral and longitudinal motions is achieved considering a constant speed u_0 [Rajamani, 2011].

The main nonlinearity about (6.1) arises from the tire forces behavior. In this paper, we choose the brush tire model due to its simple and clear formulation. It has fewer parameters compared to the traditional Pacejka's model while maintaining the ability to capture the tire saturation [Pacejka, 2012].

The brush model is mainly dependent on the slip angle α_i . Tire slip is defined as the angle between the direction of motion and the wheel heading. From Figure 6.2 and

considering the kinematics motion we have

$$\begin{aligned}\alpha_f &= \frac{v + ar}{u_0} - \delta, \\ \alpha_r &= \frac{v - br}{u_0}.\end{aligned}\tag{6.2}$$

Following [Rajamani, 2011], the brush lateral tire force model is expressed as:

$$F_{yi} = \begin{cases} -\mu_i F_{zi} \text{sign}(\alpha_i), & \text{if } |\alpha_i| > \alpha_{sl_i}, \\ -2C_\alpha \sigma_y \left\{ 1 - |\theta_y \sigma_y| + \frac{1}{3}(\theta_y \sigma_y)^2 \right\}, & \text{o/w.} \end{cases}\tag{6.3}$$

where α_{sl_i} is the slip angle threshold needed to reach the full sliding condition, defined as

$$\alpha_{sl_i} = \tan^{-1} \left(\frac{3\mu_i F_{zi}}{2C_\alpha} \right),\tag{6.4}$$

and

$$\begin{aligned}\theta_y &= \frac{2C_\alpha}{3\mu_i F_{zi}}, \\ \sigma_y &= \tan \alpha_i.\end{aligned}\tag{6.5}$$

Coefficients μ_i are the available friction coefficient, F_{zi} are the vertical forces, and C_α is the tire cornering stiffness coefficient. The factor $2C_\alpha$ in (6.3)-(6.5) accounts for the fact that we assume a lumped axle with twice the capacity of a single tire, i.e., the equivalence between the bicycle and the four-wheel planar model. Moreover, due to vehicle symmetry, we have equal front and rear cornering stiffness, therefore, $C_{\alpha f} = C_{\alpha r} = C_\alpha$.

For the vertical forces, the static load transfer is assumed as:

$$\begin{aligned}F_{zf} &= bmg/(a + b), \\ F_{zr} &= amg/(a + b),\end{aligned}\tag{6.6}$$

where g is the gravitational acceleration.

Substituting from (6.2), (6.3), and (6.6) into (6.1), we assemble the two complete equations describing the lateral dynamics. The states are $x = [v, r]^T$ and input $u = \delta$. For a comprehensive analysis of the lateral vehicle model see [Rajamani, 2011, Chapter 2].

6.4 Parameter Identification

As seen in (6.1) and (6.3), the vehicle lateral behavior is strongly dependent on two fundamental parameters: tire cornering stiffness C_α and inertia I_z . This section details the offline estimation performed with the platform.

If a sufficiently large and representative dataset composed of measurements of states v and r is available, we can use data-based concepts to compare the model to data and estimate the desired parameters. This methodology can be seen as a problem of fitting experimental data to a nonlinear deterministic function.

The problem consists of finding the decision variables $x_p = [C_\alpha, I_z]^T$ that solve

$$\begin{aligned} x_p^* &= \underset{C_\alpha, I_z}{\operatorname{argmin}} (\lambda_1 e_{v,rms} + \lambda_2 e_{r,rms} + \lambda_3 C_\alpha + \lambda_4 I_z) \\ \text{s.t.} \quad & C_\alpha > 0, \\ & I_z > 0, \end{aligned} \tag{6.7}$$

where $x_p^* = [\hat{C}_\alpha, \hat{I}_z]^T$ is the optimum value that minimizes the objective function. Errors $e_{v,rms}$ and $e_{r,rms}$ are the states v and r root mean squared (*rms*) errors between the simulated and measured values. The design parameters $\lambda_1, \dots, \lambda_4$ define the set of weighting factors that indicates the importance of the residuals and the regularization.

If experimental data were free of error, coefficients C_α and I_z could be obtained straightforwardly by measuring the states at two points and solving the deterministic nonlinear model (6.1). For most practical applications this characteristic does not hold and a dataset collection should alternatively be used.

6.4.1 Data collection

Problem (6.7), as well as data analysis procedures in general, is heavily dependent on the dataset accuracy. It is imperative that the data accurately capture the process model [Rhinehart, 2016]. Additionally, when estimating parameters, one should ensure that the implicit assumptions on the distribution of the noise terms are reasonable. Here, the noises are independent and random disturbances with zero mean, or equivalently, white noise.

To yield meaningful information about the vehicle lateral response, we must gather a data set with a representative level of excitation. Towards this end, we use the swept sine wave as input, also known as chirp signal. It is a persistently exciting signal used to disturb the system over a specified range of frequencies [Honório et al., 2018].

In order to have a comprehensive and representative data set, a number of tests must be performed. The test consists of applying constant a longitudinal speed while employing the time-varying steer input. The process is repeated for several steering angle amplitudes and for different longitudinal speeds.

The dataset used in this work contains signals obtained varying the steer sine input amplitude from 10 to 25 degrees, with starting and ending frequencies of 1 and 6 Hz, respectively, and by setting three constant longitudinal speeds, 0.25, 0.6, and 1 m/s. A

total of 13658 measurements are gathered with a frequency of 10 Hz.

6.4.2 Experimental setup

For the experimental data discussed above and for the analyzes presented hereinafter, three class of sensors are used: simple motor encoders, the Xsens MTI-G-710 IMU unit, and the LIDAR Hokuyo UTM-30LX scanning laser.

The steering angle and longitudinal velocity are measured by encoders, with proper values calculated considering the mechanical gear and transmission ratio. Angular velocity r is straightforwardly measured by the gyroscopes in the IMU and the vehicle pose (position and orientation) is obtained using the LIDAR sensor along with a simultaneous localization and mapping (SLAM) algorithm, publicly available through the Hector mapping package [Kohlbrecher et al., 2011].

From these measurements, we estimate the lateral velocity v using an Extended Kalman Filter, proposed in [Moore and Stouch, 2015]. The filter considers a planar movement and combines the wheel odometry information, the IMU's linear acceleration and angular velocity measurements, and the vehicle pose, outputted by the SLAM algorithm.

6.4.3 Experimental identification

The tests were performed on an unpolished ceramic tile surface with empirically estimated friction coefficient $\mu_i \approx 0.4$. The vehicle physical parameters required in this work are listed in table 6.1.

Table 6.1. List of the vehicle's physical parameters.

Symbol	Parameter name	Value
m	Vehicle mass	17.11 kg
a	Distance from CG to front axle	0.30 m
b	Distance from CG to rear axle	0.27 m
μ_i	Friction coefficient	0.4

The steering angle follows the chirp signal in an open-loop command. The experiment is repeated a number of times, varying the wave amplitude and longitudinal speed. A small fraction of the executed input, used for validation, is shown in Figure 6.3. The wave starts with an initial frequency of 1 Hz and ends with 6 Hz.

Note that the imperfections of the sine wave are due to the experimental setup nature. The steering angle is transmitted through a DC motor equipped with a low-level position controller. Therefore, it follows the steering system dynamics.

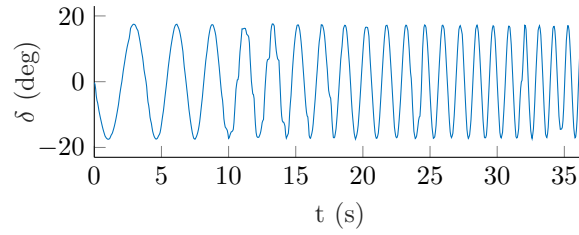


Figure 6.3. Steering angle following the swept sine. The first half-wave period is discarded due to initial measurement noises.

The proposed optimization problem is then solved via Matlab/Simulink in an off-board computer. There are many available algorithms that can be employed to solve the nonlinear constrained multivariable function (6.7), we have chosen an interior-point method using the builtin “fmincon” function from Matlab.

The weighting factors are chosen with respect to the magnitude of the corresponding residuals. Following an empirically trial and error approach, we designated $\lambda_1 = 3$, $\lambda_2 = 1$, $\lambda_3 = 1 \times 10^{-7}$ and $\lambda_4 = 2 \times 10^{-3}$, expressed each in such SI unit to make cost (6.7) dimensionless. The optimum estimated parameters obtained are

$$\begin{aligned}\hat{C}_\alpha &= 94.75 \text{ N}, \\ \hat{I}_z &= 1.64 \text{ kg/m}^2.\end{aligned}\tag{6.8}$$

Naturally, to validate the estimation, we compare the system’s simulated and measured responses. The simulation is carried out using the identified values \hat{C}_α and \hat{I}_z along with the vehicle model, described in Section 6.3.

6.4.4 Validation

We first analyze the identified model considering the open-loop swept sine input of Figure 6.3. The vehicle is set with a constant longitudinal velocity of 0.25 m/s. The results are shown in Figure 6.4.

It is notable the strong agreement between the measured and simulated vehicle states. The major discrepancy is observed in the lateral velocity v , mostly noticed during the transient responses when excited by high frequencies. Despite that, the states are in phase and the response time between both signals is consistent.

Now we wish to compare the estimated response with a practical maneuver. The experiment is conducted with a constant longitudinal speed of 0.4 m/s and setting the desired yaw rates with magnitudes of 0.2 and -0.2 rad/s. This results in a maneuver where two constant curvature radius are achieved with opposite directions. The performed trajectory and the commanded steering angle are shown in Figure 6.5.

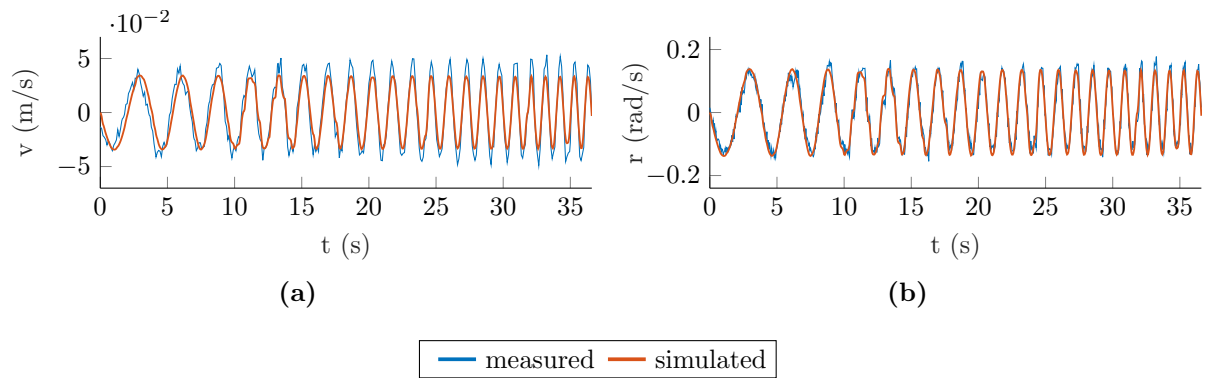


Figure 6.4. Comparison between lateral (a) and angular (b) velocities for the sinusoidal steering angle input.

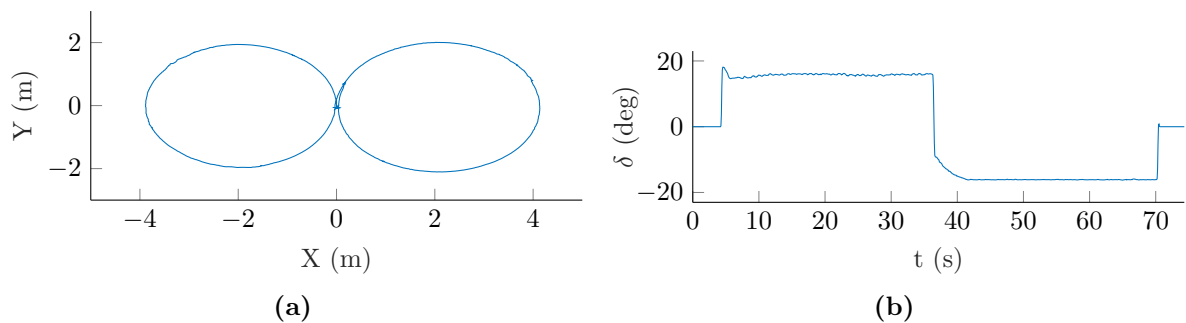


Figure 6.5. Trajectory of the proposed maneuver (a) and commanded steering angle (b).

The vehicle lateral states are shown in Figure 6.6. Note that v cannot be measured directly. As discussed, it must be filtered and the signal-noise ratio is associated with the noise exposure of our measurements. Despite unfavorable noise in v , the level of accuracy required to define whether the simulated response agrees with the estimated v is sufficient and satisfactory.

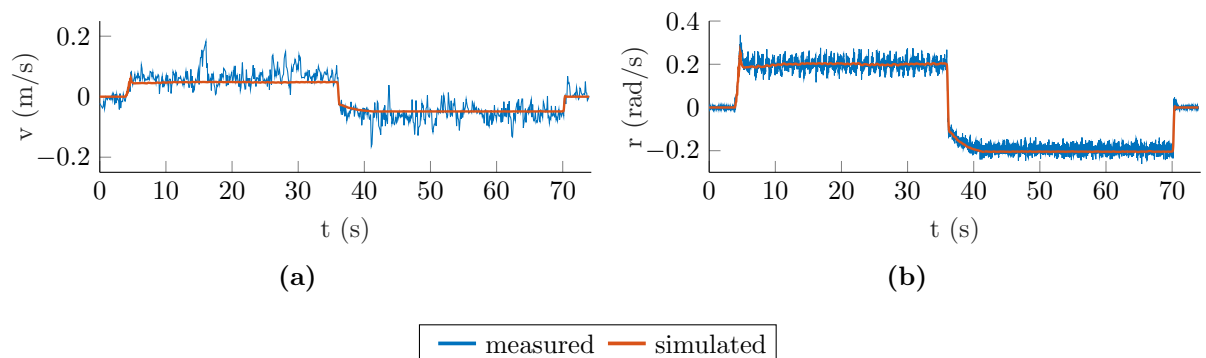


Figure 6.6. In (a) lateral velocity and (b) angular velocity.

6.4.5 Systematic investigation

To be able to confidently claim that the model properly represents the vehicle lateral motion, a comparison is presented in a systematic format. A standardized set of experiments is performed to confirm that the values obtained by simulating the vehicle match those acquired from the real evaluation.

From Figure 6.7, each experiment is conducted with a constant longitudinal speed, ranging from 0.3 to 0.7 m/s, and with four levels of steering angle excitation, -5, -10, -15, and -20 degrees. The steering pattern is time-dependent and the changes occur at successive 10 seconds time intervals.

In comparing the model to data, the results in Figure 6.7 provide a clear overview of accuracy. The results are systematic, sustained, repeatable, and show consistent deviation between measured and simulated signals. We can, therefore, confidently use the model for further analysis and control purposes.

Note that, for each 10-second interval, the vehicle operates in a steady-state condition, characterized by the constant regime. For the noisy data, the equilibrium condition can be quantified through the signal average of the corresponding segment. Thereby, the simulated and measured steady condition for each interval, as well as their absolute deviation (error), are reported in Table 6.2.

Table 6.2. Simulated (sim.) and real equilibrium points as well as their absolute difference (error) for each 10 seconds segment (T1 to T4) of the scenarios presented in Figure 6.7.

u_0 (m/s)		T1 (0 to 10 s)			T2 (10 to 20 s)			T3 (20 to 30 s)			T4 (30 to 40 s)		
		state	sim.	real	error	sim.	real	error	sim.	real	error	sim.	real
0.3	v	-0.012	-0.006	0.006	-0.023	-0.017	0.006	-0.036	-0.034	0.002	-0.053	-0.041	0.012
	r	-0.044	-0.046	0.002	-0.087	-0.082	0.005	-0.135	-0.133	0.002	-0.200	-0.191	0.009
0.4	v	-0.015	-0.008	0.008	-0.033	-0.021	0.012	-0.048	-0.045	0.003	-0.072	-0.071	0.001
	r	-0.058	-0.057	0.001	-0.126	-0.121	0.005	-0.183	-0.194	0.011	-0.272	-0.266	0.007
0.5	v	-0.019	-0.015	0.004	-0.040	-0.033	0.007	-0.063	-0.055	0.008	-0.088	-0.081	0.007
	r	-0.073	-0.075	0.003	-0.155	-0.153	0.001	-0.242	-0.253	0.011	-0.340	-0.339	0.001
0.6	v	-0.024	-0.010	0.015	-0.044	-0.044	0.001	-0.067	-0.081	0.014	-0.112	-0.112	0.000
	r	-0.096	-0.094	0.002	-0.174	-0.179	0.005	-0.262	-0.260	0.002	-0.439	-0.426	0.013
0.7	v	-0.029	-0.018	0.012	-0.051	-0.042	0.009	-0.077	-0.087	0.010	-0.120	-0.119	0.001
	r	-0.118	-0.115	0.003	-0.205	-0.197	0.007	-0.309	-0.303	0.006	-0.480	-0.473	0.007

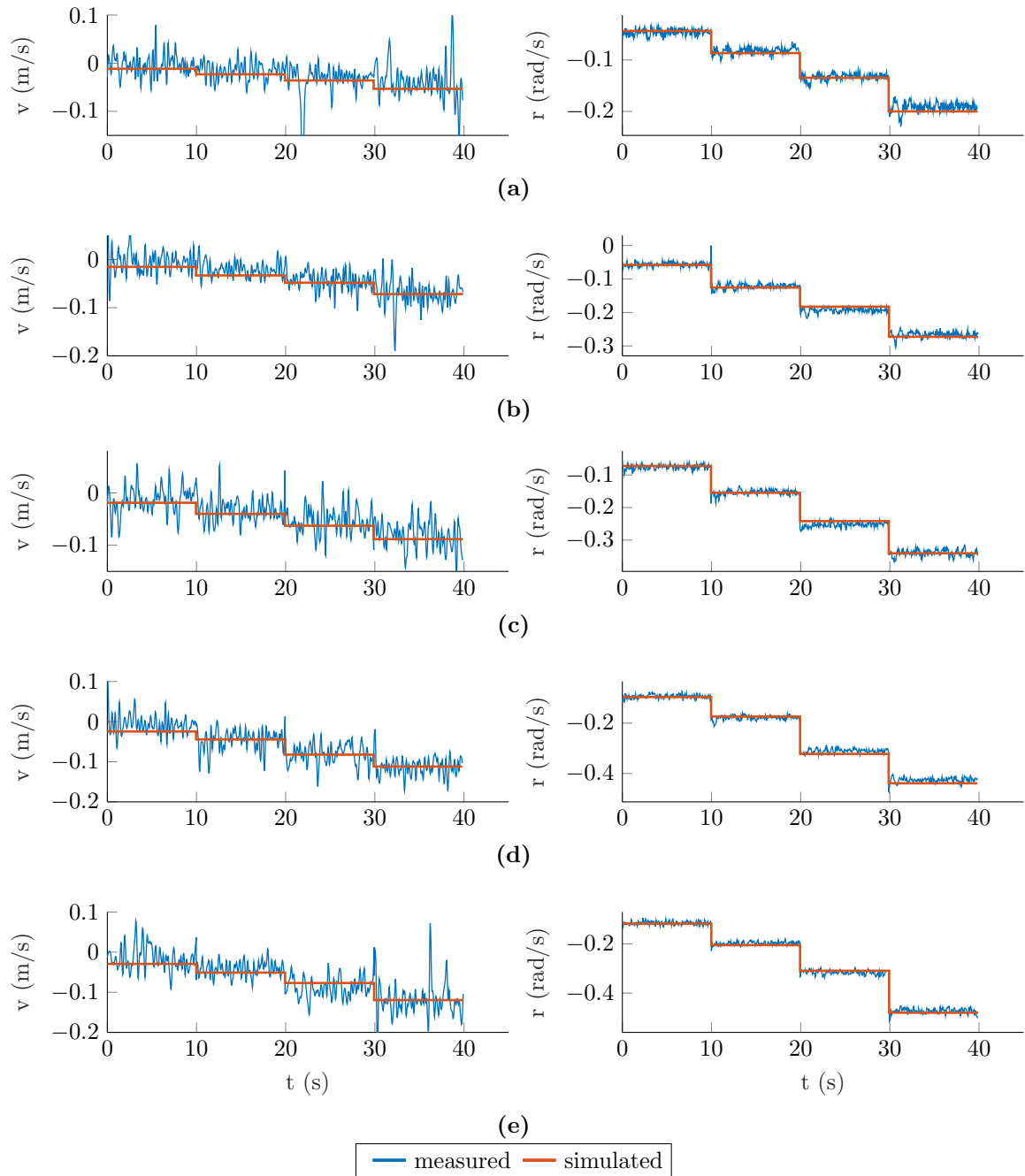


Figure 6.7. Set of experiments. The steering angle pattern is time-dependent fixed to the corresponding values: -5 , -10 , -15 , and -20 degrees. Longitudinal velocity is (a) 0.3 m/s, (b) 0.4 m/s, (c) 0.5 m/s, (d) 0.6 m/s, and (e) 0.7 m/s.

6.5 Stability Analysis

The findings presented in the preceding section lead to an important reflection on the vehicle equilibrium analysis: the steady-state conditions. For a given input, the steady-state conditions are related to the vehicle equilibrium points.

Given the nonlinear system (6.1) and its general form $\dot{x} = f(x, u)$, the system's equilibrium condition occurs at x_{eq} and the corresponding input values u_{eq} such that the state derivatives of the system are all zero, that is, $f(x_{eq}, u_{eq}) = 0$.

The bicycle model has only the steering angle as input. From a modeling standpoint, this control input cannot accelerate the vehicle in an arbitrary direction of the state space, meaning that the system is underactuated. Thus, in accordance with the mathematical model, steady-state conditions are only possible at certain locations in the state space [Khalil, 2002].

The study of these achievable equilibrium conditions reveals properties that have clear implications for stability and control designs. They provide physical understanding into nonlinear system dynamics and exhibit stability properties that have been used for different control purposes, such as for drift equilibria control [Voser et al., 2010, Cordeiro, 2017], basis of observers [Cordeiro et al., 2017], augmenting a vehicle's open-loop dynamics through steering and braking [Bobier-Tiu et al., 2018b], and for estimating and enlarging the domain of attraction [Masouleh and Limebeer, 2017, Ribeiro et al., 2020].

Assuming that our vehicle model, using the estimated parameters, correctly describes the vehicle behavior, we can search for the vehicle's equilibrium points (EP). The equilibrium points of the bicycle model are characterized by zero lateral and angular accelerations. Thus, with $\dot{v} = \dot{r} = 0$, the differential equations given in (6.1) are reduced to:

$$\dot{v} = \frac{F_{yf} \cos \delta_{eq} + F_{yr}}{m} - r_{eq} u_0 = f_v(v_{eq}, r_{eq}, \delta_{eq}) = 0, \quad (6.9)$$

$$\dot{r} = \frac{aF_{yf} \cos \delta_{eq} - bF_{yr}}{I_z} = f_r(v_{eq}, r_{eq}, \delta_{eq}) = 0. \quad (6.10)$$

Note that the lateral forces F_{yi} are also functions of the desired quantities v_{eq} , r_{eq} , δ_{eq} and u_0 . Constraining the values of δ_{eq} and u_0 , the system of equations (6.9) and (6.10) becomes a system of two equations and two unknowns, v_{eq} and r_{eq} , that can be obtained numerically.

A gradient-based algorithm is used to search for the desired points. The numerical procedure consists of executing the optimization algorithm from different starting points, using a uniform distribution.

By repeating the search for a wide range of steering angle values, it is possible to obtain the steady-state points for a driving condition. Figure 6.8 shows the EP as a function of

the steering angle that varies from -20 to $+20$ degrees with an increment of 1 degree. The results are also shown for three levels of longitudinal velocity.

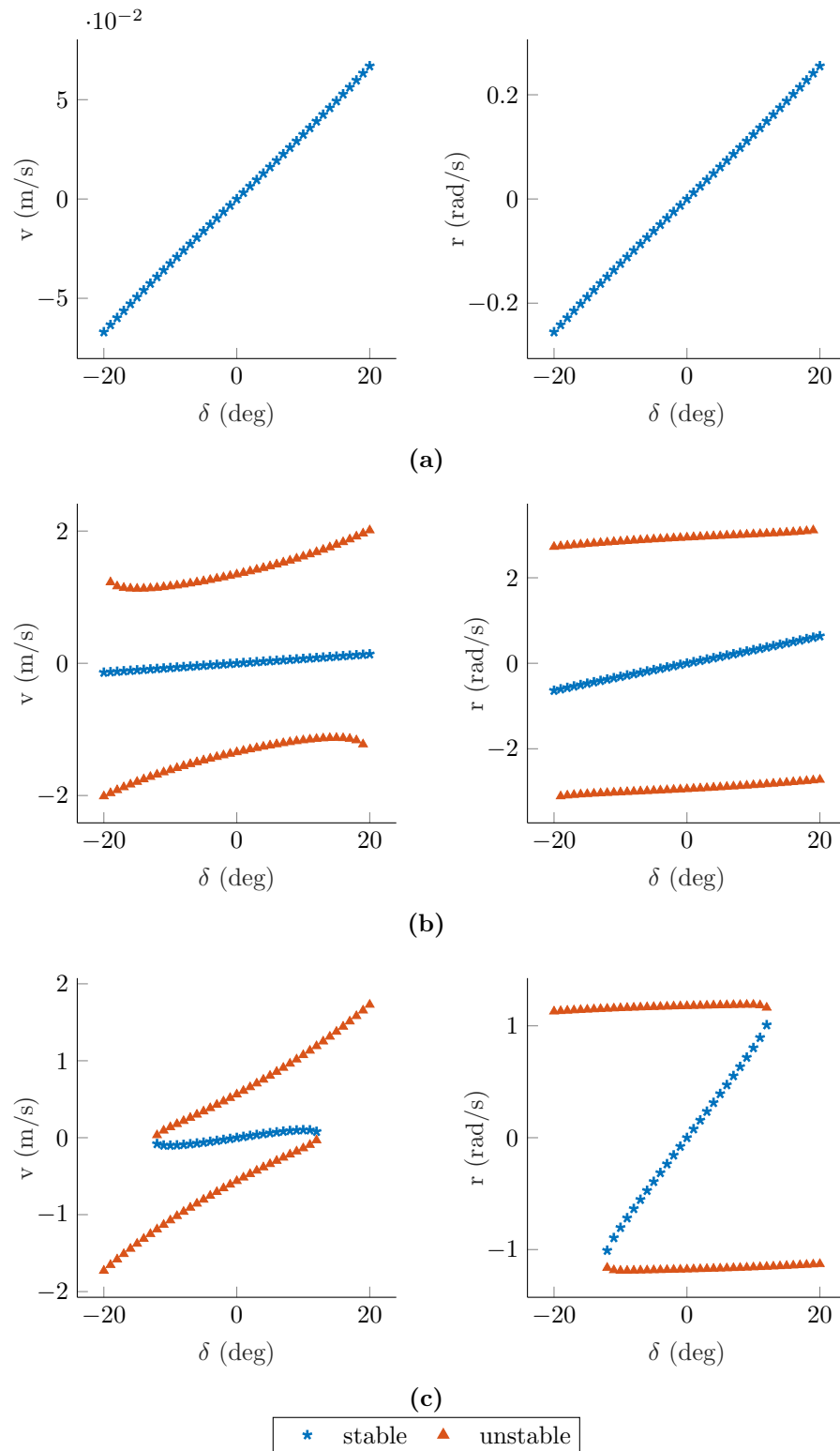


Figure 6.8. Equilibrium points considering longitudinal velocities u_0 of (a) 0.4 m/s, (b) 1.0 m/s, and (c) 2.5 m/s.

An eigenvalue analysis of the system's linearization is employed to verify the stability

condition for each equilibrium point. It is evident that the bicycle model exhibits two distinct classes of equilibria, stable and unstable ones. The family of EP shown as orange triangles presents comparatively large values of lateral velocity v_{eq} . For these points, the vehicle is said to be drifting. This is characterized by saturated tire forces, implying in an unstable equilibrium point.

In contrast, the stable EP, shown as blue stars, is evidenced by a small v_{eq} and the appearance of a linear relationship between δ_{eq} with quantities v_{eq} and r_{eq} . They correspond to a typical cornering performed in daily driving conditions. In this case, the vehicle is turning in the same direction as it is steered. In a drift condition, the handling characteristic known as countersteering is observed, recognized when the vehicle is steered to the opposite direction of the turn [Edelmann and Plöchl, 2009]. In agreement with the findings of [Ono et al., 1998], the unstable points are a result of a bifurcation in the system dynamics, heavily dependent on the tire force saturation.

Also, from Figure 6.8, no unstable points are verified for low longitudinal velocities. On the other hand, with $u_0 = 2.5$ m/s, no stable points are verified for absolute δ_{eq} greater than 12° . This means that, for $\delta_{eq} > 12^\circ$, the steady condition can only be achieved with drift.

In recent literature, the motivation of understanding and controlling the vehicle in drifting consists of exploring the new allowable window of operating conditions that would otherwise be infeasible [Hindiyeh, 2013]. Within this work, however, as a first validation of the scaled vehicle architecture, the most important behavior aspects and control properties will be investigated under a stable regime, i.e., considering only the stable equilibrium points as viable conditions.

6.5.1 Sensitivity analysis of the stable equilibrium points

When performing a maneuver, the vehicle can experience variations in longitudinal velocity. Moreover, the available friction coefficient may differ from the expected value or even change during the journey. These are two important parameters that confer meaningful behavior properties in the vehicle steady-state response.

To identify the parameter whose variation has the most impact on the vehicle lateral states, we perform a sensitivity analysis. Particularly, this characterization will be focused on the stable equilibrium points (blue segments) of Figure 6.8b, achieved with longitudinal velocity $u_0 = 1$ m/s.

Figures 6.9a and 6.9b show the effect of varying the model parameters u_0 and μ_i , respectively. For each one, a variation of $\pm 20\%$ from their nominal values are considered.

Lateral states v and r increase noticeably as the magnitude of u_0 increases. The opposite is also true, when longitudinal velocity decreases, a decrement in lateral excitation is detected. On the other hand, we can see that fluctuations around the available μ_i do

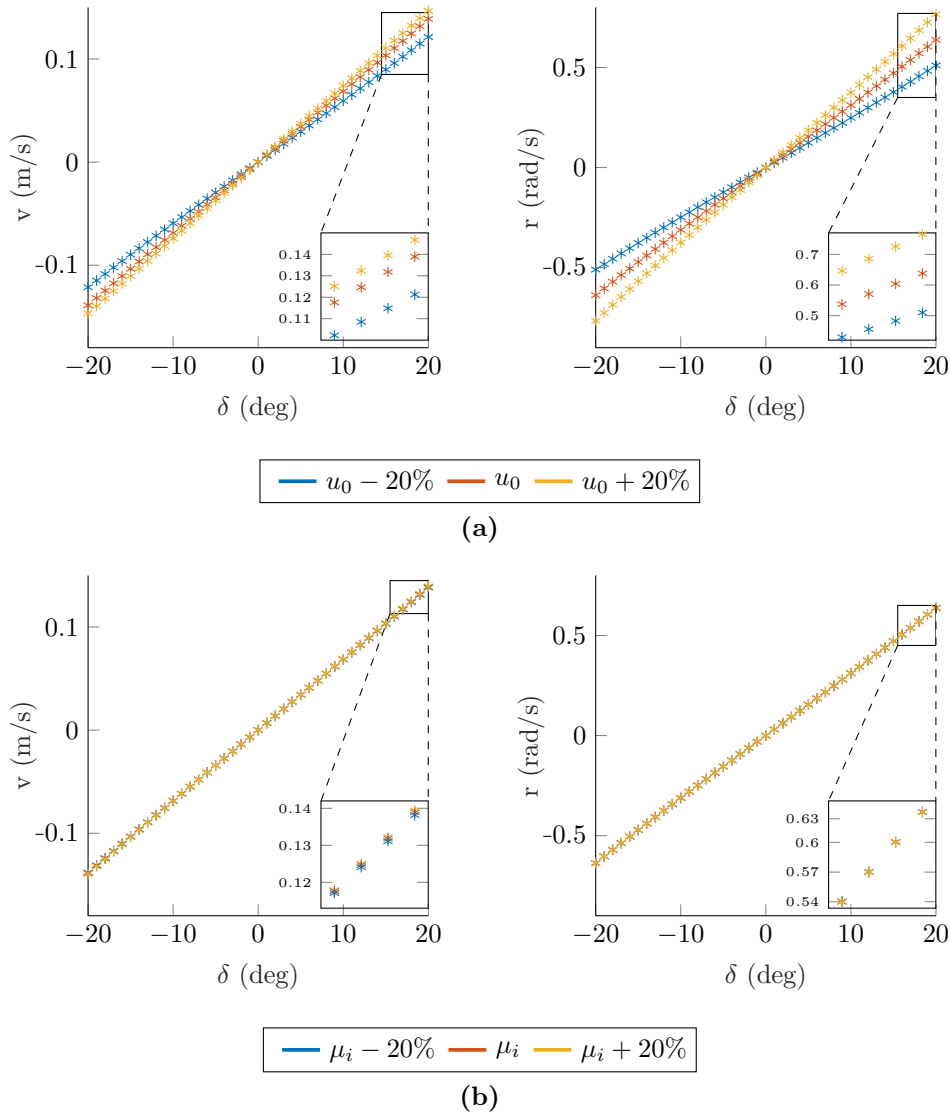


Figure 6.9. Effect of changing the standard deviation of (a) longitudinal velocity and (b) friction coefficient.

not lead to a significant variation in the EP. The reason is that the stable points are characterized by handling regimes such that tire force saturation has not been attained, the tire mainly operates in its linear region.

According to the tire force model (6.3), μ_i act on the threshold needed to reach the saturation condition. For the stable EP, the maximum achievable tire lateral force has not yet been reached. This allows an error margin in μ_i without affecting the operation of the stable points, which explains the insensitivity to small variations in friction. In contrast, when analyzing the unstable points, these properties are not verified [Voser et al., 2010].

The above discussion indicates that designs responsible to maintain the vehicle near its stable equilibrium point may not degrade substantially when the exact knowledge of surface conditions is not available. On the other hand, it is more important to correctly measure the longitudinal speed so that predictions of the theoretical model precisely

coincide with the measured response.

6.6 Experimental Validation

Now that the vehicle characterization is complete, we move forward to the SOS approach. This section, therefore, is devoted to the SOS control experimental analysis using the vehicle platform to validate the control design. The validation is proposed through a closed-loop scheme that considers four transitions among stable equilibrium points. For each of them, a control law is computed using the SOS theory. To simplify the design and the experimental evaluation, we consider only the steering angle input.

The polynomial vehicle model is assembled using the rational polynomial approximation. The RoA estimation and control synthesis are performed as described in Chapter 5. All vehicle parameters necessary for the analysis are listed in Table 6.3.

Table 6.3. List of physical parameters.

Symbol	Parameter name	Value
m	Vehicle mass	17.11 kg
a	Distance from CG to front axle	0.30 m
b	Distance from CG to rear axle	0.27 m
μ_i	Friction coefficient	0.4
C_α	Cornering stiffness	94.75 N
I_z	Yaw moment of inertia	1.64 kg/m ²
δ_{max}	Maximum steering angle	23 deg

By evaluating Algorithm 1 and 2, we achieve the results presented in Figures 6.10 and 6.11, respectively. The estimated RoA of the vehicle in study is presented for a series of conditions. In these cases, longitudinal velocity is $u_0 = 1.5$ m/s and the steering angle is set at three levels of excitation: 0, -5, and -10 degrees.

The results are similar to those presented in the previous chapter. Some characteristics are clearly analogous: the phase portrait have a similar format; the estimation is improved for high-order Lyapunov functions; and, as we increase the steering angle, the estimation accuracy is reduced due to the asymmetric gradient. Moreover, the closed-loop analysis shows that the control law indeed expands the RoA, stabilizing a small portion of the plane. From these figures we confirm that the model is assembled correctly and the synthesis is evaluated properly.

As mentioned, for the experimental evaluation, we consider four transitions among equilibrium points. For this purpose, we arbitrarily chose the points presented in Table 6.4.

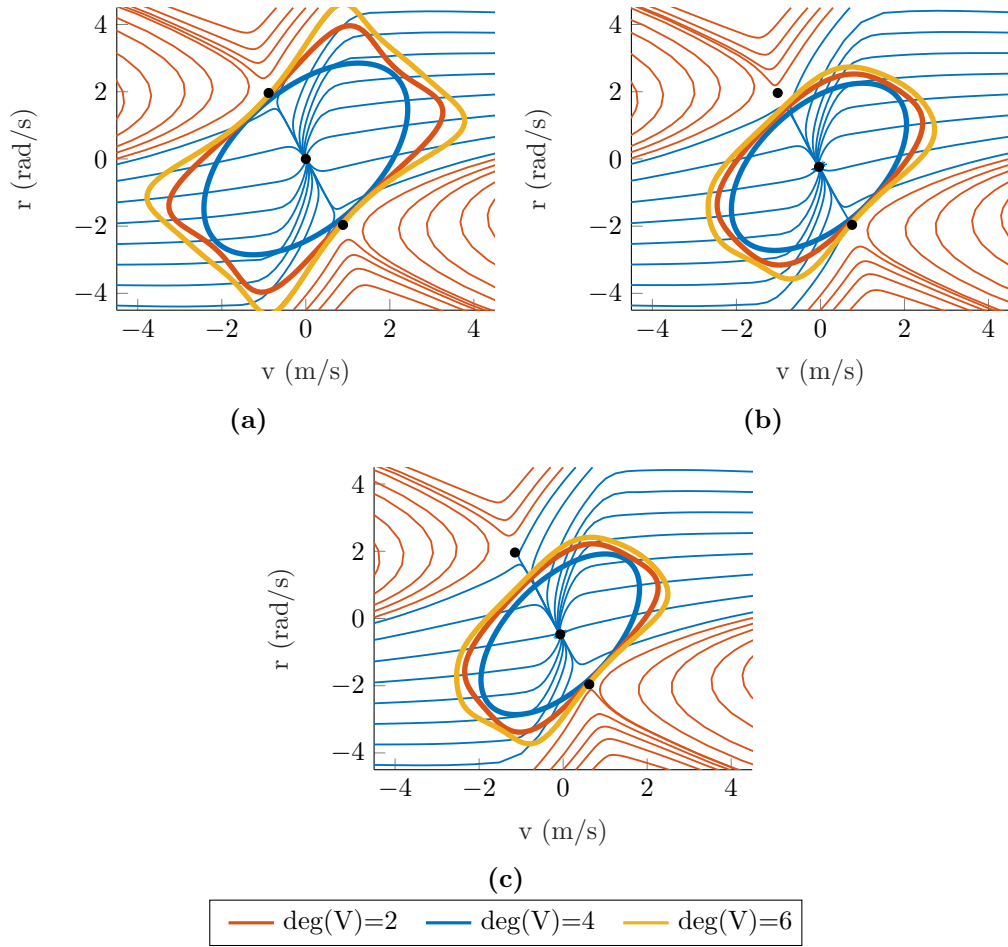


Figure 6.10. Estimated RoA. Steering angle is set to (a) $\delta = 0$, (b) $\delta = -5$, and (c) $\delta = -10$ degrees.

Observe that, for each selected pair u_0 and δ_{eq} , there is a single computed value of v_{eq} and r_{eq} that characterize the stable EP. The experiment is divided into four time-dependent segments, T1, ..., T4, individually associated to v_{eq} and r_{eq} that are the instantaneous goal point.

Table 6.4. Theoretical stable equilibrium points calculated from the bicycle model.

Segment	u_0 (m/s)	δ_{eq} (deg)	v_{eq} (m/s)	r_{eq} (rad/s)
T1	0.6	-12.00	-0.0554	-0.2212
T2	1.2	-17.50	-0.1240	-0.6528
T3	0.4	-15.00	-0.0481	-0.1840
T4	0.9	-13.50	-0.0846	-0.3750

For each segment T_i , a respective control law must be computed. For a more elaborate and comprehensive validation, we designed first- and third-orders polynomial controllers.

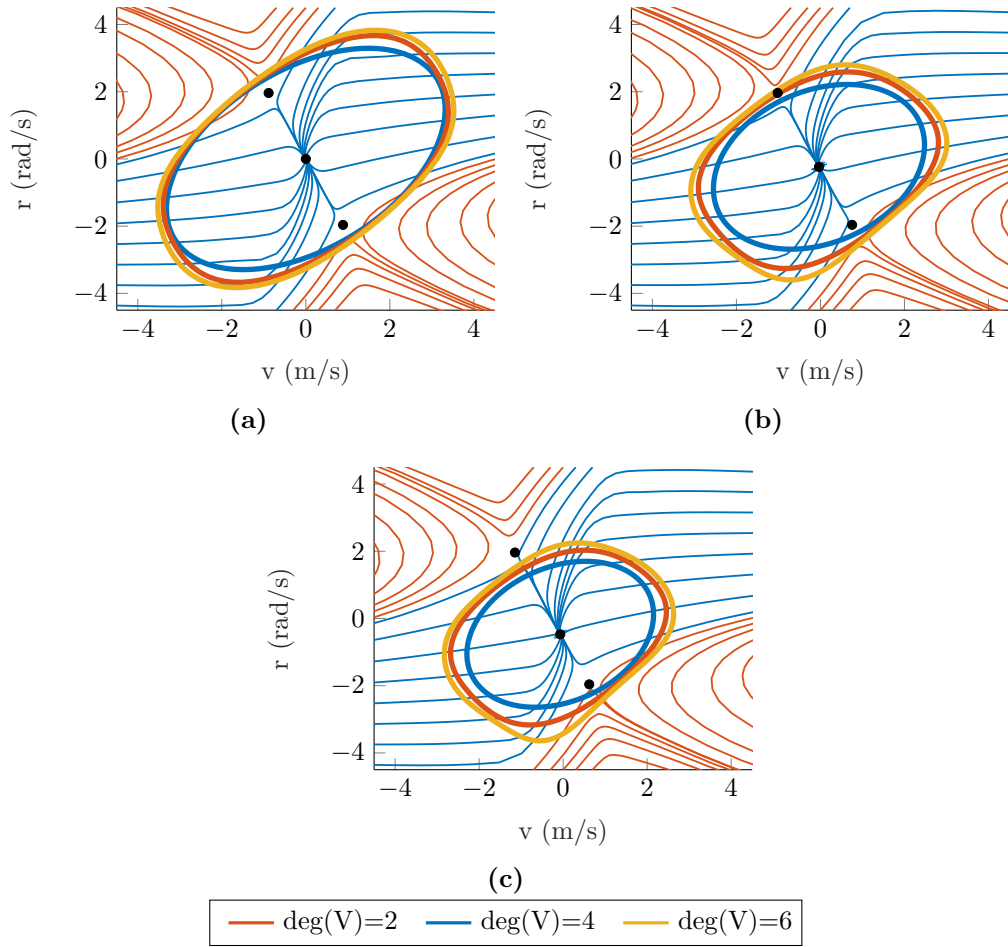


Figure 6.11. Estimated RoA of the closed-loop system. Steering angle is set to (a) $\delta = 0$, (b) $\delta = -5$, and (c) $\delta = -10$ degrees.

The first-order computed gains are

$$\begin{aligned}
 K_{1,T1} &= 0.0563\bar{v} + 0.1577\bar{r}, \\
 K_{1,T2} &= 0.0761\bar{v} + 0.1652\bar{r}, \\
 K_{1,T3} &= 0.0578\bar{v} + 0.1009\bar{r}, \\
 K_{1,T4} &= 0.0350\bar{v} + 0.1221\bar{r},
 \end{aligned} \tag{6.11}$$

and third-order controllers

$$\begin{aligned}
 K_{3,T1} &= 0.0150\bar{v}^3 - 0.0435\bar{v}^2\bar{r} - 0.0005\bar{v}^2 + 0.1637\bar{v}\bar{r}^2 + 0.0070\bar{v}\bar{r} + 0.2476\bar{v} + \\
 &\quad + 0.0084\bar{r}^3 - 0.0040\bar{r}^2 + 0.1574\bar{r}, \\
 K_{3,T2} &= 0.0115\bar{v}^3 - 0.0417\bar{v}^2\bar{r} - 0.0003\bar{v}^2 + 0.0891\bar{v}\bar{r}^2 + 0.0126\bar{v}\bar{r} + 0.2181\bar{v} + \\
 &\quad + 0.0052\bar{r}^3 - 0.0001\bar{r}^2 + 0.2246\bar{r}, \\
 K_{3,T3} &= 0.0128\bar{v}^3 - 0.0478\bar{v}^2\bar{r} - 0.0036\bar{v}^2 + 0.1197\bar{v}\bar{r}^2 + 0.0095\bar{v}\bar{r} + 0.2605\bar{v} -
 \end{aligned} \tag{6.12}$$

$$\begin{aligned}
& -0.0023\bar{r}^3 - 0.0006\bar{r}^2 + 0.2552\bar{r}, \\
K_{3,T_4} = & 0.0798\bar{v}^3 - 0.0825\bar{v}^2\bar{r} - 0.0010\bar{v}^2 + 0.1089\bar{v}\bar{r}^2 + 0.0101\bar{v}\bar{r} + 0.2623\bar{v} + \\
& + 0.0061\bar{r}^3 - 0.0045\bar{r}^2 + 0.3730\bar{r}.
\end{aligned}$$

Each segment T_i is associated to a control law, where K_{1,T_i} and K_{3,T_i} are the first- and third-order polynomials, respectively. Variables \bar{v} and \bar{r} are expressed in their respective coordinate system, i.e., $\bar{v} = v - v_{eq}$ and $\bar{r} = r - r_{eq}$. For the experimental evaluation, the transition among controllers is deliberately driven by time.

Interestingly, the coefficients of the quadratic terms in (6.12) are noticeably smaller than their first- and third-order pairs. Quadratic terms always produce a positive contribution to the control effort, therefore, it is intuitive to reduce the importance of such terms due to the asymmetry that it generate. This is also the reason that we did not search for a second-order polynomial controller.

As it can be seen in Figure 6.12, the experimental evaluation results in a maneuver with four radii of curvature. This is obviously true since the desired equilibrium conditions of each segment are appropriately distinct. Although the references are the same for both controllers, a slight difference is noted in the performed trajectory. For the third-order controllers (Figure 6.12b), the radius of curvature is slightly greater, which resulted in steeper curves.

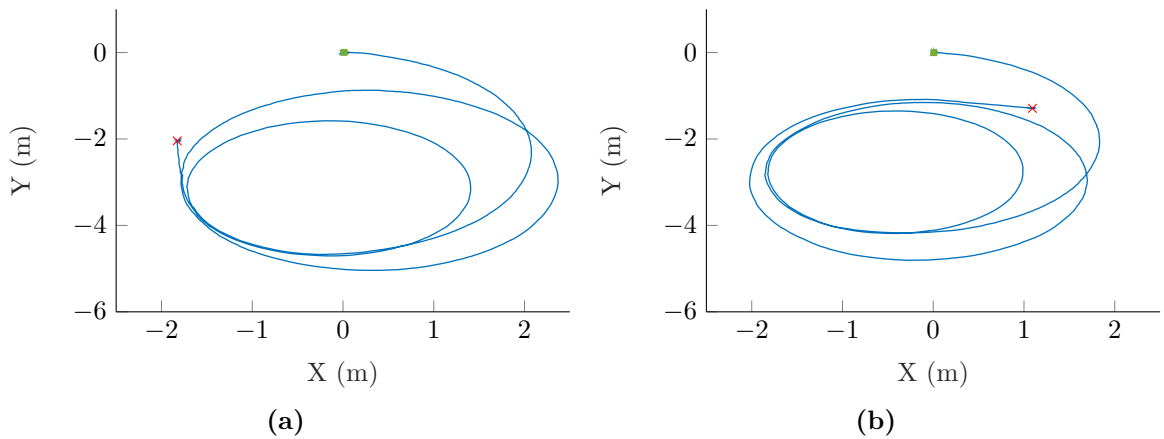


Figure 6.12. Performed trajectory. The results are obtained using (a) first- and (b) third-orders controllers. Green and red marks are the initial and ending positions.

In Figure 6.13, we show the measured longitudinal velocity. The response properly follows the desired values, which are listed in Table 6.4. Longitudinal velocity is impelled by the motor's drive that regulates the wheels velocity. It is not related to the SOS controller, therefore, much the same response is expected between them. Also note that segments T_1 to T_4 are discriminated over time.

The desired and measured lateral response, v and r , are shown in Figure 6.14. The

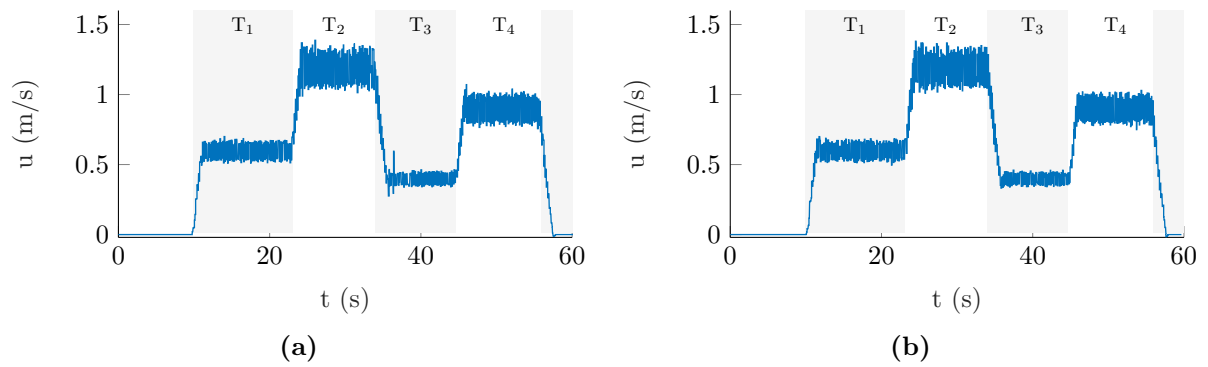


Figure 6.13. Measured longitudinal velocity for the closed-loop maneuver using (a) first- and (b) third-orders controllers.

accordance and also errors between the reference and measured response are evident.

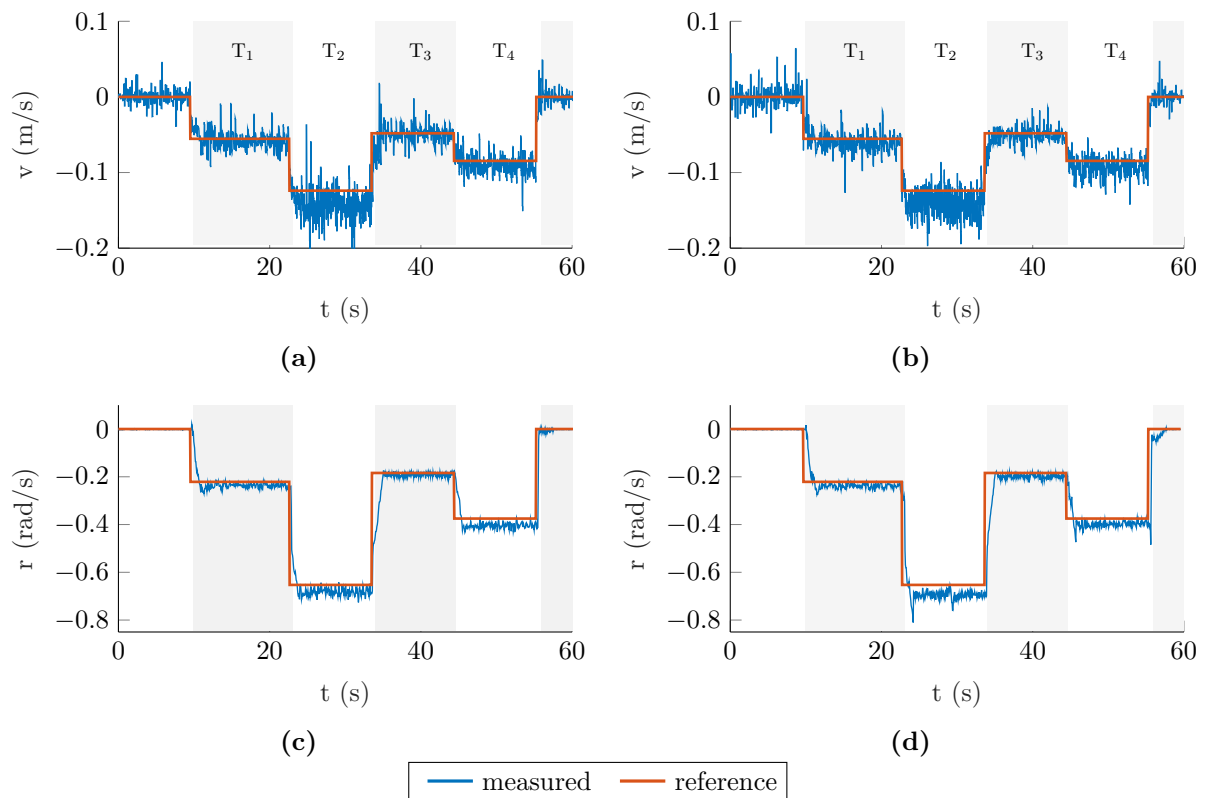


Figure 6.14. Desired and achieved equilibrium conditions. Left and right figures are obtained using the first and third order controllers, respectively.

Finally, in Figure 6.15 we show the commanded steering angle. A strong actuation is observed for the third-order controller, which is the reason for the steeper curves discussed above. For controllers $K_{3,Ti}$, in addition to the contribution from the elements of second and third orders, their linear coefficients are also remarkably greater than the coefficients of $K_{1,Ti}$. This is the reason for the noisy signal as well as the large effort observed between

transitions.

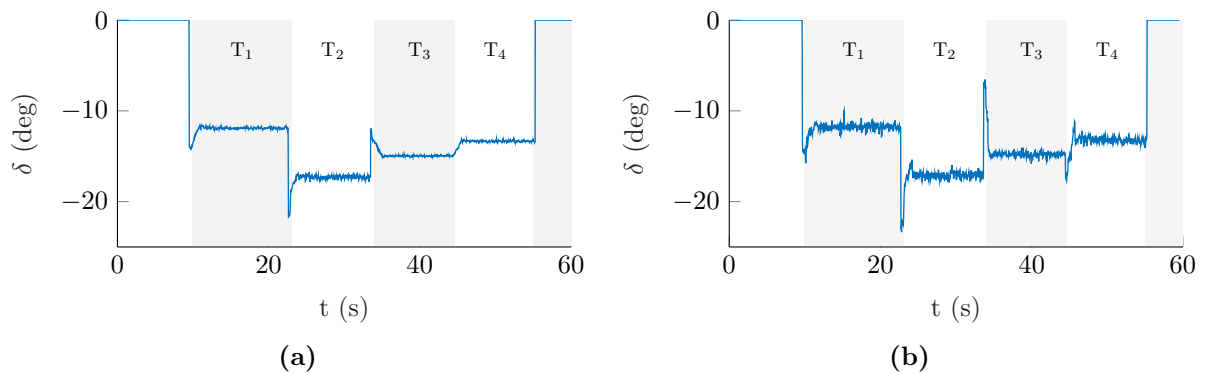


Figure 6.15. Commanded steering angle using the (a) first- and (b) third-order controllers.

The above discussion is evident by examining Figure 6.16. The continuous curves are the level sets of the third-order controller. Similarly, dashed lines stand for the level sets of the first-order controller. The figure shows the values of \bar{v} and \bar{r} necessary to provide a given input.

Take, for example, the 15 degrees steering correction (brown curve). The perturbations \bar{x} necessary to provide a steering angle correction of 15 degrees are considerably smaller for K_3 than K_1 . This shows that controller K_3 can provide high commanded values with relatively small errors.

In Figure 6.16 we have shown the control curves of segment T_1 , nonetheless, similar S-shaped curves are also observed for segments T_2 to T_4 .

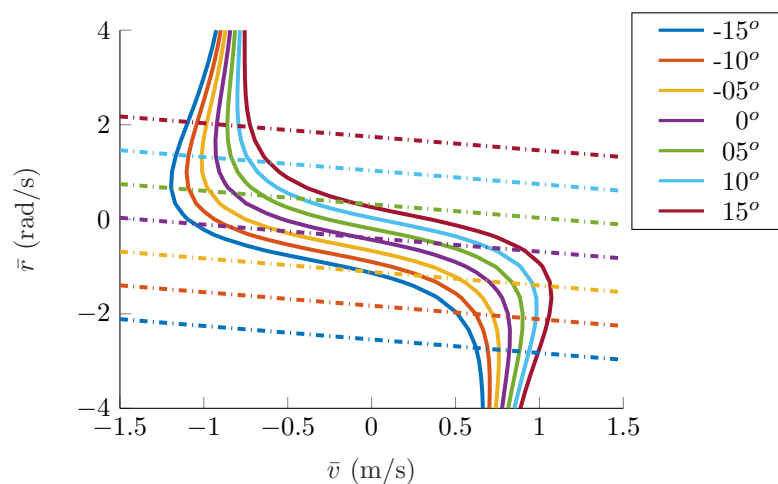


Figure 6.16. Level sets of the polynomial control law. Dashed and continuous lines stand for the first- and third-orders controllers, respectively.

The expected and obtained steady-state values are presented in Table 2. The achieved values are computed through the average of the signals of each segment. We consider only

the stationary regime by discarding the transient response from the calculation.

Table 6.5. Expected and reached values using the first- and third-order controllers.

Segment	Values	delta (deg)	States	
			v (m/s)	r (rad/s)
T1	Expected	-12.00	-0.0554	-0.2212
	Reached K1	-11.86	-0.0573	-0.2386
	Reached K3	-11.68	-0.0618	-0.2386
T2	Expected	-17.50	-0.1240	-0.6528
	Reached K1	-17.04	-0.1441	-0.6821
	Reached K3	-16.78	-0.1381	-0.6950
T3	Expected	-15.00	-0.0481	-0.1840
	Reached K1	-14.78	-0.0491	-0.1914
	Reached K3	-14.74	-0.0481	-0.1840
T4	Expected	-13.50	-0.0846	-0.3750
	Reached K1	-13.28	-0.0903	-0.4042
	Reached K3	-12.88	-0.0921	-0.3989

Although we did not force the vehicle to reach the limits of stability, we were able to show that the control design based on the sum-of-squares programming is a valid tool. It is clear that the complexity of the resultant control law grows with the polynomial order, which may result in abstract mathematical quantities, as in (6.12). The third-order polynomial is a counter-intuitive control function that progressed correctly in the proposed experiment.

6.7 Final Remarks

This section illustrates the use of a car-like 1:5-scale vehicle as a valid and reliable test-bed platform whose lateral dynamics are similar to those of a full-sized vehicle. The validation scheme is proposed by way of three model-based essential concepts, comprising an identification process, a stability analysis step, and an SOS control design.

The control validation is proposed through a closed-loop maneuver that considers four transitions among stable equilibrium points. The results show that the proposed SOS-based methodology can be used as a valid analysis and design tool for a real vehicle application.

The following publications were produced presenting the results of this chapter (Ribeiro, Fioravanti & de Paiva 2020) and (Ribeiro, Koyama, Moutinho, de Paiva & Fioravanti 2020):

-
- A. M. Ribeiro, A. R. Fioravanti, A. Moutinho and E. C. d. Paiva. Model-Based Approach for Cornering Stiffness and Yaw Moment of Inertia Estimation of a Scaled Electric Vehicle. In *XXIII Congresso Brasileiro de Automática (CBA 2020)*, Santa Maria - Brazil, November 23-26, 2020.
<https://doi.org/10.48011/asba.v2i1.1007>
 - A. M. Ribeiro, A. R. Fioravanti, A. Moutinho and E. C. d. Paiva. A comprehensive experimental validation of a scaled car-like vehicle: Lateral dynamics identification, stability analysis, and control application. *Control Engineering Practice*. Volume 116, 2021.
<https://doi.org/10.1016/j.conengprac.2021.104924>

7 Conclusion

In this thesis, we have shown how the sum-of-squares technique can be used to analyze the vehicle nonlinear system algorithmically. We investigated the region of attraction estimation and its further enlargement through a state feedback design while accounting for input saturation. Then, we explored a scaled electric vehicle which was used for experimental validation of the discussed tools.

Before closing, we will give a summary of the main results and developments presented in the previous chapters and discuss briefly recommendations for future research directions.

7.1 Summary

In this thesis, we have seen the following results:

- In Chapter 3, we reviewed the background material needed for problem formulation in the subsequent chapters. A brief outline of polynomial definitions, sum-of-squares polynomials, and the Positivstellensatz theorem are presented.
- In Chapter 4, we presented how the sum-of-squares and semidefinite programming were used for the analysis of nonlinear systems. In particular, we explored the region of attraction estimation and how it can be expanded through state feedback with input saturation. Our first results were brought with the SOS-based control design analysis for the class of non-affine in the input system. A Taylor approximation was proposed and the inclusion of a new step into the iterative algorithm is discussed. We finished by giving some examples for a better understanding.
- In Chapter 2, we inspected the existing tire and vehicle models used throughout this dissertation. It included multiple approaches to tire force modeling as well as three versions of the vehicle planar model.
- In Chapter 5, we considered the region of attraction estimation of the lateral dynamics of a nonlinear single-track vehicle model. The tire forces were approximated using rational functions that are shown to capture the nonlinearities of more complex tire curves remarkably better than polynomial functions. The chapter also addressed the

stabilization problem, the objective was to estimate the largest state-space region such that stability and input saturation can be guaranteed. The algorithm allows the region of attraction to be approximated by a level set of a Lyapunov function and the computation of polynomial state feedback control laws. It is shown that SOS programming techniques can be used to approximate the stability region without resorting to numerical integration. To conclude, a Monte-Carlo analysis is presented to show that the proposed SOS-based methodology can be used as a valid analysis and design tool.

- In Chapter 6, thorough characterization of a scaled electric vehicle is presented through identification, stability analysis, and SOS-based control design schemes. The estimation of unknown parameters was performed based on the analysis of the signal produced at the output of the platform when exciting the system by a given input signal. The obtained results led to a second important reflection that highlights meaningful vehicle behavior properties. The analysis section is then presented showing the characterization of the vehicle's operating conditions. Stable equilibrium points were classified and chosen as the desirable conditions for a given maneuver. Finally, the control scheme incorporated the above characteristics into its design. The SOS theory was employed to synthesize polynomial control laws that were experimentally validated using the vehicle platform. For each presented characterization, a wide set of experiments were carried out using the scaled vehicle platform. In all of them, a persistent agreement between expected and achieved response was obtained.

7.2 Future Research Directions

We would now like to mention a few pointers for future research. The SOS-based analysis and controller designed and successfully implemented in this dissertation provides a fundamental understanding of vehicle stability by means of Lyapunov's theorem. From this foundation, there are multiple guidelines for future research. Some of these directions continue to focus upon the region of attraction estimation for a more refined model, while others involve the control design enhancement and an in-depth experimental validation.

7.2.1 Inclusion of longitudinal and vertical dynamics and weight transfer

It was observed in Section 5.3.3 that load-transfer effects confer meaningful behavior properties that are important factors for stability. Nonetheless, the bicycle model employed in the study assumes lumped tires that reflect the effect of lateral weight transfer upon the net lateral force capability at the front and rear wheels. It does not capture the effect of

load transfer upon the individual wheels at an axle.

For a more precise investigation, these effects should be incorporated into the analysis through a model refinement. With a three-stated and four-wheel planar model, the wheels can be modeled individually and the coupling between the tire lateral and longitudinal forces can be considered. Nonetheless, analysis feasibility relies upon the resulting model being polynomial in its arguments.

The central effect of this improvement would be upon the force capability of each wheel. The yaw moment and steering angle authorities are only available through the attainable force at each wheel, which is better described by the improved model. Besides that, the bicycle model assumes a constant longitudinal velocity. In a more complete model, longitudinal speed should be written as an additional state such that the effect of variations around the trimmed condition is alleviated.

7.2.2 Regulation in unstable equilibrium conditions

The vehicle equilibrium conditions are characterized by one stable equilibrium point and a pair of unstable equilibria. The feature of strictly controlling the vehicle in these unstable points, i.e., intentionally drifting, considerably increases the range of allowable operating conditions that, otherwise, would not be possible.

The sum-of-squares programming technique could be extended to this closed-loop stabilization problem. It is often difficult to produce a perceptive understanding of the vehicle response under a control structure, such as predicting the combined effect of distinct inputs.

By using the SOS approach, it may be possible to produce closed-loop dynamics that are viable to manipulate. It should be possible to account for multiple inputs and, most importantly, estimate and expand the region of the state space that the drift controller is feasible.

7.2.3 Performance requirements

The performances of the control systems are not explicitly incorporated into the SOS control design. From a practical point of view, it is possible to obtain a balance between inputs by adjusting the saturation limits of the respective control signal. However, the author understands that these parameters must follow the physical limitations of the plant in the study.

One can consider an objective function that makes, for example, a compromise between state error and control energy efficiency, such as in the classic LQR. By means of additional steps into Algorithm 2 in Chapter 4, it should be possible to consider such performance criteria. It is worth mentioning that this is non-standard in the SOS-based synthesis

problem and would require a detailed and careful analysis.

7.2.4 Experimental validation

Although an experimental validation was presented in Chapter 6, the analysis did not take the vehicle to the limits of handling. One should run experiments that manage the vehicle to a region near the stability boundary. This scenario would test, and also attest, the stable region predicted by the theoretical analysis. Therefore, we highlight the need for more exhaustively experimental validation.

Bibliography

- J. Ackermann. Robust car steering by yaw rate control. In *29th IEEE Conference on Decision and Control*. IEEE, 1990. doi: 10.1109/cdc.1990.203981. URL <https://doi.org/10.1109/cdc.1990.203981>.
- A. A. Ahmadi and A. Majumdar. DSOS and SDSOS Optimization: More Tractable Alternatives to Sum of Squares and Semidefinite Optimization. *SIAM Journal on Applied Algebra and Geometry*, 3(2):193–230, Jan. 2019. ISSN 2470-6566. doi: 10.1137/18M118935X. URL <https://epubs.siam.org/doi/10.1137/18M118935X>.
- A. A. Aly, E.-S. Zeidan, A. Hamed, and F. Salem. An antilock-braking systems (ABS) control: A technical review. *Intelligent Control and Automation*, 02(03):186–195, 2011. doi: 10.4236/ica.2011.23023. URL <https://doi.org/10.4236/ica.2011.23023>.
- J. Anderson and A. Papachristodoulou. Advances in computational lyapunov analysis using sum-of-squares programming. *Discrete and Continuous Dynamical Systems - Series B*, 20(8):2361–2381, Aug. 2015. doi: 10.3934/dcdsb.2015.20.2361. URL <https://doi.org/10.3934/dcdsb.2015.20.2361>.
- A. Antunes, P. Outeiro, C. Cardeira, and P. Oliveira. Implementation and testing of a sideslip estimation for a formula student prototype. *Robotics and Autonomous Systems*, 115:83–89, May 2019. doi: 10.1016/j.robot.2019.01.018. URL <https://doi.org/10.1016/j.robot.2019.01.018>.
- M. Ataei, A. Khajepour, and S. Jeon. Reconfigurable integrated stability control for four- and three-wheeled urban vehicles with flexible combinations of actuation systems. *IEEE/ASME Transactions on Mechatronics*, 23(5):2031–2041, Oct. 2018. ISSN 1941-014X. doi: 10.1109/tmech.2018.2862924. URL <https://doi.org/10.1109/tmech.2018.2862924>.
- M. Ataei, A. Khajepour, and S. Jeon. Model predictive control for integrated lateral stability, traction/braking control, and rollover prevention of electric vehicles. *Vehicle System Dynamics*, 58(1):49–73, Mar. 2019. doi: 10.1080/00423114.2019.1585557. URL <https://doi.org/10.1080/00423114.2019.1585557>.

- F. Ballo, G. Previati, M. Gobbi, and G. Mastinu. Tire-rim interaction, a semi-analytical tire model. *Journal of Mechanical Design*, 140(4), Jan. 2018. doi: 10.1115/1.4038927. URL <https://doi.org/10.1115/1.4038927>.
- C. E. Beal and C. Boyd. Coupled lateral-longitudinal vehicle dynamics and control design with three-dimensional state portraits. *Vehicle System Dynamics*, 57(2):286–313, 2019. doi: 10.1080/00423114.2018.1467019. URL <https://doi.org/10.1080/00423114.2018.1467019>.
- K. Berntorp, P. Inani, R. Quirynen, and S. D. Cairano. Motion planning of autonomous road vehicles by particle filtering: Implementation and validation. In *2019 American Control Conference (ACC)*, pages 1382–1387. IEEE, July 2019. doi: 10.23919/acc.2019.8815309. URL <https://doi.org/10.23919/acc.2019.8815309>.
- C. G. Bobier-Tiu, C. E. Beal, J. C. Kegelman, R. Y. Hindiyeh, and J. C. Gerdes. Vehicle control synthesis using phase portraits of planar dynamics. *Vehicle System Dynamics*, 57(9):1318–1337, July 2018a. doi: 10.1080/00423114.2018.1502456. URL <https://doi.org/10.1080/00423114.2018.1502456>.
- C. G. Bobier-Tiu, C. E. Beal, J. C. Kegelman, R. Y. Hindiyeh, and J. C. Gerdes. Vehicle control synthesis using phase portraits of planar dynamics. *Vehicle System Dynamics*, 57(9):1318–1337, July 2018b.
- J. Bochnak, M. Coste, and M.-F. Roy. *Real Algebraic Geometry*. Springer, Berlin New York, 1998. ISBN 978-3-662-03718-8. URL <https://doi.org/10.1007/978-3-662-03718-8>.
- A. Bulsara, A. Raman, S. Kamarajugadda, M. Schmid, and V. N. Krovi. Obstacle avoidance using model predictive control: An implementation and validation study using scaled vehicles. In *SAE Technical Paper Series*, pages 1–8. SAE International, Apr. 2020. doi: 10.4271/2020-01-0109. URL <https://doi.org/10.4271/2020-01-0109>.
- A. Chakraborty, P. Seiler, and G. J. Balas. Nonlinear region of attraction analysis for flight control verification and validation. *Control Engineering Practice*, 19(4):335–345, apr 2011. doi: 10.1016/j.conengprac.2010.12.001. URL <https://doi.org/10.1016/j.conengprac.2010.12.001>.
- C. Chatzikomis, M. Zanchetta, P. Gruber, A. Sorniotti, B. Modic, T. Motaln, L. Blagotinssek, and G. Gotovac. An energy-efficient torque-vectoring algorithm for electric vehicles with multiple motors. *Mechanical Systems and Signal Processing*, 128:655–673, Aug. 2019. doi: 10.1016/j.ymsp.2019.03.012. URL <https://doi.org/10.1016/j.ymsp.2019.03.012>.

- C.-T. Chen. *Linear system theory and design*. Oxford University Press, Inc., 1998.
- M. Chen, Y. Tian, G. Fortino, J. Zhang, and I. Humar. Cognitive internet of vehicles. *Computer Communications*, 120:58–70, May 2018. ISSN 0140-3664. doi: 10.1016/j.comcom.2018.02.006. URL <http://www.sciencedirect.com/science/article/pii/S0140366417311015>.
- Y. Chen and J. J. Zhu. Car-like ground vehicle trajectory tracking by using trajectory linearization control. In D. Systems and C. Conference, editors, *Dynamic Systems and Control*, volume 2. American Society of Mechanical Engineers, Oct. 2017. doi: 10.1115/DSCC2017-5372. URL <https://doi.org/10.1115/DSCC2017-5372>. V002T21A014.
- Y.-J. Chen, M. Tanaka, K. Tanaka, and H. O. Wang. Stability analysis and region-of-attraction estimation using piecewise polynomial lyapunov functions: Polynomial fuzzy model approach. *IEEE Transactions on Fuzzy Systems*, 23(4):1314–1322, Aug. 2015. doi: 10.1109/tfuzz.2014.2347993. URL <https://doi.org/10.1109/tfuzz.2014.2347993>.
- G. Chesi. SMRSOFT: a matlab toolbox for optimization over polynomials and dynamical systems study via SOS programming, 2011a. URL <http://www.eee.hku.hk/~chesi>.
- G. Chesi. *Domain of attraction : analysis and control via SOS programming*. Springer, London, 2011b. ISBN 978-0-85729-959-8.
- R. A. Cordeiro, A. M. Ribeiro, J. R. Azinheira, A. C. Victorino, P. A. V. Ferreira, E. C. de Paiva, and S. S. Bueno. Road grades and tire forces estimation using two-stage extended kalman filter in a delayed interconnected cascade structure. In *2017 IEEE Intelligent Vehicles Symposium (IV)*, pages 115–120. IEEE, June 2017. doi: 10.1109/ivs.2017.7995707. URL <https://doi.org/10.1109/ivs.2017.7995707>.
- R. d. A. Cordeiro. *Estimation of Tire-Ground Interaction Forces in Four-Wheel Vehicles and their Influences during Maneuvers in Extreme Conditions*. PhD thesis, Universidade Estadual de Campinas, Sept. 2017. URL <http://repositorio.unicamp.br/jspui/handle/REPOSIP/330443>.
- T. Cunis, J.-P. Condomines, and L. Burlion. Sum-of-squares flight control synthesis for deep-stall recovery. *Journal of Guidance, Control, and Dynamics*, 43(8):1498–1511, Aug. 2020. doi: 10.2514/1.g004753. URL <https://doi.org/10.2514/1.g004753>.
- C. Depature, W. Lhomme, P. Sicard, A. Bouscayrol, and L. Boulon. Backstepping control of an electric vehicle with local control saturation. In *2017 IEEE Vehicle Power and Propulsion Conference (VPPC)*, pages 1–6. IEEE, Dec. 2017. doi: 10.1109/vppc.2017.8330916. URL <https://doi.org/10.1109/vppc.2017.8330916>.

- R. Drummond, G. Valmorbidia, and S. R. Duncan. Generalized absolute stability using lyapunov functions with relaxed positivity conditions. *IEEE Control Systems Letters*, 2(2):207–212, Apr. 2018. doi: 10.1109/lcsys.2017.2782747. URL <https://doi.org/10.1109/lcsys.2017.2782747>.
- L. E. Dubins. On curves of minimal length with a constraint on average curvature, and with prescribed initial and terminal positions and tangents. *American Journal of Mathematics*, 79(3):497, July 1957. doi: 10.2307/2372560. URL <https://doi.org/10.2307/2372560>.
- J. Edelmann and M. Plöchl. Handling characteristics and stability of the steady-state powerslide motion of an automobile. *Regular and Chaotic Dynamics*, 14(6):682–692, Dec. 2009. doi: 10.1134/s1560354709060069. URL <https://doi.org/10.1134/s1560354709060069>.
- M. Frego, E. Bertolazzi, F. Biral, D. Fontanelli, and L. Palopoli. Semi-analytical minimum time solutions for a vehicle following clothoid-based trajectory subject to velocity constraints. In *2016 European Control Conference (ECC)*, pages 2221–2227. IEEE, June 2016. doi: 10.1109/ecc.2016.7810621. URL <https://doi.org/10.1109/ecc.2016.7810621>.
- O. Galluppi, S. Formentin, S. M. Savaresi, and C. Novara. Multivariable nonlinear data-driven control with application to autonomous vehicle lateral dynamics. *Journal of Dynamic Systems, Measurement, and Control*, 141(10), June 2019. doi: 10.1115/1.4043926. URL <https://doi.org/10.1115/1.4043926>.
- R. Gambuti, S. Canale, F. Facchinei, A. Lanna, and A. D. Giorgio. Electric vehicle trip planning integrating range constraints and charging facilities. In *2015 23rd Mediterranean Conference on Control and Automation (MED)*, pages 472–479. IEEE, June 2015. doi: 10.1109/med.2015.7158793. URL <https://doi.org/10.1109/med.2015.7158793>.
- S. Gim, L. Adouane, S. Lee, and J.-P. Dérutin. Clothoids composition method for smooth path generation of car-like vehicle navigation. *Journal of Intelligent & Robotic Systems*, 88(1):129–146, Mar. 2017. doi: 10.1007/s10846-017-0531-8. URL <https://doi.org/10.1007/s10846-017-0531-8>.
- J. Y. Goh, T. Goel, and J. C. Gerdes. Toward automated vehicle control beyond the stability limits: Drifting along a general path. *Journal of Dynamic Systems, Measurement, and Control*, 142(2), Nov. 2019. doi: 10.1115/1.4045320. URL <https://doi.org/10.1115/1.4045320>.

- B. Goldfain, P. Drews, C. You, M. Barulic, O. Velev, P. Tsiotras, and J. M. Rehg. AutoRally: An open platform for aggressive autonomous driving. *IEEE Control Systems*, 39(1):26–55, Feb. 2019. doi: 10.1109/mcs.2018.2876958. URL <https://doi.org/10.1109/mcs.2018.2876958>.
- A. Goswami, H. Saeidi, A. Vahidi, and P. Jayakumar. Implementation of hierarchical framework with accurate localization and low level control in a low-cost scaled autonomous car. In *2018 Annual American Control Conference (ACC)*, pages 870–876. IEEE, June 2018. doi: 10.23919/acc.2018.8431024. URL <https://doi.org/10.23919/acc.2018.8431024>.
- D. Guo, J. Wang, J. B. Zhao, F. Sun, S. Gao, C. D. Li, M. H. Li, and C. C. Li. A vehicle path planning method based on a dynamic traffic network that considers fuel consumption and emissions. *Science of The Total Environment*, 663:935–943, May 2019. doi: 10.1016/j.scitotenv.2019.01.222. URL <https://doi.org/10.1016/j.scitotenv.2019.01.222>.
- R. Y. Hindiyeh. *Dynamics and control of drifting in automobiles*. PhD thesis, Stanford University, Mar. 2013. URL <https://ddl.stanford.edu/publications/dynamics-and-control-drifting-automobiles>.
- R. Y. Hindiyeh and J. Christian Gerdes. A Controller Framework for Autonomous Drifting: Design, Stability, and Experimental Validation. *Journal of Dynamic Systems, Measurement, and Control*, 136(5), 07 2014. ISSN 0022-0434. doi: 10.1115/1.4027471. URL <https://doi.org/10.1115/1.4027471>. 051015.
- L. M. Honório, E. B. Costa, E. J. Oliveira, D. de Almeida Fernandes, and A. P. G. Moreira. Persistently-exciting signal generation for optimal parameter estimation of constrained nonlinear dynamical systems. *ISA Transactions*, 77:231–241, June 2018. doi: 10.1016/j.isatra.2018.03.024. URL <https://doi.org/10.1016/j.isatra.2018.03.024>.
- A. Høyve. The effects of electronic stability control (ESC) on crashes—an update. *Accident Analysis & Prevention*, 43(3):1148–1159, May 2011. doi: 10.1016/j.aap.2010.12.025. URL <https://doi.org/10.1016/j.aap.2010.12.025>.
- C.-L. Hwang. Comparison of path tracking control of a car-like mobile robot with and without motor dynamics. *IEEE/ASME Transactions on Mechatronics*, 21(4):1801–1811, Aug. 2016. doi: 10.1109/tmech.2016.2553050. URL <https://doi.org/10.1109/tmech.2016.2553050>.
- A. Iannelli, A. Marcos, and M. Lowenberg. Robust estimations of the region of attraction using invariant sets. *Journal of the Franklin Institute*, 356(8):4622–4647, May 2019a.

- doi: 10.1016/j.jfranklin.2019.02.013. URL <https://doi.org/10.1016/j.jfranklin.2019.02.013>.
- A. Iannelli, P. Seiler, and A. Marcos. Region of attraction analysis with integral quadratic constraints. *Automatica*, 109:108543, Nov. 2019b. doi: 10.1016/j.automatica.2019.108543. URL <https://doi.org/10.1016/j.automatica.2019.108543>.
- S. Izumi, H. Somekawa, X. Xin, and T. Yamasaki. Analysis of robust transient stability of power systems using sum of squares programming. *International Journal of Electrical Power & Energy Systems*, 115:105401, Feb. 2020. doi: 10.1016/j.ijepes.2019.105401. URL <https://doi.org/10.1016/j.ijepes.2019.105401>.
- Z. Jarvis-Wloszek, R. Feeley, Weehong Tan, Kunpeng Sun, and A. Packard. Some controls applications of sum of squares programming. In *42nd IEEE International Conference on Decision and Control (IEEE Cat. No.03CH37475)*, volume 5, pages 4676–4681, Dec 2003. doi: 10.1109/cdc.2003.1272309. URL <https://doi.org/10.1109/cdc.2003.1272309>.
- Z. Jarvis-Wloszek, R. Feeley, W. Tan, K. Sun, and A. Packard. Control applications of sum of squares programming. In *Positive Polynomials in Control*, pages 3–22. Springer Berlin Heidelberg, Aug. 2005. doi: 10.1007/10997703_1. URL https://doi.org/10.1007/10997703_1.
- Z. W. Jarvis-Wloszek. *Lyapunov based analysis and controller synthesis for polynomial systems using sum-of-squares optimization*. PhD thesis, University of California, Berkeley Berkeley, CA, 2003.
- T. A. Johansen and T. I. Fossen. Control allocation—a survey. *Automatica*, 49(5):1087–1103, May 2013. ISSN 0005-1098. doi: 10.1016/j.automatica.2013.01.035. URL <https://doi.org/10.1016/j.automatica.2013.01.035>.
- D. B. Johnson and J. C. Huston. Nonlinear lateral stability analysis of road vehicles usingb liapunov’s second method. In *SAE Technical Paper Series*. SAE International, Sept. 1984. doi: 10.4271/841057. URL <https://doi.org/10.4271/841057>.
- M. Jones and M. M. Peet. Using sos and sublevel set volume minimization for estimation of forward reachable sets. *IFAC-PapersOnLine*, 52(16):484 – 489, 2019. ISSN 2405-8963. doi: <https://doi.org/10.1016/j.ifacol.2019.12.008>. URL <http://www.sciencedirect.com/science/article/pii/S2405896319318348>. 11th IFAC Symposium on Nonlinear Control Systems NOLCOS 2019.
- N. R. Kapania, J. Subosits, and J. C. Gerdes. A sequential two-step algorithm for fast generation of vehicle racing trajectories. *Journal of Dynamic Systems, Measurement,*

- and Control*, 138(9), June 2016. ISSN 0022-0434. doi: 10.1115/1.4033311. URL <https://doi.org/10.1115/1.4033311>.
- S. Karaman, A. Anders, M. Boulet, J. Connor, K. Gregson, W. Guerra, O. Guldner, M. Mohamoud, B. Plancher, R. Shin, and J. Vivilecchia. Project-based, collaborative, algorithmic robotics for high school students: Programming self-driving race cars at MIT. In *2017 IEEE Integrated STEM Education Conference (ISEC)*, pages 195–203. IEEE, 2017. doi: 10.1109/isecon.2017.7910242. URL <https://doi.org/10.1109/isecon.2017.7910242>.
- M. S. Kati, H. Köroğlu, and J. Fredriksson. Robust lateral control of long-combination vehicles under moments of inertia and tyre cornering stiffness uncertainties. *Vehicle System Dynamics*, 57(12):1847–1873, Dec. 2018. doi: 10.1080/00423114.2018.1552363. URL <https://www.tandfonline.com/doi/full/10.1080/00423114.2018.1552363>.
- D. I. Katzourakis, I. Papaefstathiou, and M. G. Lagoudakis. An open-source scaled automobile platform for fault-tolerant electronic stability control. *IEEE Transactions on Instrumentation and Measurement*, 59(9):2303–2314, Sept. 2010. doi: 10.1109/tim.2009.2034575. URL <https://doi.org/10.1109/tim.2009.2034575>.
- J. C. Kegelmann, L. K. Harbott, and J. C. Gerdes. Insights into vehicle trajectories at the handling limits: analysing open data from race car drivers. *Vehicle System Dynamics*, 55(2):191–207, Nov. 2016. doi: 10.1080/00423114.2016.1249893. URL <https://doi.org/10.1080/00423114.2016.1249893>.
- A. Khalifa, O. Kermorgant, S. Dominguez, and P. Martinet. An observer-based longitudinal control of car-like vehicles platoon navigating in an urban environment. In *2019 IEEE 58th Conference on Decision and Control (CDC)*, pages 5735–5741. IEEE, Dec. 2019. doi: 10.1109/cdc40024.2019.9029187. URL <https://doi.org/10.1109/cdc40024.2019.9029187>.
- H. Khalil. *Nonlinear Systems*. Pearson Education. Prentice Hall, 2002. ISBN 9780130673893. URL https://books.google.com.br/books?id=t_d1QgAACAAJ.
- S. Kohlbrecher, O. von Stryk, J. Meyer, and U. Klingauf. A flexible and scalable SLAM system with full 3d motion estimation. In *2011 IEEE International Symposium on Safety, Security, and Rescue Robotics*, pages 155–160. IEEE, Nov. 2011. doi: 10.1109/ssrr.2011.6106777. URL <https://doi.org/10.1109/ssrr.2011.6106777>.
- M. Kozłowski. Analysis of dynamics of a scaled PRT (personal rapid transit) vehicle. *Journal of Vibroengineering*, 21(5):1426–1440, Aug. 2019. doi: 10.21595/jve.2019.20577. URL <https://doi.org/10.21595/jve.2019.20577>.

- B. Landry, M. Chen, S. Hemley, and M. Pavone. Reach-avoid problems via sum-of-squares optimization and dynamic programming. In *2018 IEEE/RSJ International Conference on Intelligent Robots and Systems (IROS)*, pages 1–8. IEEE, Oct. 2018. doi: 10.1109/iros.2018.8594078. URL <https://doi.org/10.1109/iros.2018.8594078>.
- S. Lapapong, V. Gupta, E. Callejas, and S. Brennan. Fidelity of using scaled vehicles for chassis dynamic studies. *Vehicle System Dynamics*, 47(11):1401–1437, Oct. 2009. doi: 10.1080/00423110802687604. URL <https://doi.org/10.1080/00423110802687604>.
- V. A. Laurence, J. Y. Goh, and J. C. Gerdes. Path-tracking for autonomous vehicles at the limit of friction. In *2017 American Control Conference (ACC)*, pages 5586–5591. IEEE, May 2017. doi: 10.23919/acc.2017.7963824. URL <https://doi.org/10.23919/acc.2017.7963824>.
- S. Lefèvre, A. Carvalho, Y. Gao, H. E. Tseng, and F. Borrelli. Driver models for personalised driving assistance. *Vehicle System Dynamics*, 53(12):1705–1720, July 2015. doi: 10.1080/00423114.2015.1062899. URL <http://www.tandfonline.com/doi/full/10.1080/00423114.2015.1062899>.
- L. Li, K. Ota, and M. Dong. Humanlike driving: Empirical decision-making system for autonomous vehicles. *IEEE Transactions on Vehicular Technology*, 67(8):6814–6823, Aug. 2018. doi: 10.1109/tvt.2018.2822762. URL <https://doi.org/10.1109/tvt.2018.2822762>.
- Q. Li, G. Shi, J. Wei, and Y. Lin. Yaw stability control of active front steering with fractional-order PID controller. In *2009 International Conference on Information Engineering and Computer Science*. IEEE, Dec. 2009. doi: 10.1109/iciecs.2009.5366433. URL <https://doi.org/10.1109/iciecs.2009.5366433>.
- T.-C. Liang, J.-S. Liu, G.-T. Hung, and Y.-Z. Chang. Practical and flexible path planning for car-like mobile robot using maximal-curvature cubic spiral. *Robotics and Autonomous Systems*, 52(4):312–335, Sept. 2005. doi: 10.1016/j.robot.2005.05.001. URL <https://doi.org/10.1016/j.robot.2005.05.001>.
- H.-Y. Lin, C.-W. Yao, K.-S. Cheng, and V. L. Tran. Topological map construction and scene recognition for vehicle localization. *Autonomous Robots*, 42(1):65–81, Jan 2018. ISSN 1573-7527. doi: 10.1007/s10514-017-9638-9. URL <https://doi.org/10.1007/s10514-017-9638-9>.
- P. Liu, S. Rakheja, and A. K. W. Ahmed. Detection of dynamic roll instability of heavy vehicles for open-loop rollover control. In *SAE Technical Paper Series*. SAE International, Nov. 1997. doi: 10.4271/973263. URL <https://doi.org/10.4271/973263>.

- W. Liu. *Introduction to hybrid vehicle system modeling and control*. John Wiley & Sons, 2013.
- J. Lofberg. Pre- and post-processing sum-of-squares programs in practice. *IEEE Transactions on Automatic Control*, 54(5):1007–1011, May 2009. doi: 10.1109/tac.2009.2017144. URL <https://doi.org/10.1109/tac.2009.2017144>.
- A. Lutz, B. Schick, H. Holzmann, M. Kochem, H. Meyer-Tuve, O. Lange, Y. Mao, and G. Tosolin. Simulation methods supporting homologation of electronic stability control in vehicle variants. *Vehicle System Dynamics*, 55(10):1432–1497, June 2017. doi: 10.1080/00423114.2017.1322705. URL <https://doi.org/10.1080/00423114.2017.1322705>.
- T. T. Mac, C. Copot, D. T. Tran, and R. D. Keyser. Heuristic approaches in robot path planning: A survey. *Robotics and Autonomous Systems*, 86:13 – 28, 2016. ISSN 0921-8890. doi: <https://doi.org/10.1016/j.robot.2016.08.001>. URL <http://www.sciencedirect.com/science/article/pii/S0921889015300671>.
- M. I. Masouleh and D. J. N. Limebeer. Non-linear vehicle domain of attraction analysis using sum-of-squares programming. In *2016 IEEE Conference on Control Applications (CCA)*. IEEE, Sept. 2016. doi: 10.1109/cca.2016.7587971. URL <https://doi.org/10.1109/cca.2016.7587971>.
- M. I. Masouleh and D. J. N. Limebeer. Region of attraction analysis for nonlinear vehicle lateral dynamics using sum-of-squares programming. *Vehicle System Dynamics*, 56(7): 1118–1138, dec 2017. doi: 10.1080/00423114.2017.1409429. URL <https://doi.org/10.1080/00423114.2017.1409429>.
- T. Moore and D. Stouch. A generalized extended kalman filter implementation for the robot operating system. In *Intelligent Autonomous Systems 13*, pages 335–348. Springer International Publishing, Sept. 2015. doi: 10.1007/978-3-319-08338-4_25. URL https://doi.org/10.1007/978-3-319-08338-4_25.
- A. Narang. *Analysis and control of non-affine, non-standard, singularly perturbed systems*. PhD thesis, Texas A&M University, 2012. URL <https://core.ac.uk/reader/13642793>.
- B. Németh, P. Gáspár, and T. Péni. Nonlinear automotive actuator analysis based on sum of squares programming. In *2014 European Control Conference (ECC)*. IEEE, June 2014. doi: 10.1109/ecc.2014.6862429. URL <https://doi.org/10.1109/ecc.2014.6862429>.

- B. Németh, P. Gáspár, and T. Péni. Nonlinear analysis of vehicle control actuations based on controlled invariant sets. *International Journal of Applied Mathematics and Computer Science*, 26(1):31–43, Mar. 2016. doi: 10.1515/amcs-2016-0003. URL <https://doi.org/10.1515/amcs-2016-0003>.
- L. A. C. O. Nogueira, M. F. Koyama, R. A. Cordeiro, A. M. Ribeiro, S. S. Bueno, and S. S. Bueno. A miniaturized four-wheel robotic vehicle for autonomous driving research in off-road scenarios. In *XXII Congresso Brasileiro de Automática*, pages 1–7, 2018. doi: 10.20906/cps/cba2018-0369. URL <https://doi.org/10.20906/cps/cba2018-0369>.
- E. Ono, S. Hosoe, H. D. Tuan, and S. Doi. Bifurcation in vehicle dynamics and robust front wheel steering control. *IEEE Transactions on Control Systems Technology*, 6(3):412–420, May 1998. doi: 10.1109/87.668041. URL <https://doi.org/10.1109/87.668041>.
- M. Ozcan and M. M. Ankarali. Feedback motion planning for a dynamic car model via random sequential composition. In *2019 IEEE International Conference on Systems, Man and Cybernetics (SMC)*, pages 4239–4244. IEEE, Oct. 2019. doi: 10.1109/smc.2019.8913917. URL <https://doi.org/10.1109/smc.2019.8913917>.
- H. B. Pacejka. *Tire and Vehicle Dynamics*. Elsevier/BH, Amsterdam Boston, 2012. ISBN 978-0-08-097016-5. doi: 10.1016/c2010-0-68548-8. URL <https://doi.org/10.1016/c2010-0-68548-8>.
- A. Papachristodoulou. *Scalable analysis of nonlinear systems using convex optimization*. PhD thesis, California Institute of Technology, Jan. 2005. URL <https://thesis.library.caltech.edu/1678/>.
- A. Papachristodoulou and S. Prajna. On the construction of lyapunov functions using the sum of squares decomposition. In *Proceedings of the 41st IEEE Conference on Decision and Control*, volume 3, pages 3482–3487, Dec 2002. doi: 10.1109/cdc.2002.1184414. URL <https://doi.org/10.1109/cdc.2002.1184414>.
- A. Papachristodoulou, J. Anderson, G. Valmorbida, S. Prajna, P. Seiler, and P. A. Parrilo. *SOSTOOLS: Sum of squares optimization toolbox for MATLAB*, 2013. URL <http://www.cds.caltech.edu/sostools/>.
- K. Park, S.-J. Heo, and I. Baek. Controller design for improving lateral vehicle dynamic stability. *JSAE Review*, 22(4):481 – 486, 2001. ISSN 0389-4304. doi: [https://doi.org/10.1016/S0389-4304\(01\)00141-2](https://doi.org/10.1016/S0389-4304(01)00141-2). URL <http://www.sciencedirect.com/science/article/pii/S0389430401001412>.
- P. A. Parrilo. *Structured semidefinite programs and semialgebraic geometry methods in robustness and optimization*. PhD thesis, California Institute of Technology, may 2000. URL <http://www.mit.edu/~parrilo/pubs/files/thesis.pdf>.

- P. A. Parrilo. Semidefinite programming relaxations for semialgebraic problems. *Mathematical Programming*, 96(2):293–320, May 2003. ISSN 1436-4646. doi: 10.1007/s10107-003-0387-5. URL <https://doi.org/10.1007/s10107-003-0387-5>.
- M. Patel, G. Orzechowski, Q. Tian, and A. A. Shabana. A new multibody system approach for tire modeling using ANCF finite elements. *Proceedings of the Institution of Mechanical Engineers, Part K: Journal of Multi-body Dynamics*, 230(1):69–84, Mar. 2015. doi: 10.1177/1464419315574641. URL <https://doi.org/10.1177/1464419315574641>.
- R. Pinto, A. E. B. Velasquez, I. L. A. Pedraza, V. A. H. Higuti, M. V. Gasparino, and M. Becker. Deployment of a smooth clothoid-based path planning and predictive control for the autonomous navigation of a car-like robot. In *Proceedings of the 25th International Congress of Mechanical Engineering*. ABCM, 2019. doi: 10.26678/abcm.cobem2019.cob2019-1683. URL <https://doi.org/10.26678/abcm.cobem2019.cob2019-1683>.
- J. L. Pitarch, A. Sala, and C. V. Arino. Closed-form estimates of the domain of attraction for nonlinear systems via fuzzy-polynomial models. *IEEE Transactions on Cybernetics*, 44(4):526–538, Apr. 2014. doi: 10.1109/tcyb.2013.2258910. URL <https://doi.org/10.1109/tcyb.2013.2258910>.
- M. Polley, A. Alleyne, and E. D. Vries. Scaled vehicle tire characteristics: dimensionless analysis. *Vehicle System Dynamics*, 44(2):87–105, Feb. 2006. ISSN 0042-3114, 1744-5159. doi: 10.1080/00423110500385717. URL <https://doi.org/10.1080/00423110500385717>.
- V. Powers and T. Wörmann. An algorithm for sums of squares of real polynomials. *Journal of Pure and Applied Algebra*, 127(1):99 – 104, 1998. ISSN 0022-4049. doi: [https://doi.org/10.1016/S0022-4049\(97\)83827-3](https://doi.org/10.1016/S0022-4049(97)83827-3). URL <http://www.sciencedirect.com/science/article/pii/S0022404997838273>.
- R. Rajamani. *Vehicle dynamics and control*. Springer Science & Business Media, 2011.
- R. Rhinehart. *Nonlinear regression modeling for engineering applications : modeling, model validation, and enabling design of experiments*. John Wiley & Sons, Chichester, UK Hoboken, NJ, 2016. ISBN 978-1-118-59796-5.
- A. M. Ribeiro. Desenvolvimento de uma abordagem de diferencial eletrônico para um veículo elétrico robótico multitração. Master’s thesis, Universidade Estadual de Campinas, may 2016. URL <http://repositorio.unicamp.br/jspui/handle/REPOSIP/305471>.

- A. M. Ribeiro, A. R. Fioravanti, A. Moutinho, and E. C. de Paiva. Sum of squares approach for ground vehicle lateral control under tire saturation forces. *IFAC-PapersOnLine*, , to appear:1–7, 2020. 21th IFAC World Congress.
- Z. Rong-hui, C. Guo-ying, W. Guo-qiang, J. Hong-guang, and C. Tao. Robust optimal control technology for four-wheel steering vehicle. In *2007 International Conference on Mechatronics and Automation*, pages 1513–1517. IEEE, Aug. 2007. doi: 10.1109/icma.2007.4303773. URL <https://doi.org/10.1109/icma.2007.4303773>.
- F. D. Rossa and G. Mastinu. Straight ahead running of a nonlinear car and driver model – new nonlinear behaviours highlighted. *Vehicle System Dynamics*, 56(5):753–768, Jan. 2018. doi: 10.1080/00423114.2017.1422526. URL <https://doi.org/10.1080/00423114.2017.1422526>.
- S. Sadri and C. Q. Wu. Lateral stability analysis of on-road vehicles using Lyapunov’s direct method. In *2012 IEEE Intelligent Vehicles Symposium*, pages 821–826. IEEE, June 2012. doi: 10.1109/ivs.2012.6232162. URL <https://doi.org/10.1109/ivs.2012.6232162>.
- SAE International. Taxonomy and definitions for terms related to driving automation systems for on-road motor vehicles. In *Ground Vehicle Standard J3016*, pages 1–35, June 2018. URL https://saemobilus.sae.org/content/J3016_201806.
- P. Seiler. SOSOPT: A toolbox for polynomial optimization. *CoRR*, abs/1308.1889, 2013. URL <https://dept.aem.umn.edu/~AerospaceControl/>.
- X. Shen, S. Diamond, M. Udell, Y. Gu, and S. Boyd. Disciplined multi-convex programming. In *2017 29th Chinese Control And Decision Conference (CCDC)*, pages 895–900. IEEE, May 2017. doi: 10.1109/ccdc.2017.7978647. URL <https://doi.org/10.1109/ccdc.2017.7978647>.
- S. Singh, M. Chen, S. L. Herbert, C. J. Tomlin, and M. Pavone. Robust tracking with model mismatch for fast and safe planning: An SOS optimization approach. In *Springer Proceedings in Advanced Robotics*, pages 545–564. Springer International Publishing, 2020. doi: 10.1007/978-3-030-44051-0_32. URL https://doi.org/10.1007/978-3-030-44051-0_32.
- E. N. Smith, E. Velenis, D. Tavernini, and D. Cao. Effect of handling characteristics on minimum time cornering with torque vectoring. *Vehicle System Dynamics*, 56(2):221–248, 2018. doi: 10.1080/00423114.2017.1371771. URL <https://doi.org/10.1080/00423114.2017.1371771>.

- G. Stengle. A nullstellensatz and a positivstellensatz in semialgebraic geometry. *Mathematische Annalen*, 207(2):87–97, June 1974. doi: 10.1007/bf01362149. URL <https://doi.org/10.1007/bf01362149>.
- W. Sun, J. Tian, S. Li, Z. Yang, and Z. Ma. Stability analysis of vehicle negotiating a curve in the plane. *Advances in Mechanical Engineering*, 5:893835, Jan. 2013. doi: 10.1155/2013/893835. URL <https://doi.org/10.1155/2013/893835>.
- M. Tacchi, B. Marinescu, M. Anghel, S. Kundu, S. Benahmed, and C. Cardozo. Power system transient stability analysis using sum of squares programming. In *2018 Power Systems Computation Conference (PSCC)*, pages 1–7. IEEE, June 2018. doi: 10.23919/pssc.2018.8442484. URL <https://doi.org/10.23919/pssc.2018.8442484>.
- T. A. Tamba and Y. Y. Nazaruddin. Nonlinear stability analysis of vehicle side-slip dynamics using SOS programming. In *2018 5th International Conference on Electric Vehicular Technology (ICEVT)*. IEEE, Oct. 2018. doi: 10.1109/icevt.2018.8628351. URL <https://doi.org/10.1109/icevt.2018.8628351>.
- W. Tan and A. Packard. Stability region analysis using polynomial and composite polynomial lyapunov functions and sum-of-squares programming. *IEEE Transactions on Automatic Control*, 53(2):565–571, Mar. 2008. doi: 10.1109/tac.2007.914221. URL <https://doi.org/10.1109/tac.2007.914221>.
- R. Tedrake and the Drake Development Team. Drake: Model-based design and verification for robotics, 2019. URL <https://drake.mit.edu>.
- U. Topcu, A. Packard, and P. Seiler. Local stability analysis using simulations and sum-of-squares programming. *Automatica*, 44(10):2669–2675, Oct. 2008. doi: 10.1016/j.automatica.2008.03.010. URL <https://doi.org/10.1016/j.automatica.2008.03.010>.
- U. Topcu, A. Packard, P. Seiler, and G. Balas. Robust region-of-attraction estimation. *IEEE Transactions on Automatic Control*, 55(1):137–142, Jan. 2010. doi: 10.1109/tac.2009.2033751. URL <https://doi.org/10.1109/tac.2009.2033751>.
- A. Tota, B. Lenzo, Q. Lu, A. Sorniotti, P. Gruber, S. Fallah, M. Velardocchia, E. Galvagno, and J. D. Smet. On the experimental analysis of integral sliding modes for yaw rate and sideslip control of an electric vehicle with multiple motors. *International Journal of Automotive Technology*, 19(5):811–823, Sept. 2018. doi: 10.1007/s12239-018-0078-0. URL <https://doi.org/10.1007/s12239-018-0078-0>.
- K. Treetipsounthorn and G. Phanomchoeng. Real-time rollover warning in tripped and un-tripped rollovers with a neural network. In *2018 IEEE 4th International Conference on Control Science and Systems Engineering (ICCSSE)*, pages 95–100. IEEE,

- Aug. 2018. doi: 10.1109/ccsse.2018.8724838. URL <https://doi.org/10.1109/ccsse.2018.8724838>.
- H. True. On the theory of nonlinear dynamics and its applications in vehicle systems dynamics. *Vehicle System Dynamics*, 31(5-6):393–421, 1999. doi: 10.1076/vesd.31.5.393.8361. URL <https://www.tandfonline.com/doi/abs/10.1076/vesd.31.5.393.8361>.
- J. Villagra, V. Milanés, J. Pérez, and J. Godoy. Smooth path and speed planning for an automated public transport vehicle. *Robotics and Autonomous Systems*, 60(2):252–265, Feb. 2012. doi: 10.1016/j.robot.2011.11.001. URL <https://doi.org/10.1016/j.robot.2011.11.001>.
- C. Voser, R. Y. Hindiyeh, and J. C. Gerdes. Analysis and control of high sideslip manoeuvres. *Vehicle System Dynamics*, 48(sup1):317–336, Dec. 2010. doi: 10.1080/00423111003746140. URL <https://doi.org/10.1080/00423111003746140>.
- F. Wang and Y. Chen. Dynamics and control of a novel active yaw stabilizer to enhance vehicle lateral motion stability. *Journal of Dynamic Systems, Measurement, and Control*, 140(8), Mar. 2018. ISSN 0022-0434. doi: 10.1115/1.4039187. URL <https://doi.org/10.1115/1.4039187>.
- S. Wang, Z. She, and S. S. Ge. Estimating minimal domains of attraction for uncertain nonlinear systems. *IEEE Transactions on Systems, Man, and Cybernetics: Systems*, pages 1–12, 2020a. doi: 10.1109/tsmc.2020.2980673. URL <https://doi.org/10.1109/tsmc.2020.2980673>.
- S. Wang, Z. She, and S. S. Ge. Inner-estimating domains of attraction for nonpolynomial systems with polynomial differential inclusions. *IEEE Transactions on Cybernetics*, pages 1–14, 2020b. doi: 10.1109/tcyb.2020.2987326. URL <https://doi.org/10.1109/tcyb.2020.2987326>.
- W. Xu, Z. J. Fu, W. D. Xie, A. Q. He, Y. Xiao, and B. Li. Optimal torque vectoring control for distributed drive electric vehicle. *International Journal of Modelling, Identification and Control*, 31(2):124, 2019. doi: 10.1504/ijmic.2019.098000. URL <https://doi.org/10.1504/ijmic.2019.098000>.
- H. Yamaguchi, A. Nishijima, and A. Kawakami. Control of two manipulation points of a cooperative transportation system with two car-like vehicles following parametric curve paths. *Robotics and Autonomous Systems*, 63:165–178, Jan. 2015. doi: 10.1016/j.robot.2014.07.007. URL <https://doi.org/10.1016/j.robot.2014.07.007>.

- C. You, J. Lu, D. Filev, and P. Tsiotras. Highway traffic modeling and decision making for autonomous vehicle using reinforcement learning. In *2018 IEEE Intelligent Vehicles Symposium (IV)*, pages 1227–1232, June 2018. doi: 10.1109/ivs.2018.8500675. URL <https://doi.org/10.1109/ivs.2018.8500675>.
- H. Yuan, X. Sun, and T. Gordon. Unified decision-making and control for highway collision avoidance using active front steer and individual wheel torque control. *Vehicle System Dynamics*, 57(8):1188–1205, Oct. 2018. doi: 10.1080/00423114.2018.1535125. URL <https://doi.org/10.1080/00423114.2018.1535125>.
- L. Yuan, H. Zhao, H. Chen, and B. Ren. Nonlinear MPC-based slip control for electric vehicles with vehicle safety constraints. *Mechatronics*, 38:1–15, Sept. 2016. ISSN 0957-4158. doi: 10.1016/j.mechatronics.2016.05.006. URL <https://doi.org/10.1016/j.mechatronics.2016.05.006>.
- L. Yue, M. Abdel-Aty, Y. Wu, and L. Wang. Assessment of the safety benefits of vehicles’ advanced driver assistance, connectivity and low level automation systems. *Accident Analysis & Prevention*, 117:55–64, Aug. 2018. ISSN 0001-4575. doi: 10.1016/j.aap.2018.04.002. URL <http://www.sciencedirect.com/science/article/pii/S0001457518301404>.
- X. Zheng, Z. She, Q. Liang, and M. Li. Inner approximations of domains of attraction for a class of switched systems by computing lyapunov-like functions. *International Journal of Robust and Nonlinear Control*, 28(6):2191–2208, Dec. 2018. doi: 10.1002/rnc.4010. URL <https://doi.org/10.1002/rnc.4010>.